CHARACTERIZATION OF HIGH-Z PIXEL ARRAY DETECTORS FOR X-RAY IMAGING AT A SYNCHROTRON

A Thesis

Presented to the Faculty of the Physics Department

of Cornell University

in Partial Fulfillment of the Requirements for the Degree of

Bachelor of Arts

by

Alexander Albert

May 2023

CHARACTERIZATION OF HIGH-Z PIXEL ARRAY DETECTORS FOR X-RAY IMAGING AT A SYNCHROTRON

Alexander Albert, B.A.

Cornell University 2023

X-ray synchrotron experiments are imperative to the characterization of many materials at the smallest scales. Currently, there does not exist a sufficiently capable detector for photons with energies greater than 20 keV. Most synchrotrons use detectors with a semiconducting silicon sensor layer, but the detection efficiency, limited by the fraction of absorbed photons, decreases dramatically for silicon at these energies. Using our in-house characterization setup, we investigated the behavior of silicon and various alternative materials with a larger atomic number ("high-Z"). This included germanium and amorphous selenium, two candidates that have been characterized in previous studies and have well-developed fabrication methods. We also studied lead perovskite ($CsPbBr_3$) and cadmium zinc telluride - selenium (CZTS), two materials from which high-quality single-crystals can be grown, but whose behavior and durability in a high flux, high bias environment is not as well characterized. These sensors were bonded to the Mixed Mode Pixel Array Detector (MMPAD), a readout architecture designed by the Gruner lab that is equipped for continuous imaging at high fluxes. The noise, dark current, leakage current, pixel-by-pixel uniformity, spatial resolution, dynamic response, and other metrics of performance were assessed, and the advantages and limitations of each sensor were identified. None of the high-Z sensors exhibited the performance of silicon after photon absorption, but the behaviors of each material under the conditions required for synchrotron imaging were better understood.

BIOGRAPHICAL SKETCH

Alexander Albert was born in Sydney, Australia in 2001 and grew up in Pearland, Texas. He graduated from Glenda Dawson High School in 2019 and attended Cornell University from 2019 to 2023, where he received a Bachelor of Arts in Physics and Mathematics. He begins graduate studies in Physics at the California Institute of Technology in September 2023.

ACKNOWLEDGEMENTS

Throughout my undergraduate career, I have been extremely fortunate to do research under the guidance and support of so many wonderful people. I would first like to thank my advisors for this thesis project: Julia Thom-Levy and Sol Gruner. Thank you so much for welcoming me to the group! Professor Thom has been an amazing mentor ever since I first knocked on her office door as a freshman. Thank you for the invaluable support you have provided at every step of my academic journey. And to Professor Gruner, thank you for the insight you have provided both for this project and for my future aspirations in grad school and beyond. I must also express special thanks to Dr. Mark Tate, who has been nothing short of a third advisor. Mark taught me everything I know about X-ray detectors, and his ability to fix any experimental problem I would encounter is truly remarkable and inspirational.

The rest of the Gruner/Thom-Levy detector lab have also been a tremendous source of support. Thank you Marty, Marianne, Kate, Divya, William, Lena, Nick, Blake, and Chester for all of the help you have provided, whether it meant working during the weekend and late at night for the CZTS CHESS run, providing feedback on any practice talks I'd give at the group meeting, or even fixing my glasses (thanks Marty!). I'm also extremely grateful for the mentorship provided by Dr. Joey Reichert and Dr. Jan Strube in my high energy physics endeavors. Thank you for your patience and your willingness to answer all of my questions! I believe that my many one-on-one conversations with each of you have sparked a deep interest in particle physics.

My college experience has been so rich and enjoyable largely due to the amazing friends I've made along the way. To the group at 241 Linden and everyone associated, thanks for all of the great memories! And thank you to my friends in

Pearland - I would always be so excited for the things we would do over break.

Lastly, a special thank you to my parents and my bulldog, Archie. I'm so lucky to have had such a wonderful childhood and loving family always there for me.

TABLE OF CONTENTS

LIST OF TABLES

LIST OF FIGURES

CHAPTER 1

INTRODUCTION

X-rays, the subset of electromagnetic radiation with a wavelength ranging from 0.01-10 nm, are a subject of considerable interest to physicists, engineers, physicians, and professionals in a wide variety of fields [3]. The small wavelength of an X-ray, relative other sources of radiation such as visible light, can yield valuable information about the structure and composition of a given material at atomic scales, as the location, energy, and other attributes of an X-ray beam can be measured after it interacts with a sample. In radiography, medical professionals use X-rays to image underneath tissue and view the inner structure of various parts of the body via a two-dimensional projection [3]. Lower frequency electromagnetic radiation usually fails to penetrate the human skin, and high-energy gamma radiation is emitted predominately during nuclear processes and can be more difficult to produce using commercial technology [16]. Moreover, astrophysicists have developed X-ray telescopes, as stellar matter often emits X-ray photons when consumed by a black hole and exploding supernovae are often characterized by a flash of X-rays that illuminate regions of space up to light years away [17, 18]. Thus, X-ray radiation not only is produced in a controlled environment and used for everyday purposes, but also permeates the universe, serving as a probe to discover new phenomena at all scales.

In this thesis, we focus on the imaging applications of X-rays and the instrumentation required to realize the numerous applications of X-ray imaging to material science. For example, many metallic alloys consist of a set of neighboring crystalline grains, each with a uniform solid-state structure [19]. The application of external stresses can lead to fracturing at the interface between neighboring grains,

a phenomenon known as"grain-boundary cracking", and other microstructural deformations that can eventually lead to large-scale damage in materials used often for aircraft, spacecraft, and many other industries [19]. High energy X-ray Diffraction Microscopy (HEDM) is an emerging technique used by physicists and material scientists to image polycrystalline materials, at the length scale of a grain, upon the application of an external load [4]. In HEDM, incoming X-ray photons interact with the crystal structure of the sample via diffraction, and a 3-D reconstruction of the sample at the microscale can be ascertained via fast-framing detectors [4].

HEDM, as well as other imaging techniques that probe the structure of materials at this scale, usually take place at an synchrotron light source (or "synchrotron"), where high energy photons can be generated with the greatest flux [4]. Most synchrotrons consist of an otherwise empty circular storage ring through which electrons travel at relativistic speeds [20]. A charged particle must be constantly accelerating to move in a circle (the direction of its velocity is constantly changing), which generates of electromagnetic "synchrotron" radiation. The energy of the radiated photons varies with the speed of the charged particle, its mass, and the radius of its path. The radius of the beamline is roughly fixed after construction, but the electrons can be accelerated about the storage rings with speeds that generate synchrotron radiation in the X-ray regime. The facility is constructed so that the resulting X-rays are diverted to where the experiments are taking place [20].

At the time of writing, there does not exist a detector that performs well at synchrotron energies and fluxes and exhibits a high spatial resolution, low noise, and that otherwise satisfies all of the necessary specifications that will be described in this thesis. The sensor characterizations described in the coming chapters strive

(a)

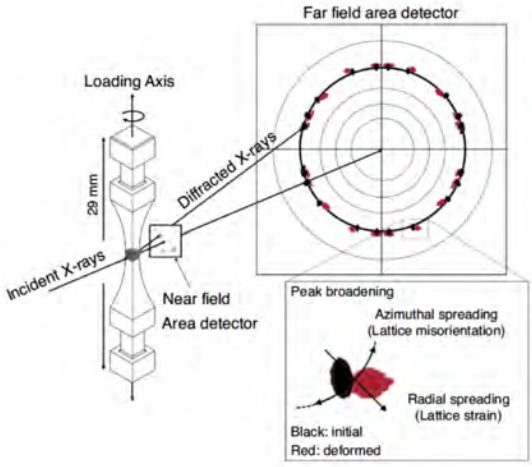

(b)

(c)

Figure 1.1: (a) is a radiograph of a human arm. (b) illustrates an HEDM experiment and its sensitivity to grain-level deformations in a sample. (c) depicts the size of the Cornell High Energy Synchrotron (CHESS) relative to a soccer field [3, 4, 5]

to comparatively assess the advantages and limitations associated with different sensor materials, with the overarching goal of improving detector performance in a synchrotron environment.

1.1 Advancements in X-ray Detection Technology

Any X-ray imager utilizes either *direct* or *indirect* detection. One of the earliest and most widely used X-ray detectors developed for use at a light source was the Charge Coupled Device (CCD) detector, invented in Bell Labs in 1969 [21]. Like the majority of today's X-ray detectors, early CCDs consisted of a silicon semiconductor sensor with a MOS composition [21]. The CCD would consist of an array of MOS capacitors, each of which would accumulate some photogenerated charge proportional to the intensity of incident radiation [22]. Using an effective shift register, signal charge would be transferred from capacitor to capacitor until it reached an amplifier that would convert the charge into a signal voltage that could be stored in memory [22]. An image can be reconstructed from the signal voltages associated with each capacitor in the array. Although the CCD was fundamentally photosensitive device with the ability to produce a two-dimensional X-ray image, it lacked the sensitivity and radiation hardness required for the direct detection of X-ray photons [23].

To ameliorate these drawbacks, CCD operators would place a large-area phosphor screen in front of the CCD to effectively act as an amplifier [23]. Atoms in the phosphor screen would be scintillated by incoming X-rays and the generated optical photons would be diverted towards the CCD [23]. This fundamentally indirect detection method, though more effective than directly exposing the CCD to X-rays, still lacked the sensitivity and temporal resolution required for high-precision measurements, particularly for experiments with higher fluxes and harder X-rays [23]. The distance between the phosphor screen and the CCD also introduced an additional means through which the spatial resolution could be worsened, as the detected optical photons would have to be "traced back" to the position at which

they first interacted with the screen [23].

The Hybrid Pixel Detector (HPD) is a modern solution to many of the inefficiencies that plague indirect X-ray detection. Though CCD performance has dramatically improved throughout the late 20th and early 21st centuries, and CCDs are still commonly used in experiments with soft X-rays, HPDs enjoy an improved dynamic range, sensitivity, and resolution [6]. HPDs, like CCDs, use a semiconducting sensor layer to convert incident radiation to electron-hole pairs. However, the semiconductor is bonded face-to-face with a silicon readout chip - both the semiconducting sensor layer and the readout chip are pixelated, and an array of (usually solder) bump-bonds connect each sensor pixel to a readout channel [6]. Each channel consists of its own electronics, typically an Application Specific Integrating Circuit (ASIC). The ASIC used in an HPD is typically fabricated using commercially available CMOS technology that enjoys faster readout than a CCD [6, 22]. The result is a faster, more robust detector that is capable of direct X-ray detection. Figure 1.2 illustrates the operational differences between CCDs and HPDs.

The basic detection mechanism in an HPD is relatively straightforward. Incoming X-ray photons generate charge carriers in the bulk semiconductor, which drift towards to the readout chip via the electric field induced from an applied bias voltage. The total registered signal in a given pixel over a specified collection time is computed via an integrating operational amplifier (op-amp). After additional post-processing steps, a pixel-by-pixel X-ray image can be reconstructed with a resolution on the order of the pixel size [24]. The ASIC's fast readout allows for near-continuous live data acquisition with noise mainly due to photon counting statistics [6]. The Mixed Mode Pixel Array Detector (MMPAD), designed by this

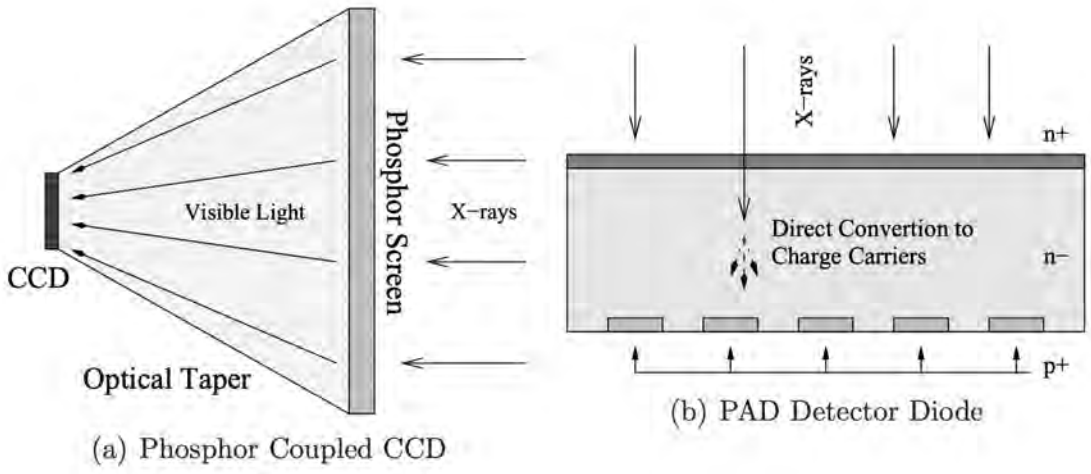

Figure 1.2: (a) illustrates the operation of many early CCDs in which the conversion of X-ray radiation to optical photons before exposure to the main detector would be a necessary step. (b) depicts the direct conversion of X-ray photons to charge carriers in the sensor layer of a PAD [2]

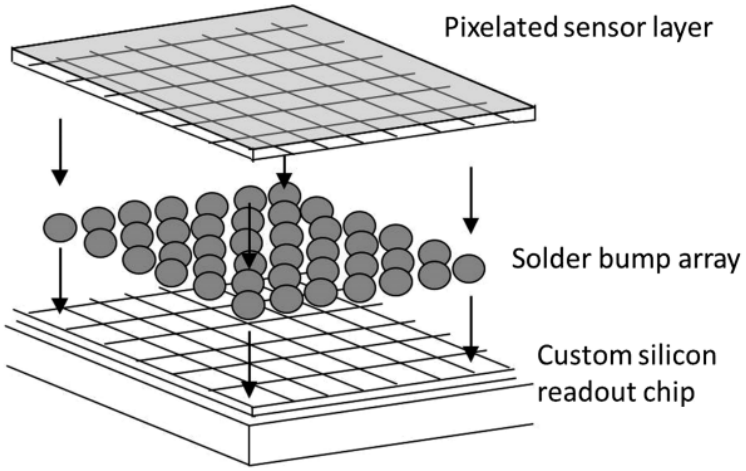

Figure 1.3: Geometry of a Hybrid Pixel Detector [6]

group, is one such particularly high-performing HPD. I will present a more thorough description of Pixel Array Detectors (PADs) in later sections of this thesis.

1.2 Fundamentals of Semiconductor Physics

In a conceptual representation of an HPD, the pixelated sensor layer is almost entirely distinct from the readout chip. Assuming sufficient radiation hardness, the readout chip only meaningfully interacts with collected charge from the sensor, not the incident X-rays themselves. Therefore, the ASIC engineers who design the readout chip have jurisdiction over the readout speed, readout noise, and other aspects of the signal processing, but largely do not concern themselves with the behavior of the sensor layer itself. The generation of a meaningful signal, which physically is a localized increase in electric charge available for conduction upon the absorption of an X-ray photon, is determined entirely by the physical properties of the sensor layer. To understand how different sensor materials impact detector performance, a rudimentary understanding of the physics of semiconductors is required. In this section, we highlight important behaviors in semiconductor physics, predominately in the context of crystalline materials.

1.2.1 The Band Theory of Solids

Many naturally-occurring solids have a crystalline structure, in which atoms or molecules are arranged in a well-defined and repeating lattice geometry. The energy of the quantum states that the valence electrons of a given atom inhabit is determined by the lattice spacing, or how close that atom is to its nearest neighbors. If interactions between neighboring atoms are ignored, perhaps due to a large lattice spacing, each set of valence electrons will occupy the same energy states [7]. Once inter-atom interactions are considered and the lattice spacing is reduced, each energy level becomes N-fold degenerate, where N is the number of

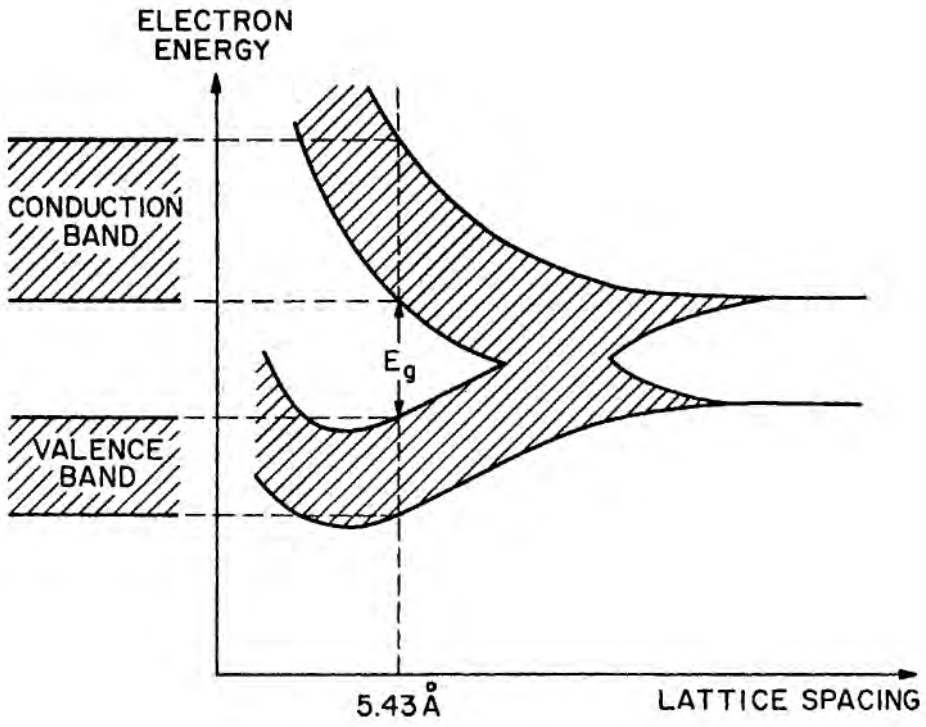

Figure 1.4: Band Structure for silicon arranged in a diamond lattice. The diagram demonstrates how the two discrete energy states are split in continuum valence and conduction bands once the lattice spacing is decreased [7].

atoms in the lattice [7]. The energy levels eventually split to lift the degeneracy, and as N$\rightarrow \infty$, the set of energies valence electrons can inhabit becomes a continuum known as the *valence band* [7]. Electrons in the valence band are still bound to the crystal lattice. There also exists a continuous band for higher energy states, in which electrons are still bound to the lattice structure but are free to move to different lattice sites in the materials via conduction. These energies constitute the *conduction band*. When an electron is excited to the conduction band, the resulting vacancy in its valence shell is called a hole. The behavior of a hole is akin to that of a positive charge carrier in the conduction band with a different mobility than an electron [7].

The *band gap* of a given solid is the energy difference between the bottom of

the conduction band and the top of the valence band. In a conductor there is no band gap because the valence and conduction bands overlap [25]. A *semiconductor* is a material whose band gap is less than 5 eV and an insulator is one with a band gap greater than 5 eV [25]. Though an amorphous material lacks a uniform lattice geometry on the same length scales as a crystal, a local band structure exists at any given location [26]. The material can then be labeled a conductor, semiconductor, or insulator based on the approximate band gap throughout [26].

1.2.2 Impurities and Defects

Consider a lattice of silicon atoms, each of which has 4 electrons in its valence shell. If a single atom in the lattice is replaced by a different element with a different number of valence electrons, as shown in Figure 1.5, an additional electron or hole is available for conduction [27]. Thus, the conductivity of the material and the concentration of its charge carriers can be purposefully modified by the injection of impurities, a process known as *doping*. An n-type semiconductor has been doped such that there exists an excess of electrons in the conduction band [27]. These impurities are called donors. P-type semiconductors have an excess of holes, which again is equivalent to having positive charge carriers in the conduction band [27]. These impurities are called acceptors. Many of the most important semiconducting technologies, such as PN junction diodes and MOS capacitors, implement p-doped and n-doped materials. The doping profile of the sensor layer is an important consideration during fabrication of an HPD.

Apart from the purposeful inclusion of impurities, unintended aberrations, or "defects", may break the symmetry of the lattice structure at particular locations. This include point defects, in which there may be extra or missing atoms in the

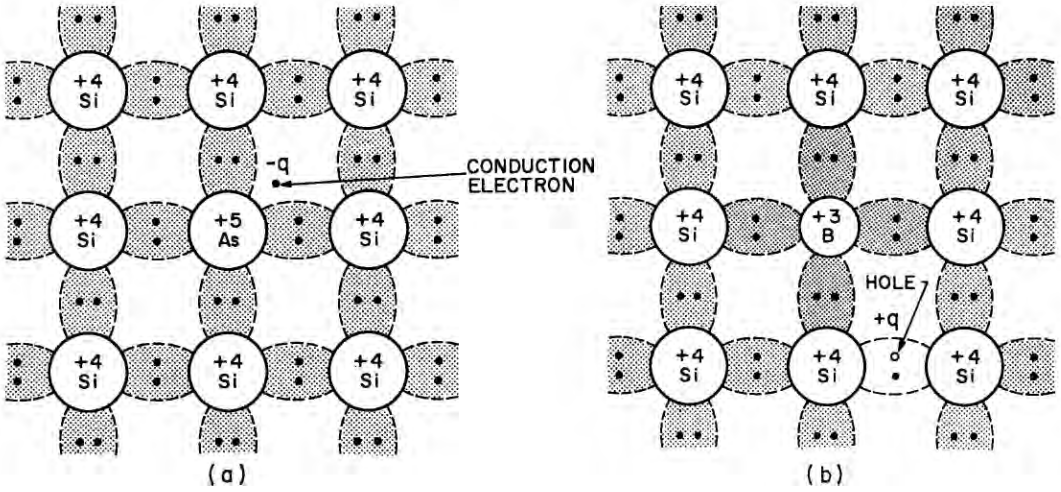

Figure 1.5: (a) and (b) show the lattice structure of n-type and p-type silicon respectively. The arsenic impurity in (a) introduces a conduction electron, while the boron impurity in (b) introduces a hole [7].

lattice [7]. A collection of point defects creates a defect cluster, which can behave like a localized charge distribution and affect the electric field in the bulk semiconductor [7]. Defect clusters are also created and exacerbated by exposure to radiation [28].

These types of defects can also locally modify the band structure, creating quantum states with an energy in the band gap [28]. If a state is sufficiently close to the band edges, it can become a charge "trap": a state in which charge carriers can be held for a period of time and later released [28]. Defect states and charge traps can be hugely detrimental to X-ray imaging and contribute to many of the sensor limitations described in this thesis.

1.2.3 Generation and Recombination of Charge Carriers

The transfer of charge from the valence band to the conduction band and vice versa is induced by several mechanisms. If the semiconductor is at a high enough

temperature, thermal vibrations can excite charge carriers from the valence band to the conduction band. This constitutes a background signal known as the *dark current*. The transition occurs via either a direct band-to-band excitation or a two-step process in which the charge carrier temporarily inhabits a defect-induced band gap state [7].

Electromagnetic radiation with a sufficiently high energy can also generate free charge in the conduction band. This is the fundamental principle behind almost all X-ray detectors. X-rays interacts with matter via three mechanisms: the photoelectric effect, Compton scattering, and electron-positron pair production [2]. At synchrotron energies, most interactions are photoelectric, meaning incident photons are absorbed by the material and electrons are ionized from the valence band to the conduction band. A phonon is also emitted in the lattice itself [7]. This process is known as the *photogeneration* of charge carriers. Like thermal charge generation, ionization can be assisted by intermediate band gap states [7]. For common sensor materials, such as silicon and germanium, the ionization energy is approximately three times the band gap [25]. For an X-ray photon with energy E_X that is absorbed by a material with ionization energy E_I, the number of photogenerated charge carriers N is given by:

$$N = \frac{E_X}{E_I} \tag{1.1}$$

Interestingly, the uncertainty associated with carrier generation is markedly lower than that of a purely Poissonian process. The Poissonian noise is scaled down by a material-dependent value called the Fano Factor. These modified statistics are implemented in a variety of particle detection experiments [2].

Semiconductors are well-suited for X-ray imaging, as the ionization energy of the material is such that synchrotron X-rays can generate a charge cloud greater

than the noise threshold of the processing ASIC. This is not possible for insulators. Free charge is impossible to eliminate in true conductors, so a photogenerated signal would be nearly impossible to discriminate from background currents.

Charge carriers in the semiconductor may also exit the conduction band via a process known as recombination. In band-to-band recombination, electrons are de-excited and reincorporated with holes in the valence band, accompanied by an emission of a photon or heating of the material [28]. Like carrier generation, recombination can be assisted by the lattice imperfections that create defect states in the band gap, a process known as Shockley-Read-Hall (SRH) recombination [29]. Generation and recombination rates are both affected by the defect-induced charge traps mentioned earlier in this section. We will refrain from a quantitative description of these processes, but carrier trapping can result in measurable effects on total generation, recombination, and carrier transport in the semiconductor.

1.2.4 Charge Transport

Highly-performing sensors must exhibit a strong charge collection efficiency and excellent spatial resolution, meaning that nearly all photogenerated charge must reach the ASIC at the same location in the 2-D readout array for the corresponding signal to be properly reconstructed. The transfer of free charge at any point in the sensor bulk to the readout chip should be optimized, so a fundamental understanding of semiconductor charge transport is required.

Charge transport is characterized predominately by two mechanisms: *diffusion* and *drift* [2]. Diffusion is primarily a probabilistic phenomenon akin to the spreading of a gas in a container after a partition is removed. In simple terms, particles

move from an area with a high concentration to one with a low concentration. This helps explain why a charge cloud spreads as it moves through the sensor. Quantitatively, the current density associated with the diffusion of charge carriers is proportional to the gradient of the charge carrier concentration [2]. It is also important to understand that this is not an electromagnetic interaction.

The migration of charge carriers, due to local electric fields, is called the *carrier drift*. The current density due to drift is proportional to the carrier mobility and electric field [2].

From the charge continuity equation, the rate of change on the number of holes or electrons, $\frac{dn}{dt}$, is given by:

$$\frac{dn}{dt} + \vec{\nabla} \cdot \vec{J} = \text{Generation Term} - \text{Recombination Term} \tag{1.2}$$

where

$$\vec{J_{e/h}} = q(\mu_{e/h} * \vec{E} * \rho_{e/h} \pm D_{e/h} * \vec{\nabla}(\rho_{e/h})) \tag{1.3}$$

where μ is the carrier mobility, D is the diffusion constant, $\vec{E}$ is the electric field, and ρ is the carrier density [2]. '+' is chosen for electrons and '-' for holes.

Several important features can be gleaned from this model. For one, depending on the direction the sensor is biased, the diffusion and drift effects may compete. Furthermore, for generated charge to drift to the readout pixels with minimal spreading, the electric field in the semiconductor must be sufficiently strong. Equation 1.2 also quantifies how unintended generation and recombination effects modify the amount of charge that actually reaches the ASIC, which may or may not correspond to the"true" photogenerated signal. If generation, recombination, and charge transport are well understood, a semiconducting sensor can be fabricated such that incident photons generate a detectable amount of charge carriers

and a meaningful X-ray signal is properly reconstructed.

1.3 Diode Detectors and Pixelated Semiconductors

In the previous section, we motivated the use of semiconductors as the sensor material of choice for Hybrid Pixel Detectors. A discussion of carrier generation, recombination, and transport was included to illustrate that the fabrication procedures and operating conditions of an HPD sensor must be carefully chosen so that photogenerated charge reaches the processing ASIC with minimal signal reduction. In this section, we more precisely model the sensor as an array of PN junction diodes and illustrate how this anatomy is particularly well-suited for photon detection.

1.3.1 PN Junction Diodes

An important consideration for detector operation is the minimization of free charge in the conduction band that was *not* generated by incident X-rays. If there is far less "signal" charge in the conduction band than the ubiquitous, doping-induced holes or electrons, it will be extremely difficult to reconstruct meaningful images. A sensor must be designed and fabricated such that the *leakage current*, or total background current flowing through the sensor, is minimized.

The PN junction diode is one of the most important semiconducting technologies. It consists of a single structure in which a p-doped region with excess holes is face-to-face with an n-doped region with excess electrons. Assume there is no voltage applied across the diode. Then, a fraction of the electrons would diffuse

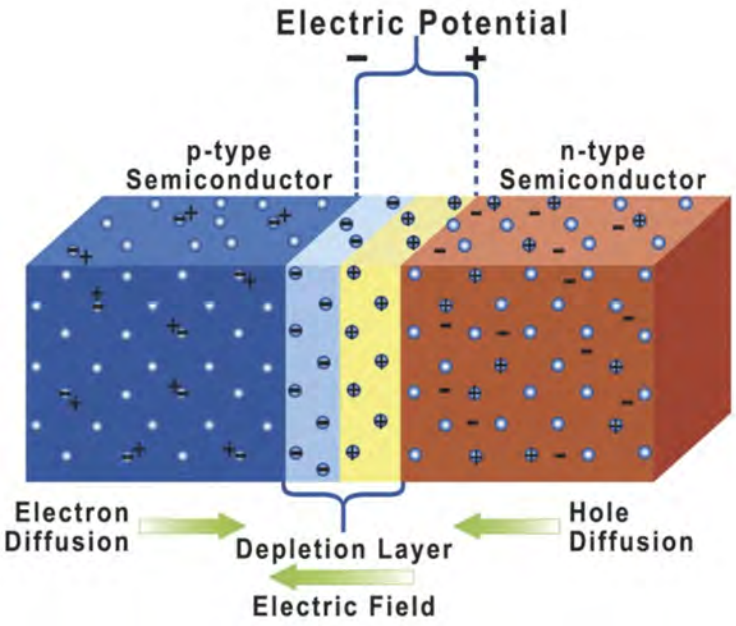

Figure 1.6: PN Junction Diode with no applied bias voltage. The diffusion of charge and the resulting depletion behavior are illustrated [8].

to the p-doped region and recombine with holes near the junction [28]. As a result, the p-doped region acquires a small negative charge and the n-doped region acquires a small positive charge, leading to a internal, "built-in" electric field near the PN boundary [28]. Moreover, all electrons and holes near the junction will have recombined, so the region is depleted of free charge carriers. We call this the *depletion region*, and is characterized by its depletion width.

The depletion width can be modified by applying a voltage bias across the diode. The diode is forward-biased if the p-doped side is placed at a higher potential than the n-doped side (Figure 1.7a). Then, the holes in the p-doped region will drift across the diode through the n-doped region, and the electrons in the n-doped region will drift across the diode in the opposite direction [28]. If a high enough bias is applied, the depletion width effectively goes to 0, and current can pass through the diode with little to no resistance [28].

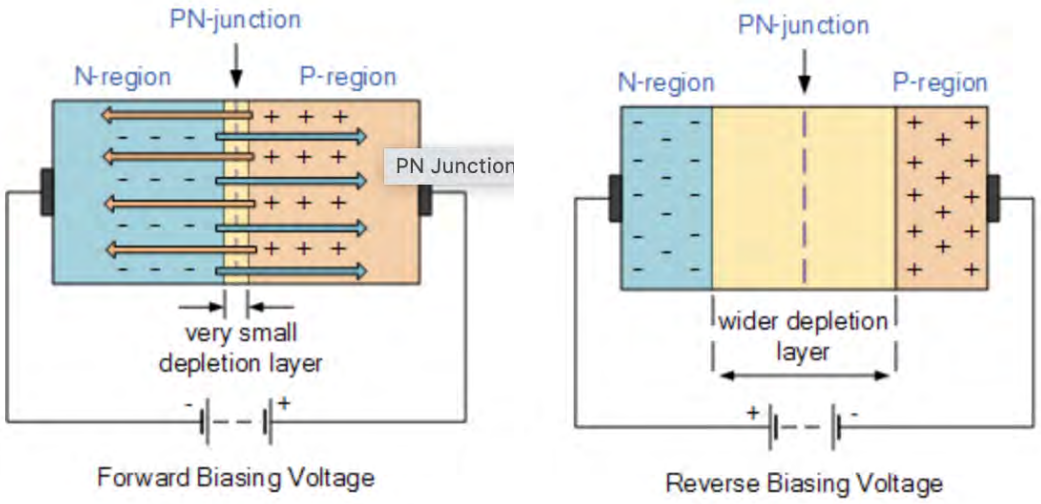

(a) (b)

Figure 1.7: (a) and (b) illustrate the transport of charge carriers in a forward-biased and a reverse-biased PN junction diode [9].

In the inverse scenario, a reverse bias is applied such that the n-doped side is placed at a higher potential than the p-doped side (Figure 1.7b). Now, free charge carriers are drift away from the PN junction, widening of the depletion region and increasing the built-in bias voltage [28]. As a result, the effective diode resistance is arbitrarily large. Assuming reverse breakdown does not occur (the scenario in which a large current in the direction of the bias is produced), the semiconductor may become almost fully devoid of charge carriers [28]. This is known as full depletion.

Clearly, the current that passes through the diode strongly depends on the applied bias voltage. Figure 1.8 shows an IV curve, which encapsulates the aforementioned behaviors under forward and reverse biases.

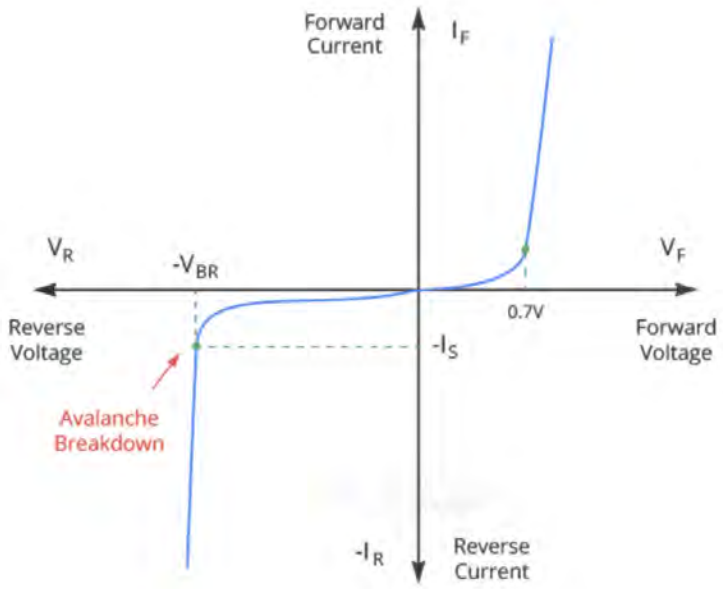

Figure 1.8: Typical IV behavior PN junction diode [10].

1.3.2 Fabrication of Pixelated Semiconductors

Consider a fully-depleted PN junction diode that is exposed to incident X-rays. If a photon is absorbed in the depletion region, a quantity of charge given by Equation 1.1 will be excited to the conduction band. The charge cloud will be accelerated by a strong electric field in the direction of the reverse bias towards one end of the diode, where it can then be "collected" for integration if an ASIC readout system is incorporated appropriately. Since the PN junction diode is fully depleted, leakage current will be minimized, and nearly all collected charge will have been photogenerated. Therefore, with proper fabrication, the PN junction diode is well-equipped for photon detection with a high signal-to-noise ratio. We call these structures *photodiodes* [30]. At first glance, one would expect that a PN junction diode can bonded to a readout sensor and depleted under a reverse bias to produce a photon detector. In fact, this is a rather accurate description of an HPD.

However, the diode structure presented in Figure 1.6 and Figure 1.7 introduces several complications. In particular, since we are interested in the fabrication of a pixel detector, we expect that the sensor structure will be pixelated in some way. Assuming the diode is biased in the z-direction, we hope to determine the signal associated with a given xy position, enabling the reconstruction of 2-D images. Therefore, we hope to fabricate an *array* of photodiodes, each with its own associated integrating electronics. The semiconductor should behave as an array of independently-operating photodiodes but still exhibit a high degree of uniformity from diode to diode. In this idealized model, each "pixel" is represented by a reverse-biased PN junction diode with xy dimensions corresponding to the pixel pitch. However, there does not exist an easy way to isolate the adjacent diodes in the sensor bulk.

Figure 1.9 illustrates a planar or PAD diode [11]. In this model, the sensor bulk is doped uniformly. Oppositely-doped localized implants are added that interface with the readout chip [11]. This creates a PN-junction diode structure at each implant, and a photosenstitive, pixelated semiconductor is assembled. The top of the sensor (sometimes a contiguous metal plate instead of an array of electrodes as shown in Figure 1.9) is typically placed at a high potential using an external power supply to create the reverse bias [31]. Note that the "top" of the sensor is the bottom of the side view diagram in Figure 1.9. The doped implants are also electroded so that incident currents can be collected and processed by the ASIC. The area of the implant is important, as an isolated diode structure must be fabricated without creating an excess of leakage current. The area outside these patches form effective dead regions where signal can be lost, but this patterning is required to pixelate the bottom of the sensor [31]. The doping profile of the sensor bulk and electroded implants requires the top of the sensor to be placed at

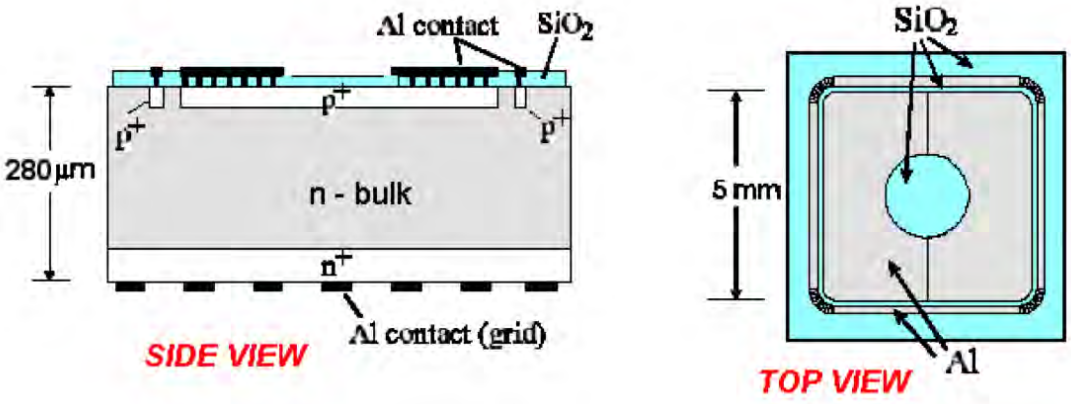

Figure 1.9: Structure of a PAD diode. Note that in the "Side View", the top of the figure corresponds with side of the sensor bonded to the readout chip [11].

either a positive or negative voltage bias - depending on which is required, either electrons or holes will be collected by the electrodes at the bottom. The detector is thus labeled either hole-collecting or electron-collecting, as the ASIC only sees one type of charge carrier.

The implants at the interface with the ASIC are interspersed with an insulating substrate, often SiO_2 for silicon sensors [32]. This reduces the pixel-to-pixel noise and otherwise isolates adjacent implants [32]. This area "between the pixels", particularly the Si/SiO_2 interface, is prone to radiation damage, resulting in an increase in inter-pixel capacitance, thermal noise, and charge trapping at this interface [32]. A quantitative analysis of these effects is not presented in this thesis, though the degradation of the insulating oxide is an important consideration for detector fabrication and can lead to a reduction in detector performance during imaging.

1.4 Notes on Document Organization

Throughout the first chapter of this thesis, I have hopefully motivated several essential ideas. First, and perhaps most important, is that the development of novel X-ray detectors for use at a synchrotron light source is of acute interest to the scientific community. The Hybrid Pixel Detector is a promising technology that is particularly well-suited for these environments and offers distinct advantages. A pixelated semiconductor sensor is typically used for direct X-ray detection with high sensitivity, minimal electronic noise, and a high degree of spatial resolution.

Chapters 2 and 3 introduce more introductory material with the intent to motivate the need for new sensor materials and to illustrate how the Mixed Mode Pixel Array Detector, coupled with our lab's detection setups, is well-equipped to identify and address existing limitations in sensor materials. Chapter 2 introduces a specific subset of HPDs that were characterized in this thesis: high-Z semiconducting sensors bonded to the MMPAD. Chapter 3 shifts to a discussion of X-ray science and the experimental setup used to characterize detectors. Chapters 4-8 present the important results of this work. Chapter 4 is a full characterization of a silicon MMPAD; though not a high-Z detector, silicon exhibits the characteristics of a capable material and lends itself well to the suite of measurements we would ideally be able to conduct for all detectors. Chapters 5-8 introduce high-Z alternatives to silicon and discuss the advantages and limitations of each sensor material. Chapter 9 highlights key outcomes from these studies and briefly discusses future work in X-ray detection and synchrotron science.

CHAPTER 2

MOTIVATION FOR THE HIGH-Z MIXED-MODE PIXEL ARRAY DETECTOR

In Chapter 1, we demonstrated that a semiconductor with a collection of PAD diode implants can behave as an array of photodiodes if fabricated properly. However, we did not address the material identity of the sensor itself. The semiconductor must be chosen carefully to optimize detector performance. In this chapter, we demonstrate that the most widely used sensor material for X-ray detection, silicon, is largely transparent at higher photon energies [6]. A larger fraction of high energy photons are detected by materials with a higher atomic number (high-Z sensors), but much work is required to improve other metrics of detector performance. Later chapters strive to identity and address these concerns. We also demonstrate that the MMPAD is well-equipped for continuous X-ray imaging and that it provides the ideal readout architecture for our investigation of high-Z sensors. In particular, the "mixed mode" nature of the readout is defined and motivated.

2.1 The Need for High-Z Materials

A high-performing of an X-ray detector should be nearly optimized with respect to three essential metrics. The first, and most fundamental, is fraction of incident X-ray photons that generate electron-hole pairs. The second is the generation and transportation of free charge generated by the absorbed photons and the minimization of excess background currents that can obscure the signal. The third is the high-speed processing of the collected signal to produce meaningful radiographs. The first two attributes are determined by the fabrication and physical

capabilities of the sensor layer. The third requires well-designed ASIC readout.

Silicon can be produced cheaply with few defects, exhibits fast and efficient charge transport due to high carrier mobilities, has minimal dark and leakage currents, and is mechanically robust [6]. The widespread use of silicon sensors can be largely attributed to these advantages. However, a given X-ray photon with an energy greater than 20 keV is unlikely to be absorbed by silicon. Thus, silicon performs poorly with respect to the first of the aforementioned metrics in this energy regime. Mathematically, the quantum efficiency (the fraction of absorbed photons) is defined by:

$$A_Q = 1 - e^{-\alpha L} \tag{2.1}$$

where A_Q is the quantum efficiency, α is the linear attenuation coefficient (a function of the material and the photon energy), and L is the sensor thickness [31]. For silicon exposed to high energy X-rays, α is small, so a very small portion of the incident photons are absorbed unless the sensor thickness is increased to the point at which spatial and temporal resolution, charge transport, and other essential metrics are reduced dramatically.

Figure 2.1 compares the quantum efficiency of silicon with two high-Z materials: germanium and cadmium telluride. The quantum efficiency at high energies is superior in high-Z materials, and if these materials exhibit strong performance in other metrics, the overall detection efficiency will likely be much higher than silicon. A low quantum efficiency represents a fundamental limitation of a sensor that largely cannot be corrected without entirely changing the material. Charge transport, leakage current, and other sensor attributes can be altered with doping and other aspects of fabrication. Thus, even though many high-Z materials do not perform as well as silicon at the moment, even at high energies, their limitations

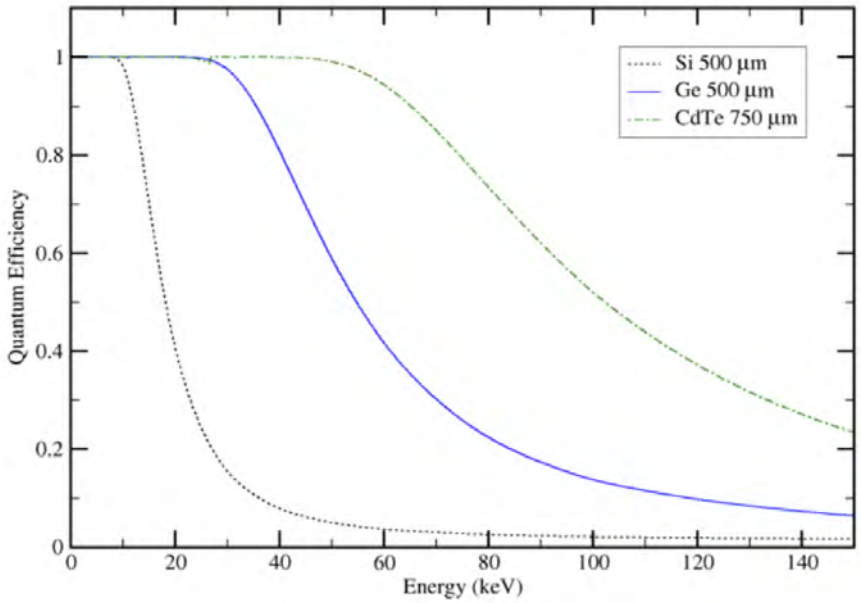

Figure 2.1: Comparison of silicon, germanium, and CdTe quantum efficiency as a function of photon energy.

are almost certainly easier to correct than silicon's. This thesis strives to identify these areas of poor detector performance and attribute them to some physical behavior of the sensor itself.

2.2 Operation of the Mixed-Mode Pixel Array Detector

An important aspect of sensor characterization is the change in sensor behavior (charge collection efficiency, leakage current, etc.) after an extended exposure to a radiation source. This requires continuous data acquisition and processing with a wide dynamic range. The MMPAD is a novel detector that was designed and assembled in the early 2000s by the Gruner lab. Its unique processing capabilities, particularly in charge integration and removal, enable continuous imaging on millisecond time scales, providing the perfect functionality for the characterizations we intended to conduct [2].

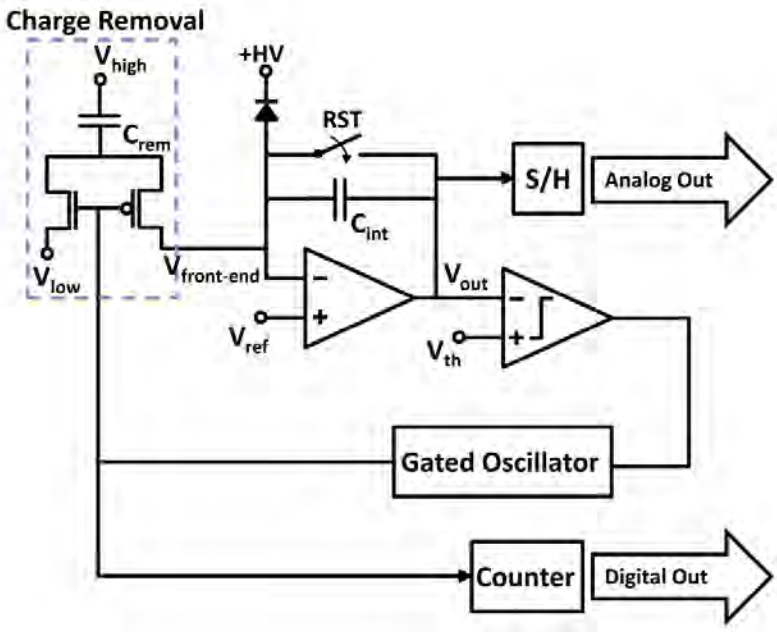

Figure 2.2: Schematic of the electronics of a single MMPAD pixel [1].

The MMPAD combines the strengths of digital and analog Pixel Array Detectors (PADs) while circumventing their limitations. Digital PADs, commonly used in high energy collider experiments, register data that surpasses a given threshold and digitizes it immediately upon acquisition [2]. This practice improves signal/background discrimination and enables fast readout [2]. However, the processing of the signal associated with a single photon is somewhat slow, so most digital PADs do not perform well at a synchrotron [2].

On the other hand, analog PADs process and store photogenerated charge via analog circuity, much in the spirit of a CCD [2]. Digitization does not occur until data collection is finished [2]. The framing rate is superior to a digital PAD, but the well depth of a pixel (how much charge can be stored) is inversely related to the pixel size [2]. This limits either the spatial resolution or dynamic range of the detector once one of the two is fixed.

Figure 2.2 is a schematic of the MMPAD electronics for a single pixel. Incoming current from the sensor is integrated/stored in the C_{int} capacitor, much like an analog PAD. Once the stored charge on the integrating capacitor reaches a certain threshold, the charge removal mechanism is triggered and a digital count is registered. At the end of the exposure time, the charge currently stored on the capacitor is registered as an analog signal. The "digital" signal corresponds to the number of times the charge removal mechanism has been activated throughout the exposure time. The total signal is determined by combining the analog and digital counts on a pixel-by-pixel basis to create a total intensity in analog-to-digital units (ADU). An ADU intensity is computed via the following formula:

$$\text{ADU intensity} = (\text{digital counts}) * (\text{analog-to-digital multiplier}) + (\text{analog counts}) \tag{2.2}$$

Physically, the analog-to-digital multiplier represents the amount of charge stored in the integrating capacitor when the charge removal mechanism is triggered. This depends on the values of the MMPAD voltages, particularly V_{ref}, V_{low}, and V_{th}. The multiplier must be computed after these voltages are set by the user, which must be chosen carefully for the detector to operate correctly. Before taking meaningful data, a calibration procedure for the MMPAD should be conducted, in which the optimal values V_{ref}, V_{low}, and V_{th} are chosen and the corresponding analog-to-digital multiplier is computed.

The most important innovation of the MMPAD was the development of a charge removal mechanism that actively operates during data collection. The collection of analog and digital data simultaneously and the combination post-exposure enables detection akin to that of analog PADs, in which data can be collected in a high-flux environment. The periodic digitization and charge removal bypasses the limitations

Parameter	**Value**
Pixel Array Dimension	128×128 pixels
Pixel Pitch	150μm×150μm
Well Size	4×10^7 8 keV X-rays
Frame Rate	1 kHz
Maximum Flux	$>10^8$ X-rays/(pix/s)

Table 2.1: Imaging specifications of the MMPAD [1, 2].

associated with a small charge well, and continuous imaging is made possible.

CHAPTER 3

X-RAY PHYSICS AND THE IN-LAB EXPERIMENTAL SETUP

Throughout this thesis, we have emphasized that synchrotron X-ray imaging is the main application of the high-Z detectors we characterized. However, beamtime at light sources is often limited, so it is not feasible to fully characterize a collection of high-Z sensors at a synchrotron. The Gruner/Thom-Levy lab has developed an in-house X-ray machine that, though photon energy and flux is limited, mimics the imaging conditions at a synchrotron. The group often characterizes particularly interesting or promising sensors at CHESS after a set of in-house measurements. The data presented in this thesis was taken in the lab.

However, since it is impossible to construct a storage ring in the lab from which X-rays can be generated via synchrotron radiation, we exploit different phenomena to produce photons in the X-ray regime. In particular, we generate of continuous emission spectra via *bremsstrahlung* with well-defined peaks at *characteristic energies*. In this chapter, I'll more precisely describe these X-ray generation mechanisms and present other techniques used to modiofy the photon energies to which the sensor is exposed.

3.1 In-Lab X-ray Production

At the beginning of Chapter 1, the significance of X-ray radiation was emphasized, particularly as a means to probe matter at atomic scales. A rich connection between X-rays and the atomic structure of common materials is thus anticipated, and it turns out that the energy "stored" in atomic structures often can be extracted in the form of X-ray photons.

An X-ray tube is a technology that can generate X-ray photons by bombarding a material with electrons [33]. Its most important constituents are a cathode and an anode that are surrounded by metal housing [33]. A voltage difference between the cathode and anode can be applied. Separately, the cathode (usually a tungsten filament) is heated by an applied current such that electrons are thermally excited out of the filament and into the tube itself. The electrons are then accelerated to the anode by the applied electric field. The interactions between the electrons and the anode generate X-ray photons that are diverted towards the detector. The energy spectrum of the photons depends on the choice of material for the anode, and we typically name a tube after the identity of its anode (i.e. we have a silver (Ag) tube, copper (Cu) tube, etc).

The group has developed the technology to specify the voltage at which the tube is biased and the current that passes through the filament. A stronger bias increases the energy at which electrons strike the anode, and the electron charge times the applied bias represents the maximum energy of a generated photon. Note that a larger current increases the number of electrons excited out of the cathode, but does not affect the X-ray emission spectrum. The maximum voltage at which the X-ray tube can be biased is 47 kV (corresponding to a maximum photon energy of 47 keV). This is somewhat lower that typical synchrotron energies, in which the average photon energy can be closer to 70-80 keV. Moreover, the maximum flux from the X-ray tube ($\sim 10^7$ X-rays/s/mm^2) is much less than that at a synchrotron ($\sim 10^{11}$ X-rays/s/mm^2) [2]. With the increased energy/flux requirements at a synchrotron, even if a detector performs well in-house, strong performance at a synchrotron cannot be assumed. However, if a detector does not perform well at the lab, it is likely to be insufficient for synchrotron experiments.

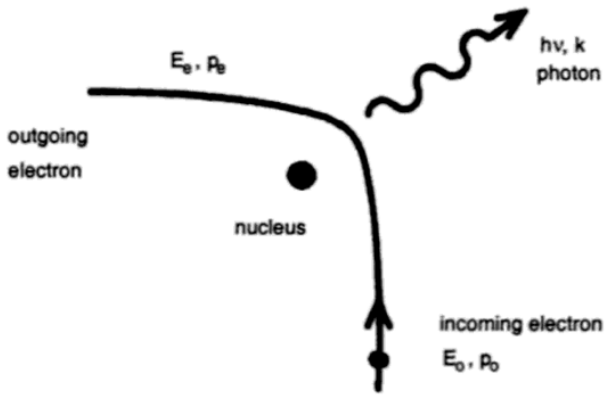

Figure 3.1: Electron-nucleus Coulomb scattering generates bremsstrahlung photons [12].

3.1.1 Bremsstrahlung and Characteristic Radiation

The production of X-ray photons, or any type of electromagnetic radiation, is an extremely rich and complex phenomenon. This thesis is geared more toward a discussion of the interactions of X-rays with matter (specifically semiconductors) than the generation of the X-rays themselves - the reader would be better off reading a textbook on electrodynamics if a more complete understanding of these interactions is desired. Nevertheless, we will briefly introduce the predominant mechanisms that generate radiation in the X-ray tube.

Bremsstrahlung radiation is produced by the deceleration of an electron after electromagnetically scattering off the nucleus of an atom [12]. In the X-ray tube, the thermally-excited electrons scatter off the anode material to generate bremsstrahlung. Assuming sufficiently large electron energies, the recoil of the nucleus can be ignored, and the energy of the generated photon is given by

$$E_{photon} = E_f - E_o \tag{3.1}$$

where E_o and E_f correspond to the initial and final energies respectively of the

incident electron during the scattering process [12]. The emission spectrum due to bremsstrahlung is given by Kramer's Law

$$I(\lambda) = K(\frac{\frac{\lambda}{\lambda_{min}} - 1}{\lambda^2}) \tag{3.2}$$

where I is the intensity of the photon count at a given wavelength, K is a property of the target material (proportional to its atomic number), and λ_{min} is the minimum possible wavelength of the emitted photon determined by the energy of the incident photons [34]. The result is continuous spectrum that goes to 0 at λ_{min} and diverges at long wavelengths. However, the energy flux associated with these near-0 energy photons is finite, so the expression is still physical [34]. When the emission spectra of a source is measured in the lab, typically using a particular photon-counting detector called a drift detector, we exclude the large wavelength portion of the spectrum, as the photons lack sufficient energy to meaningfully interact with the detector.

The emission spectrum also has sharp peaks at certain photon energies. These peaks were generated via characteristic radiation, a mechanism in which incident particles (electrons in our case) ionize inner shell electrons, accompanied by the de-excitation of an outer shell electron to inhabit to inner state vacancy. The energy lost in de-excitation is carried away by a photon. For our anodes, the dominant atomic transitions were from the n=2 to the n=1 and n=3 to the n=1 energy levels of the material [13]. The photon emissions associated with these transitions are denoted kα and kβ radiation respectively. Since atomic energy levels are discrete, kα and kβ radiation produces sharp peaks corresponding to the spectral lines of the anode material.

The number of generated bremsstrahlung and characteristic photons is of the same order of magnitude, so the average photon energy can by modified signifi-

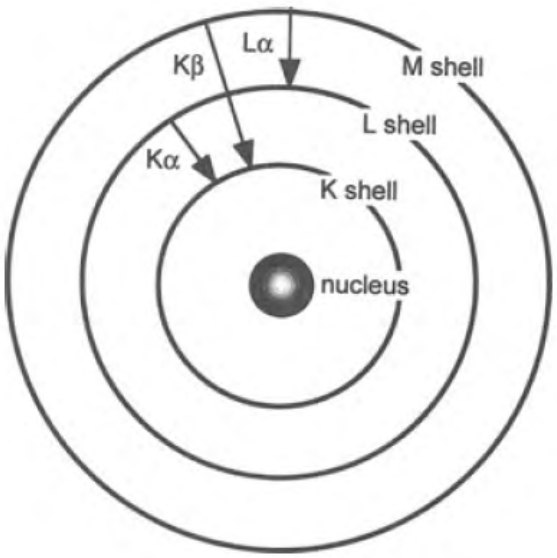

Figure 3.2: Electron transitions generate characteristic radiation with energies determined by the atomic structure of the anode material [13].

cantly by either changing the voltage at which the tube is biased or by using an entirely different tube with a different anode material. In the next section, we introduce another technique to modify the energy spectra: the insertion of filters to exclude a fraction of photons with a given energy.

3.1.2 Use of Filters to Modify Emission Spectrum

Our lab's X-ray setup includes a small rectangular slot directly after the X-ray shutter where a thin filter can be inserted. X-ray photons must pass through the filter before traveling through the beam pipe and reaching the detector. Since different materials have different attenuation behaviors, given by Equation 2.1, a material with a particular thickness can be placed in this slot to absorb photons with certain energies. One downside is that the total flux to which the detector is exposed can decrease significantly if too much material is inserted. The highest

average energy we can achieve in the lab without reducing the flux too dramatically is 24 keV, for which we use an Ag tube with a 1 mm Al filter. Silver has the greatest characteristic energies out of the X-ray tubes available to us, and aluminum absorbs the majority of the low energy radiation. Figure 3.3 illustrates how the voltage at which an X-ray tube is biased and the application of a filter affects the emission spectrum. The total energy incident on the detector is more similar than the average photon energies would suggest, as the flux decreases with the Al filter in place.

3.1.3 Production of Monochromatic Illumination

We have illustrated that the emission spectrum and average photon energies of our in-lab X-ray source can be controlled with reasonable precision. However, certain measurements (see Section 4.4.1 for example), require *monochromatic* illumination that consists of a single energy. Bremsstrahlung emissions cannot be avoided, and a filter can only modify emission spectra very roughly. For the majority of exposures, *flood illumination* is used, in which the entire face of the sensor is exposed to the full photon spectrum.

We use a graphite *monochromator* to modify the beam such that certain areas of the detector are exposed to monochromatic illumination. According to Bragg's Law, electromagnetic radiation incident to a crystal interferes constructively if the following condition in satisfied:

$$\lambda = 2dsin(\theta) \tag{3.3}$$

where d is the distance between successive layers in the crystal lattice and 2θ is the scattering angle. The X-rays incident to the graphite crystal occupy a range of

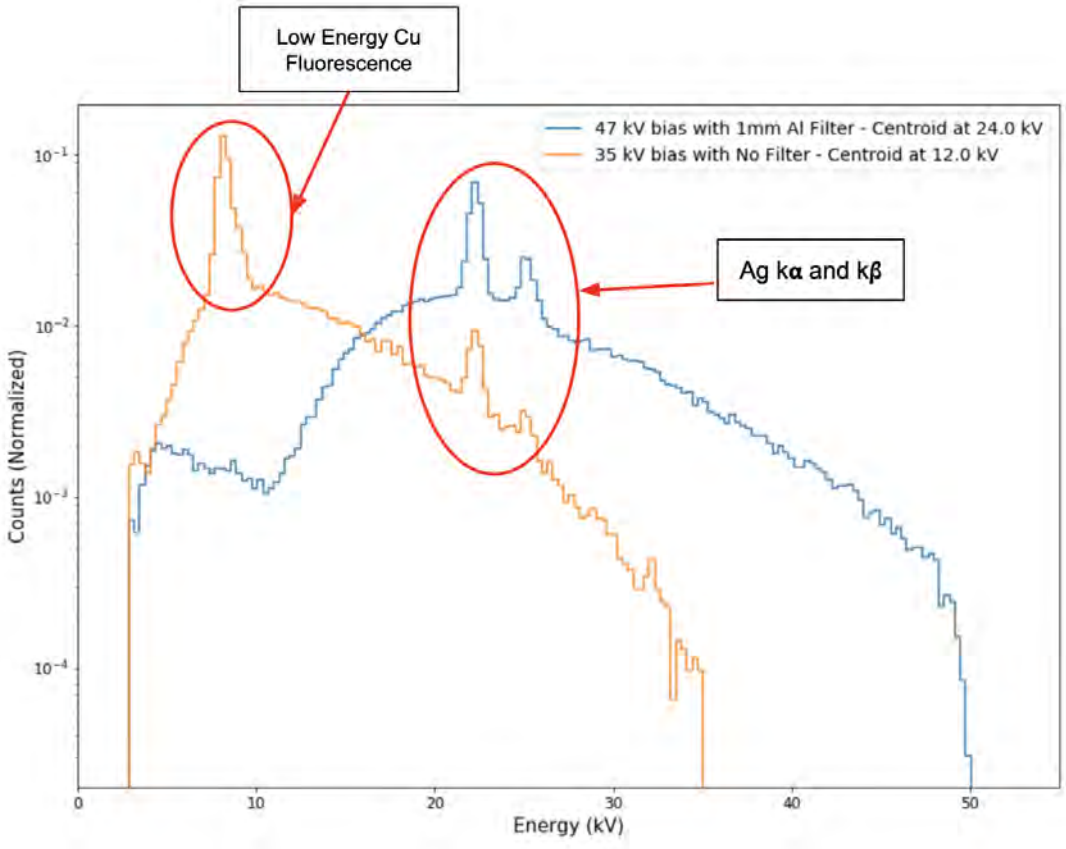

Figure 3.3: Normalized emission spectra for an Ag tube biased at 47 kV with a 1 mm Al filter and the same tube biased at 35 kV with no filter. A larger range of bremsstrahlung energies are detected at a higher bias, as the endpoints of the emission spectra are determined by the maximum energy of electrons incident to the anode. An excess copper fluorescence due to the brass in the beam pipe is observed only when the Al filter is not in place. This also increases the average energy with the Al filter substantially.

wavelengths and the beam occupies a finite solid angle, so radiation scatters off the crystal at a variety of angles. The condition prescribed in Equation 3.3 effectively "picks out" λ-θ combinations that correspond with constructive interference, and regions of the detector at a given θ relative to the graphite are uniformly illuminated by radiation of a single energy. All sensor pixels in a given row are at the same angle relative to the crystal, so the incident energy changes continuously and monotonically on a row-by-row basis. If flood illumination is desired, that X-ray tube can be aligned such that X-rays do not interact with the graphite crystal.

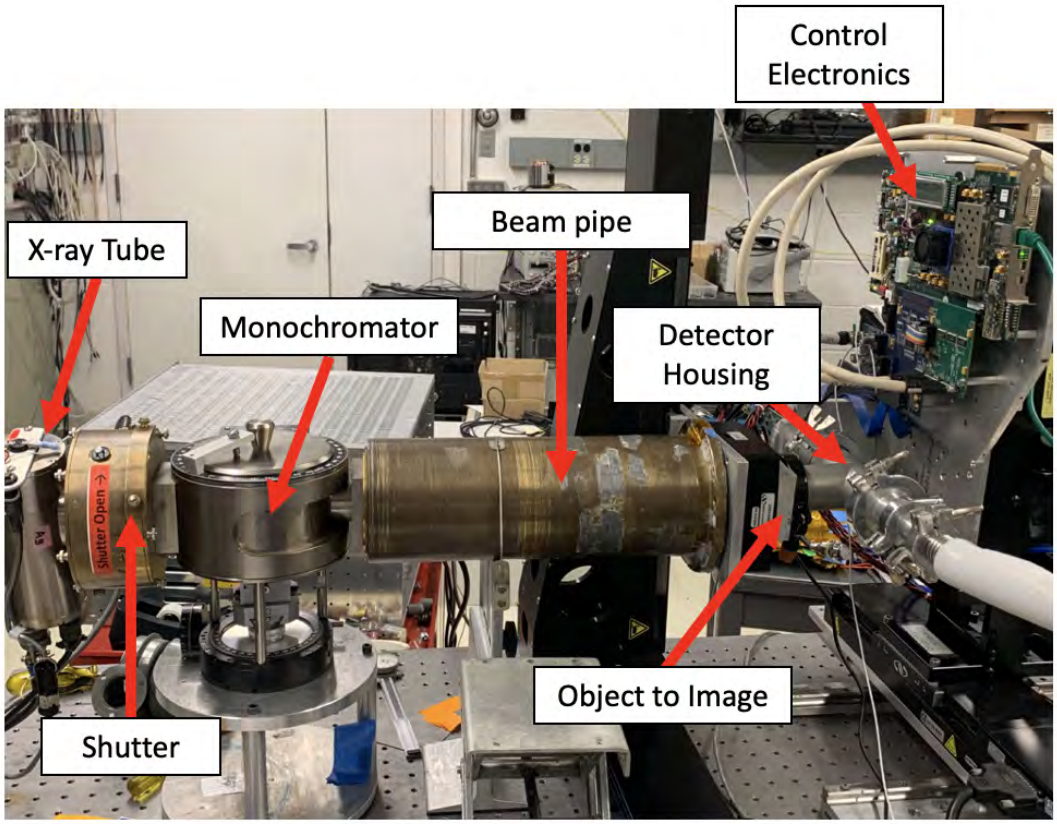

Figure 3.4: Experimental setup used for sensor characterizations at room temperature.

3.2 Experimental Setups

The Thom-Levy/Gruner lab uses two experimental setups for PAD imaging: one for room temperature characterizations and another for characterizations that must be conducted at cryogenic temperatures (the cryostat). Figure 3.4 is a labeled diagram of the apparatus for room temperature characterizations.

The setup consists of the X-ray tube, a shutter that can be opened or closed to block generated photons from reaching the detector, the graphite monochromator, a short beam pipe through which the X-rays travel, the detector housing (which can be changed depending on the operating conditions for a given sensor), and the

control electronics for readout to the computer. An object can be placed directly after the beam pipe and the corresponding reconstruction of the pattern by the detector can be ascertained. From this, the contrast, resolution, and other metrics of performance can be evaluated. The temperature is manually set to a constant value (near room temperature) using a thermoelectric cooler and a water chiller. The sensor is also placed under a vacuum and biased using a Keithley power supply that can provide just over 1,000 volts. The selenium, lead perovskite, and CZTS sensors were characterized using this setup.

Figure 3.5 presents the cryostat. The same X-ray setup is implemented, but the detector is placed in more rigid housing. An insulating chamber that can hold liquid nitrogen (behind the silver box of control electronics in Figure 3.5) is placed adjacent to the detector that can cool the detector down to $\sim$ -175^{o}C if completely filled. A PID temperature controller is programmed that, when connected to an external power supply, can roughly control the rate of sensor cooling and heating. The output from the temperature controller/power supply can only warm the system with at most a 50 W output. Moreover, cooling is done manually by adding more liquid nitrogen to the insulating chamber, so temperature control is somewhat imprecise. Like the room temperature setup, the detector is placed under vacuum and biased by a Keithley power supply. The silicon and germanium sensors were characterized in the crysotat.

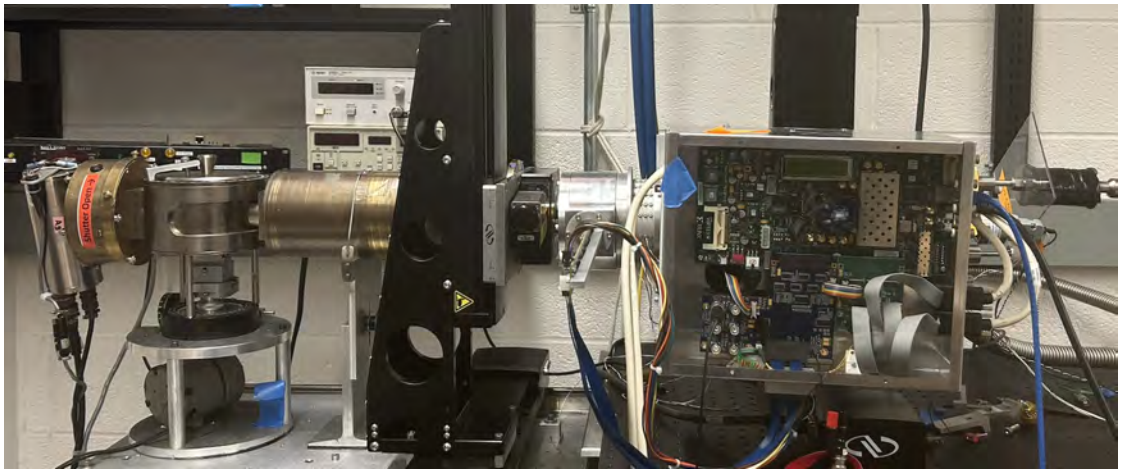

Figure 3.5: Cryostat used for characterizations at cryogenic temperatures.

CHAPTER 4

CHARACTERIZATION OF THE SENSOR BEHAVIOR AND IMAGING PERFORMANCE OF DOPED SILICON

4.1 Properties of Silicon Semiconductors, Production, and Operating Conditions

Silicon is the most widely used sensor material for both synchrotron X-ray detection and charged particle tracking in collider experiments such as CERN and Belle [35]. This is can be attributed to a variety of factors, including its versatility as a material, the existence of cheap methods of production, and the lack of pronounced defects in the bulk of the semiconductor relative to other candidate materials [11]. These properties have led not only to the popularity of doped silicon in radiation detectors, but also in fundamental semiconducting technologies such PN-junction diodes and CMOS structures. This particular sensor, denoted the Si-f50, has been characterized by the group in previous studies and is generally considered high-performing and well-understood. I present this characterization in the thesis to illustrate detector behavior when the sensor works *well*. This should provide helpful context from which the results of our germanium, selenium, perovskite, and CZTS characterizations can be better understood.

At high temperatures (around 300 K), silicon has an *indirect* band gap of 1.2 keV, meaning that the distance between the conduction and valence bands varies with crystal orientation. An incident photon can excite an electron to the conduction band if the interaction is accompanied by a lattice vibration, or phonon, that adjusts the crystal lattice's k-vector to make the transition energetically favorable

[11]. In silicon, electron excitation from the valence band to the conduction band can also occur at locations of crystal defects, in which an electron can temporarily inhabit a trap state in the band gap [29]. At these defect locations, the band structure is discontinuously modified so that excitation may be possible without phonon emission [29].

Silicon wafers enjoy relatively few defects and phonons are generally uncommon at cryogenic temperatures, which brings about an effective direct band gap of 3.6 keV when used in the cryostat [11]. As a result, low-temperature imaging reduces dark current significantly, though room-temperature imaging is still feasible and used in many experiments. Silicon's main drawback is again its low quantum efficiency, which results in significant signal reduction at X-ray energies above 15 keV.

This particular sensor, which we call the Si-f50, consists of a commercially-purchased, 200 μm thick, high resistivity silicon wafer that was solder bump-bonded to an MMPAD. The Si-f50 has 3 dead pixels. Intensities from these pixels were considering in our analysis, but had little to no effect on measured quantities.

The first set of characterization measurements were taken with the sensor at approximately -170^{o}C and placed under a 150 V voltage bias. The sensor was cooled from room temperature to -170^{o}C continuously in just over 20 minutes. Figure 4.1 provides a timeline for the cooling of the Si-f50 sensor. The sensor was fully depleted, so the vast majority of charge carriers were thermally generated. Thus, the bias current at a given temperature/time is expected to be proportional to the dark current. Our characterization of the Si-f50 sensor at -170^{o}C corresponded to a bias current of approximately 1.8 nA.

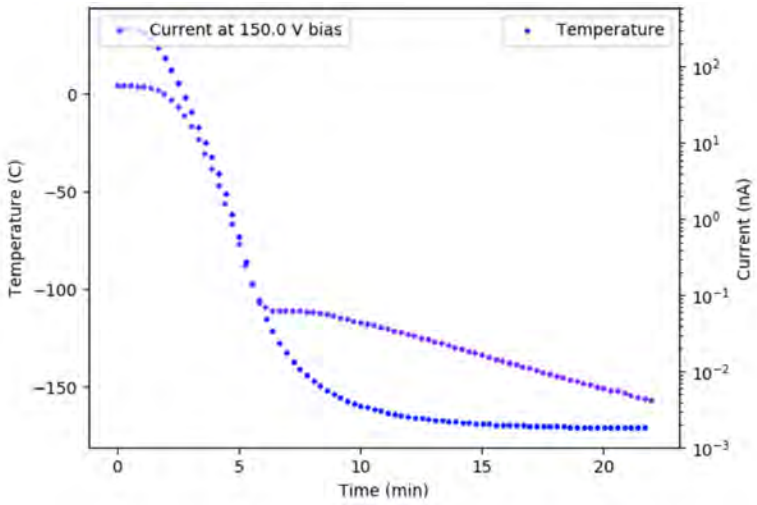

Figure 4.1: Thermal history and bias current behavior during liquid nitrogen cryogenic cooling of Si-f50 sensor. The sensor was biased at 150 V.

4.2 ASIC Noise and Sensor Dark Current

We quantified the readout noise by taking 100 background-subtracted dark images with a 1 ms collection time. Then, we histogrammed the intensity of each pixel for each frame (in ADU), from which the ASIC noise associated with a 1 ms readout is approximately the standard deviation of the resulting histogram. An intensity pattern with geometric regularity is visible in the frame-averaged background-subtracted dark image (Figure 4.2a). We attribute this to fluctuations in the MMPAD's internal power supply, which applies the relevant amplifier voltages to the ASIC pixels. Therefore, the Si-f50's ASIC noise is predominately due to systemic error associated with the experimental setup as opposed to any frame-by-frame or pixel-by-pixel variations in the collected charge.

Figure 4.1 provides further verification that the dark current is sufficiently low, especially at cryogenic temperatures. Upon reaching the target temperature at $\sim$ -170^{o}C, we more precisely quantified the dark current through the pixels. At T = -171^{o}C, we collected and averaged 100 dark images with a 100 ms collection time,

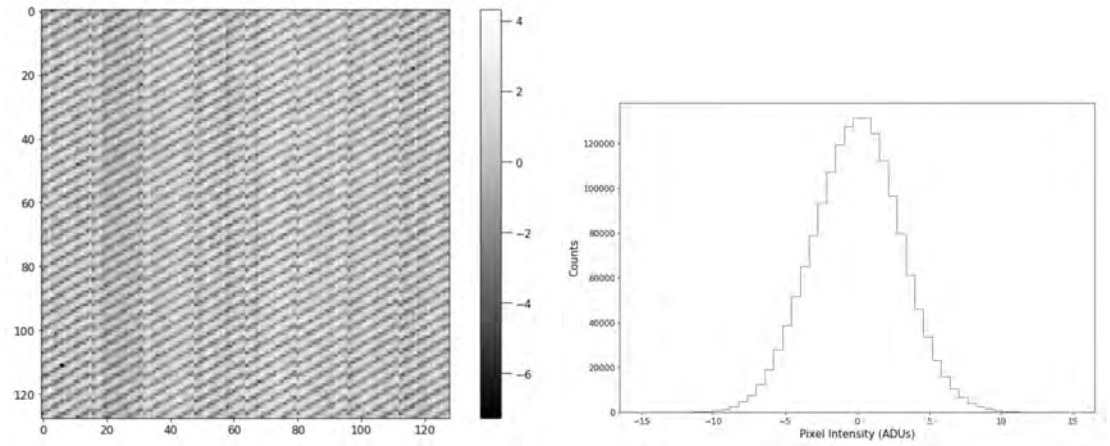

(a) (b)

Figure 4.2: (a) is the average of 100 frames, each with 1 ms integration time, for a background-subtracted dark image taken with the Si-f50 sensor. (b) shows the distribution of the non-averaged ADU pixel intensities from the same set of frames. The standard deviation of the data set, which we define as the ASIC readout noise, is 3.03 ADU.

and subtracted the existing background that corresponded to a 10 ms collection time. Dividing the pixel intensities by 90 ms gave an averaged image for which the pixel intensity corresponds to the dark current in ADU/ms. However, the dark current image replicates the same geometric pattern as Figure 4.2, which suggests that the dark current is largely minimized relative to the readout noise. Figure 4.3 displays the frame-average dark current image alongside its pixel-by-pixel intensity histogram. Since the noise profile is centered about 0, the average pixel dark current, relative to the noise, is the mean of the histogram. We found this was 5.136 ± 0.008 (ADU/ms)$*10^{-4}$.

The ADU values for the readout and dark current noise can be better understood after computation of the ADU to keV conversion described in section 4.4.1. Then, the readout noise and dark current can be quantified in terms of an equivalent photon signal.

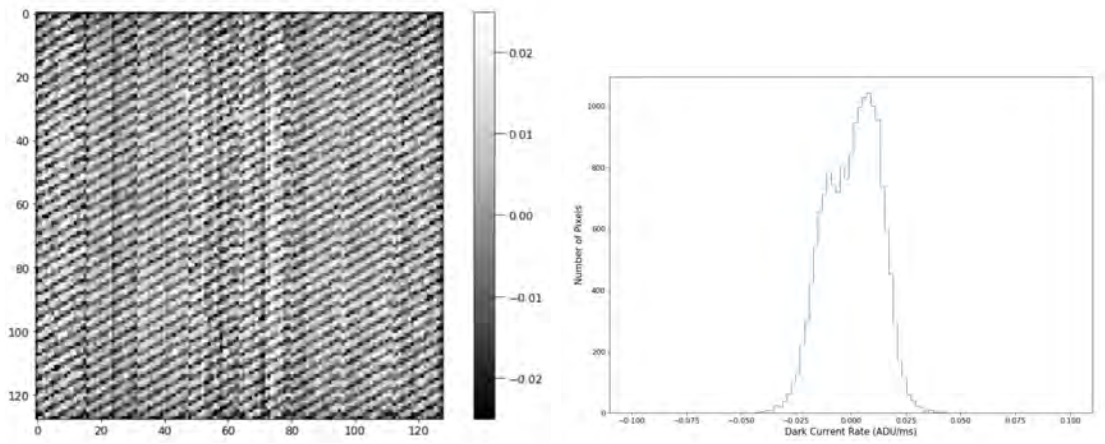

(a) (b)

Figure 4.3: (a) is an image of the Si-f50 dark current collected at -171^{o}C, in ADU/ms. (b) shows the distribution of the averaged ADU pixel intensities from (a). The average pixel dark current is given by the histogram mean of 5.136±0.008 (ADU/ms)*10^{-4}

4.3 Qualitative Imaging Performance

The most straightforward metric of detector performance is whether a two-dimensional projection of a known object can be constructed with the appropriate contrast, resolution, uniformity, etc. Fundamentally, these images show that at a very basic level, the sensor is photosensitive and lacks large-scale defects that would affect localized regions of connected pixels. The Gruner/Thom-Levy lab uses various accessible objects to do this, including a line pair mask and a small lightbulb.

A line pair mask is a thin rectangle that consists of straight lines of no foil and varying width that are parallel to the short edge of the rectangle. The attenuation length of X-rays in lead is extremely small, so if a point X-ray source is assumed, the pixels directly behind the lead should have no intensity, while the remainder of the mask should transmit all photons and yield the same intensities as if the mask was not present. This allows for the reconstruction of high-contrast image,

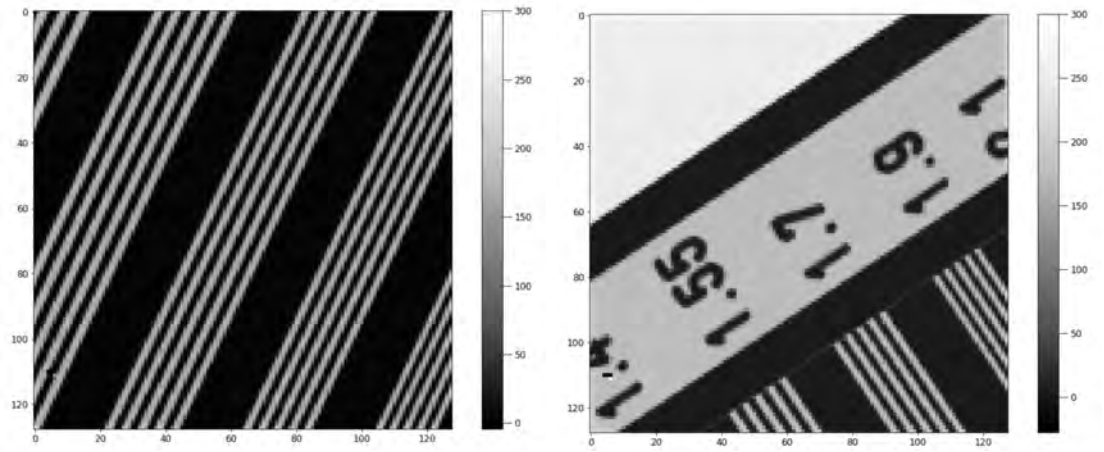

(a) (b)

Figure 4.4: ADU Images of a line pair mask at different orientations. These images were taken with 47 keV X-rays from an Ag anode with a 1 mm aluminum filter in place. Both images were computed via a background-subtracted average of 1000 frames with a 1 ms integration time.

assuming adequate detector performance. Figure 4.4 presents two X-ray images of a line pair mask. The line pair mask was exposed to flood illumination from the Ag tube biased at 47 kV with a 1 mm aluminum filter in place. Alternating strips of high and low intensity are present, and the numbers, which give the width in millimeters of a given line from which the lead was cut, are easy to read. This qualitatively suggests that the Si-f50 is capable of producing high contrast images with a resolution far less than a millimeter.

Figure 4.5 presents an X-ray image of a lightbulb and further validates the performance of the Si-f50. The 2-D projection of the lightbulb has high contrast around the inner filament. This shows that, like a medical radiograph of a human arm that shows bone (Figure 1.1a), the detector system is sensitive to attenuation differences in the material through which it propagates, both transverse to the incident beam and in its direction of propagation. Therefore, in this energy regime and for a sample with properties similar to that of the lightbulb, the Si-f50 is

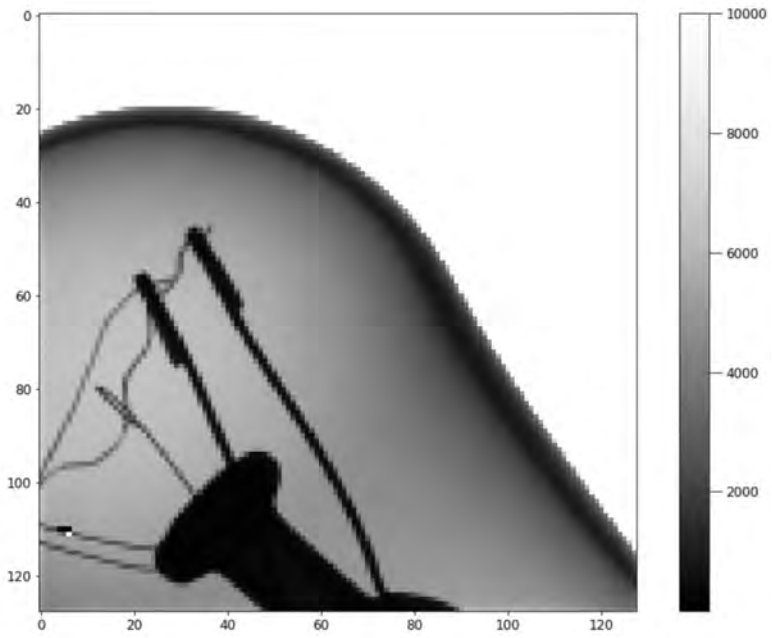

Figure 4.5: ADU Image of a small lightbulb taken with X-rays from an Ag anode biased at 47 kV with a 1 mm aluminum filter in place. This image was computed via a background-subtracted average of 400 frames with a 100 ms integration time.

capable of discerning features of an object in all three spatial dimensions, even though the resulting X-ray image is only two-dimensional.

4.4 Metrics of Sensor Performance

Here we present several quantitative measurements that are particularly important for assessing the imaging performance of the Si-f50 sensor. First, we used a pinhole mask with monochromatic illumination to determine the sensor *gain*, or the number of ADU registered per keV of incident energy. The gain can be computed by histogramming the registered pixel-by-pixel ADU intensities from photons of a known energy. Each peak corresponds to an integer number of detected photons, and measuring the spacing between adjacent peaks yields the desired quantity. Moreover, we quantified the uncertainty associated with the detection of single

photons and compared with the readout noise. Next, we investigated the sensor response to flood illumination to quantify variations in the pixel-by-pixel response and to determine if there exists any systemic non-uniformities in the experimental X-ray source. Lastly, we quantified the spatial resolution of the Si-f50 for our setup by computing the edge spread function of the sensor from the response to a step-function illumination.

4.4.1 Measurement of Sensor Gain and Single-Pixel Uncertainty

The gain of a sensor is one of the most important and potentially illuminating measurements in sensor characterization. For the MMPAD setup, it determines the conversion from ADU to keV, which allows for all images to be expressed in the more meaningful representation of energy per pixel, or photons per pixel if the X-ray energy is known and uniform. Moreover, it highlights the *response* of the material, or how much photogenerated charge reaches the readout. If the energy of incident photons and activation energy of the semiconductor are known, then the gain helps define the overall sensitivity of the sensor, which depends both on the quantum efficiency and the charge-collection efficiency. This provides a common basis for which different sensors can be compared.

We compute the gain by constructing a setup in which incident radiation with a known energy interacts with a subset of pixels. By determining the ADU signal in this subset of pixels, the ADU to keV ratio can be determined. The most straightforward way to create this setup was to manipulate the X-ray source so that a given set of pixels are incident to a known, single-valued energy. The

graphite monochromator, described in Chapter 3, can be used to ensure that a given row of pixels are incident to photons of the same energy. Thus, using the silver tube, we adjusted the monochromator by hand until there was a clear set of adjacent rows that read out a far stronger intensity than the rest of the chip. We deduced that incident radiation must have the energy of the kα silver line (22.1 keV), as there exists a strong peak in the emission spectra of silver at that energy. We limited our analysis to this brighter set of rows since the photon energy was known.

Next, we needed a means to ensure that photogenerated charge cloud from the kα photons would be absorbed by a single pixel - if the signal was shared between adjacent pixels, it would be impossible to determine the (likely fractional) number of photons associated with a given intensity. We met this constraint by placing a tungsten pinhole mask directly in front of the detector. The pinhole mask consists of 25μm holes, and an incident photon is completely absorbed by the mask unless it passes through one of these small holes. Since the individual pixels are larger than these holes, if the center of a hole is aligned with a given pixel, charge sharing between pixels will be minimized, as the width of the generated charge cloud will be less than side length of the square pixel.

Figure 4.6 is an image of the 25μm pinhole mask with monochromatic illumination. The higher intensity rows correspond to the regions illuminated by kα radiation - for each "bright" pixel in these rows, we compared the intensity of that pixel with each of its neighbors. If the pixel intensity was higher than its neighbors by a sufficient amount, i.e. charge sharing between pixels was minimized, said pixel would be included in the resulting analysis. We denote these "isolated" pixels.

For a given frame, the number of photons incident to an isolated pixel is an

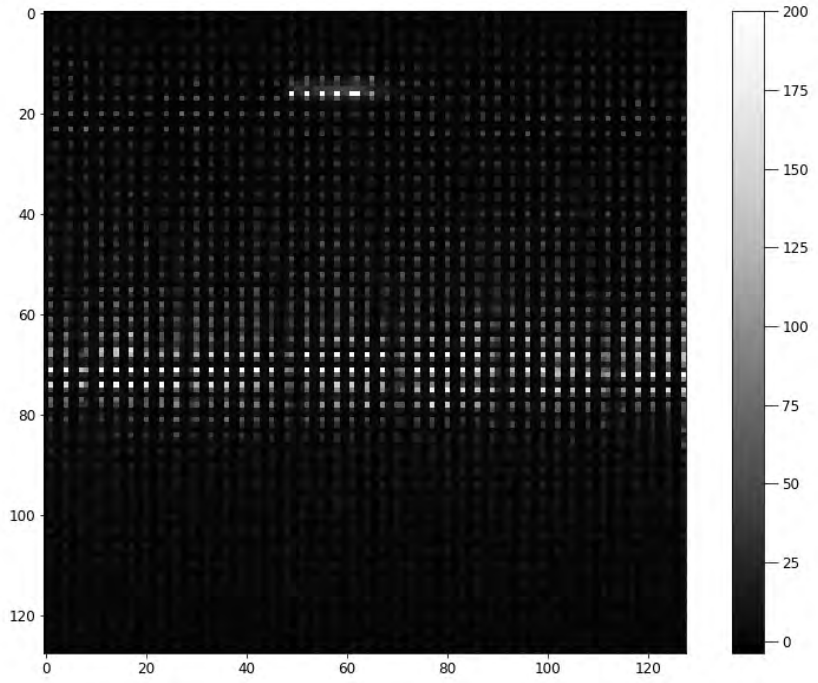

Figure 4.6: Response of Si-f50 to Ag monochromatic illumination incident to a pinhole mask with 25 μm holes on a 440 μm grid. The image is an average of 100 frames with a 300 ms collection time each. The rows with a brighter average intensity near the center of the sensor are illuminated with Ag kα radiation, and sufficiently isolated pixels in these rows are considered for computing the gain. The brightly illuminated pixels near the top of the image were not considered in the analysis, and are likely are results of an excess fluorescence in the X-ray tube.

integer value. Then, if a sufficiently large number of frames are taken, we can tabulate the total number of occurrences of a given ADU value in the set of intensities for isolated pixels for all frames with reasonable statistics. Since the photon energy is the same for all isolated pixels, we expect clear peaks in the histogram that correspond to 0,1,2,... incident kα photons. Figure 4.7 shows this histogram for 20,000 frames with a 1 ms collection time.

We fitted a Gaussian to the ADU peaks corresponding to 0,1,2, and 3 incident photons. Since the photon energy is known, we could determine the energy, in keV, associated with each peak. Then, we computed the ADU/keV gain factor via a linear regression of the ADU intensity vs total energy for the four peaks. This

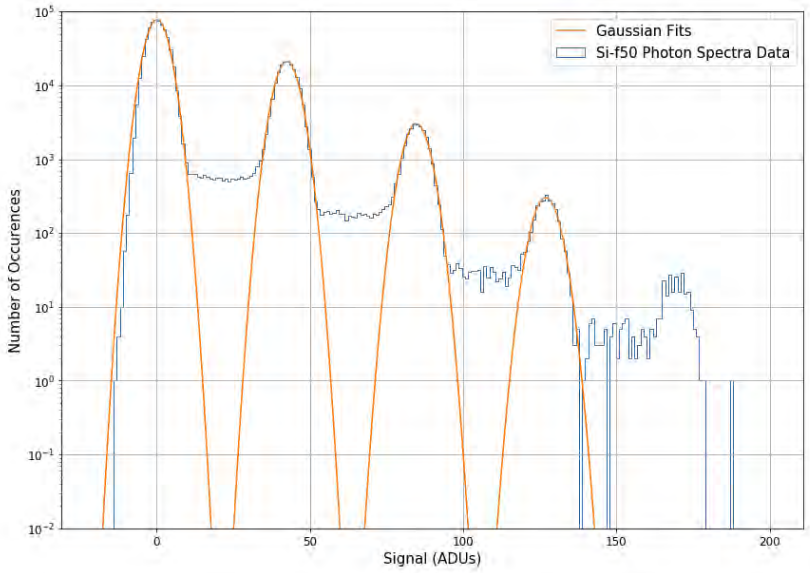

Figure 4.7: Intensity spectra for isolated pixels in the Ag kα band. Data is extracted from 20,000 frames, each with a 1 ms collection time. Each peak fitted with a Gaussian corresponds with intensities from an integer number of photons, starting with 0 photons centered around 0 ADU and increasing by one photon for each subsequent peak. We did not fit the peak corresponding to 4 incident photons due to low statistics.

gave a silicon gain value of **1.91 ADU/keV**.

This indicates that a discrete increase of 1 ADU, which defines the single-pixel energy resolution of the detector, corresponds with an energy increase of $\sim$0.5 keV. This indicates high sensitivity, particularly for the energies at which we typically image. The widths of the fitted Gaussians give the noise associated with each photon peak in ADU. The average noise from each peak was 3.30 ADU (equivalent to 0.078 Ag kα photons), which was slightly larger than the readout noise of 3.03 ADU (0.071 Ag kα photons). Overall, the single-pixel uncertainty was small, indicating strong detector performance.

4.4.2 Flood Illumination Response

Flood illumination measurements allow us to assess the uniformity in detector response across the face of the sensor. Variations in registered pixel intensities suggest a lack of uniformity in response to the same source, implying that the physical properties of the sensor may vary with pixel location. This could be rooted in fabrication, ASIC readout, or a wide variety of factors. It also provides a means to characterize the in-lab X-ray setup and inform us if various region of the sensor may be illuminated with different intensities, even if the pixels themselves behave similarly.

Figure 4.8b shows the sensor response to 47 keV X-rays from the silver tube. We specified a long (300 ms) collection time accentuate any nonuniformities. Note that regions of high and low intensity are defined by clear geometric patterns. We attribute this to the layers of tape that have been placed over the detector window to keep it intact, as shown in Figure 4.8a. These layers of tape attenuate the beam, and the amount of attenuation varies with how many layers of tape are directly in front of a given pixel.

From Figure 4.8b, it is also clear that edges of the sensor are more strongly illuminated than the center of the chip. We attribute this to the geometric discontinuity at the sensor boundary, which causes the electric field near the edges of the sensor to bend outwards at the edges. This is similar to the fringe effects in a parallel-plate capacitor, in which the geometry of the plates near its edges prevent the approximation that each plate is an infinite plane of charge. Thus, since the electric field from the bias voltage diverts toward the edges of the semiconductor, these edge pixels collect more photogenerated charge, and the intensity that is read out is noticeably greater, especially for longer integration times.

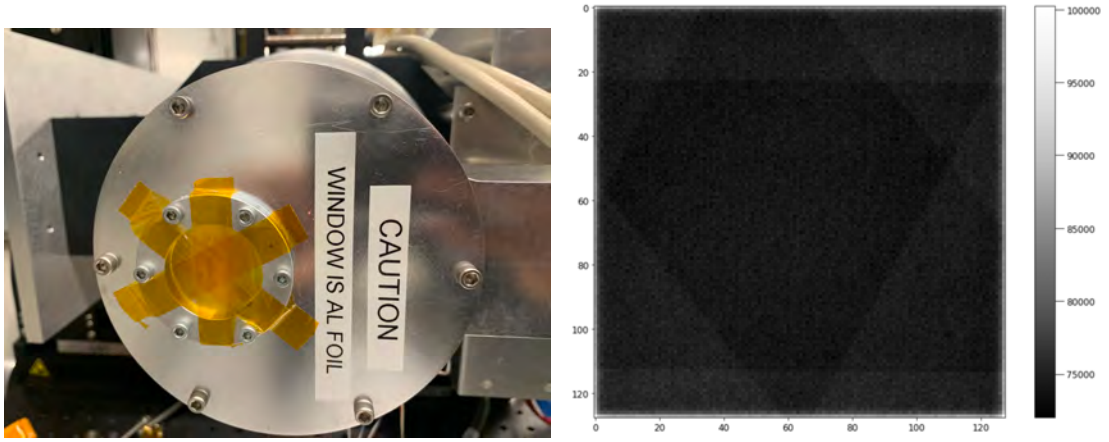

(a) (b)

Figure 4.8: (a) shows the tape placed across the detector window (b) is an average of 50 frames with the Ag tube biased at 47 kV and a specified 300 ms integration time.

Figure 4.9 is a histogram of the pixel intensities from Figure 4.8b. The peaks near 75,600 and 86,000 ADU correspond with the increased intensities near the edges. To determine the pixel-by-pixel variations in intensity for the interior pixels, we computed the standard deviation of the main peak in the histogram, which we found was 686 ADU.

More importantly, we determined to good approximation the uncertainty associated with photon counting (the shot noise), variations in the source (or tape in our case), and variations in the pixel-by-pixel response. Note that since that emitted photons have a wide range of energies, it is difficult to do better than a rough approximation in which we assume all photons have the same energy. We computed an order of magnitude estimation of the shot noise via the following procedure:

1. Determine the average ADU intensity of an interior pixel from the flood illumination histogram.

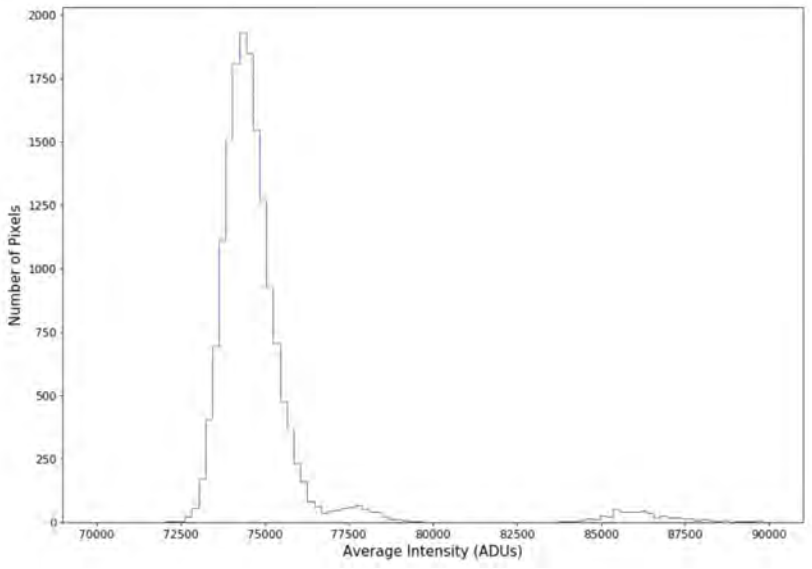

Figure 4.9: Histogram of pixel intensities from uniform flood illumination (Figure 4.8b). The secondary peaks in the histogram are due to an increase in current through the edges of the sensor. We focused on the main peak, centered at approximately 73,000 ADU, for our analysis of the variations in pixel-by-pixel response.

2. Assume an average photon energy of 22.1 keV (the Ag kα line). Use the pixel gain to determine average number of incident photons for the computed average ADU intensity.

3. The uncertainty in photon count is given by $\frac{\sqrt{\text{average photon count}}}{\text{number of frames}}$.

4. Convert uncertainty in photon count to equivalent number of ADU, again assuming uniform Ag kα radiation. This roughly gives the shot noise uncertainty.

We calculated the shot noise to be $\sim$30 ADU. This is far smaller than the total variation in interior pixel intensities. Therefore, the "width" of the peak could be attributed to either the variations in the source, likely due to the tape, or pixel-by-pixel variations that are exacerbated by the long collection time. To do this, we (roughly) isolated the region with darker interior pixels. The standard deviation of the histogram of this subset of pixel intensities was approximately 472 ADU.

Since nearly all of the pixels in this set were equally affected by the additional layers of tape, the 472 ADU uncertainty can be attributed to variations in pixel-to-pixel response. The remaining contribution to the total noise, given by (total noise) - (shot noise) - (pixel variations), represents the uncertainty due to the source/apparatus. This is about 180 ADU. Thus, the pixel-by-pixel variations are likely the driving source of uncertainty for flood illumination. However, the sensor is still highly uniform, as the total uncertainty ($\sim$686 ADU) is still small compared to the average pixel intensities ($\sim$70,000 ADU) for these imaging conditions.

4.4.3 Spatial Resolution

The spatial resolution of a detector is defined as the smallest separation between two independent point-like objects such that the two objects can be resolved. For pixelated sensors, we expect this separation distance to be of the order of the pixel size, assuming sufficient detector sensitivity resulting from a high charge-collection efficiency. However, we can more precisely quantify the spatial resolution by determining the width of the charge cloud generated by incident radiation. If we assume perfect detector performance with 100% charge collection efficiency, any incident X-ray photons will generate a certain number of charge carriers, all of which would travel in the same straight line in the direction of the applied electric field to the readout chip. In this model, the semiconductor behaves like an array of ideal, non-interacting, one-dimensional photodiodes. If this was the case, if we blocked half of a given pixel, we would expect the ADU pixel intensity to exactly halve. However, since the semiconductor is not ideal and there exists lateral charge spreading between pixels, this is not the case in experiment. We can quantify the spatial resolution by determining how much the registered intensity

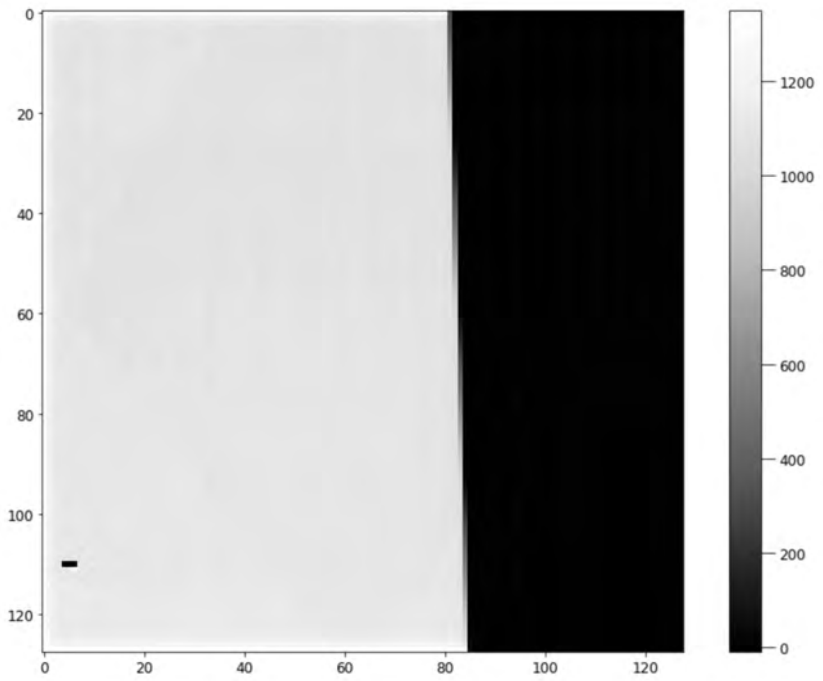

Figure 4.10: Image of a tantalum knife edge tilted at 1.67 degrees, taken from the average of 4000 frames with a 10 ms collection time. We used flood illumination from the Ag tube biased at 47 kV. Image was taken at 0^oC.

in a pixel decreases when a known fraction of the area is not exposed to X-rays.

We used a tantulum knife edge, tilted at a small angle, to partially illuminate a set of pixels and determine the corresponding sensor response. This allows us to compute the edge spread response (ESR), in which we compared the pixel intensity with and without the edge placed directly in front of a set of pixels. Figure 4.10 shows the image of the knife edge. We conducted measurements of the spatial resolution of the Si-f50 sensor at T = 0^oC, as the dark current was sufficiently small so as to not impede our analysis.

We took two sets of frames and constructed an average image for each. Let's call these two average images image 1 and image 2. The detector is shifted upward by 2 millimeters for the second set of frames, leading to the image of the edge

being shifted to the right relative to Figure 4.10. Then, pixel by pixel, we can divide image 1 by image 2 to create a map of the intensity ratios. Pixels near the edge in image 1 will be fully illuminated in image 2, so the values of the ratio map at these pixels will correspond to a fractional intensity.

The following procedure is used to produce the ESR from the intensity ratio image (slight modifications may be necessary when the knife edge is horizontal in the images).

1. For the set of relevant columns in the ratio image, plot the fractional intensity vs row number. Figure 4.11a is an example
2. Choose the columns that include pixels with fractional intensities ranging from 0 to 1 - this is the set of pixels that exhibited the full range of responses.
3. For each selected column, fit a line on the "ramp" part of each curve. Then, for each column, determine the row value for which the fractional intensity is 0.5 from its regression line. For adjacent columns, determine the difference in the corresponding row values. The average of the difference gives an average row spacing (ARS) between the locations of half intensity for adjacent columns.
4. Choose a central calibration column (Column 83 for Figure 4.11a). For each of the originally selected columns, reassign the row value of each of its points using the formula

   new row # = (old row #) + (calibration column # - column #)*(ARS)

   The data from each column should now overlap, as in Figure 4.11b.
5. Subtract all row values by the location of half intensity for the calibration row. Now, the intensity at the calibration "0" row should be 1/2. To con-

vert the x-axis to units of distance in pixels, divide the row number by the computed ARS.

6. At any point in this procedure, reflect the points about the (pixel distance = 0) line to be consistent with convention in previous studies.

If a sensor has perfect resolution (no charge spreading) and the source, knife edge, and detector are perfectly aligned, the edge spread function would be a ramp - the fractional intensity would exactly equal the proportion of the pixel area covered, which is given by the distance from the edge to the center of the pixel. We quantify how "imperfect" the ESR is by fitting it to a ramp function convoluted with a Gaussian. The Gaussian "smooths" the ramp, particularly near the transition points at the distances of -1 and 1 pixels from the edge. The width of the Gaussian determines how much smoothing occurs at these transition points. For our analysis of the Si-f50 spatial resolution, we fit by eye. Figure 4.12 shows the ESRs and corresponding best fits for the Ag 47 keV source and a Cu 23 keV source.

We found that the spatial resolution was about 22.5 μm for the Ag 47 keV source and about 15.0 μm for the 23 keV copper source. Both of these values are small, indicating the charge spreading in the bulk semiconductor is largely minimized. However, an interesting feature for the Ag source is the asymmetry of the ESR at pixel distances of -1 and 1. The "roll-off" below a fractional intensity of 1 suggests that the pixels near the edge that are almost completely uncovered are still registering a noticeably lesser intensity than when the edge is not present at all. However, this effect is not observed for the lower energy emissions from the Cu tube. We believe this may be the result of an extraneous fluorescence occurring at a particular location in the X-ray beampipe that is only produced

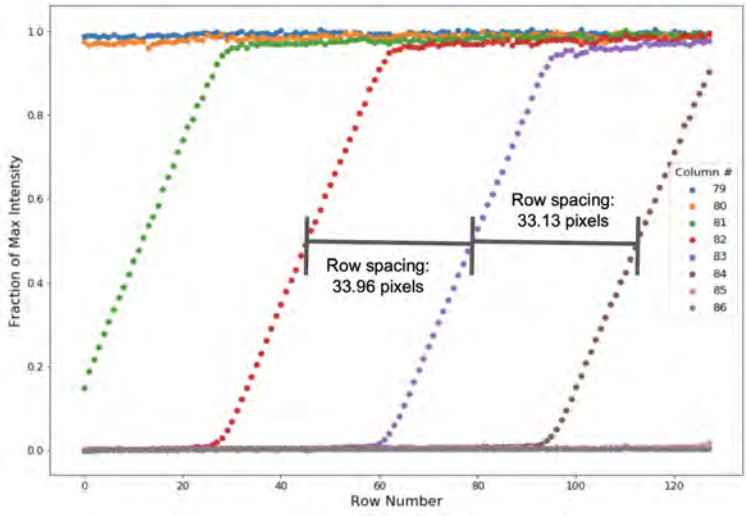

(a)

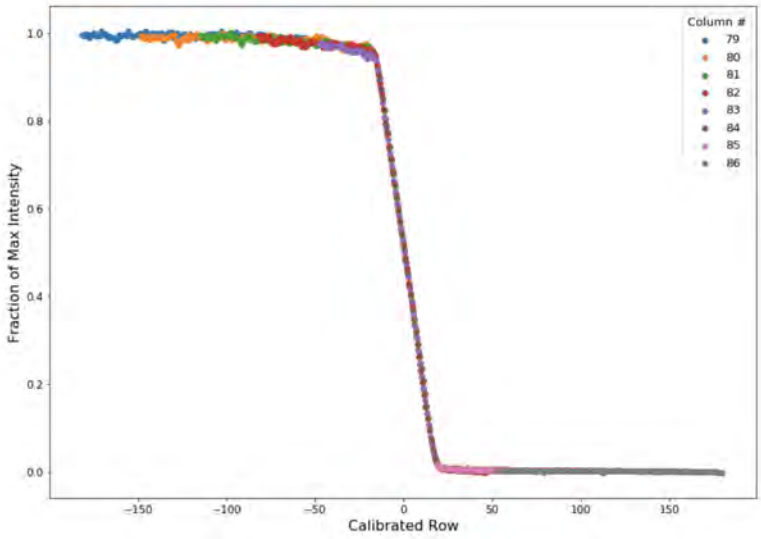

(b)

Figure 4.11: Steps in the procedure for determining the ESR from intensity ratio images. Data was taken using 47 keV flood illumination with an Ag tube and a 10 ms collection time. (a) shows the fractional intensities by row and illustrates the average row spacing, though the regression lines are not shown. (b) shows how the data is aligned after computing a new "calibrated" row for each data point.

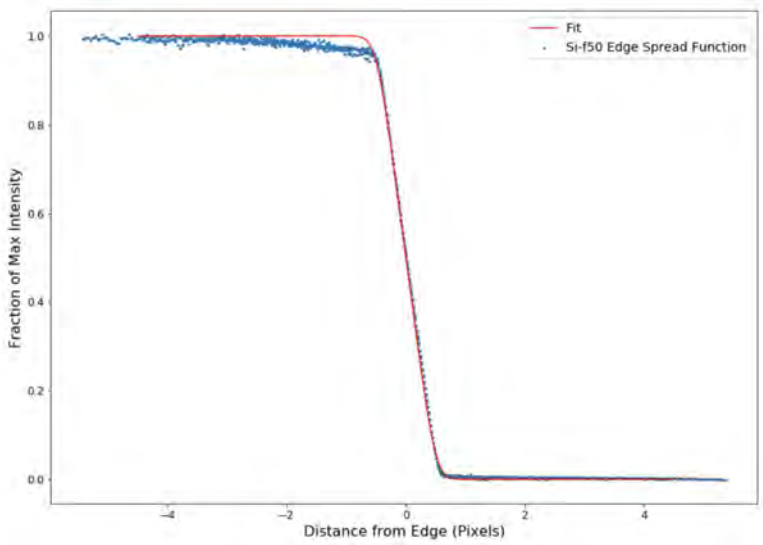

(a)

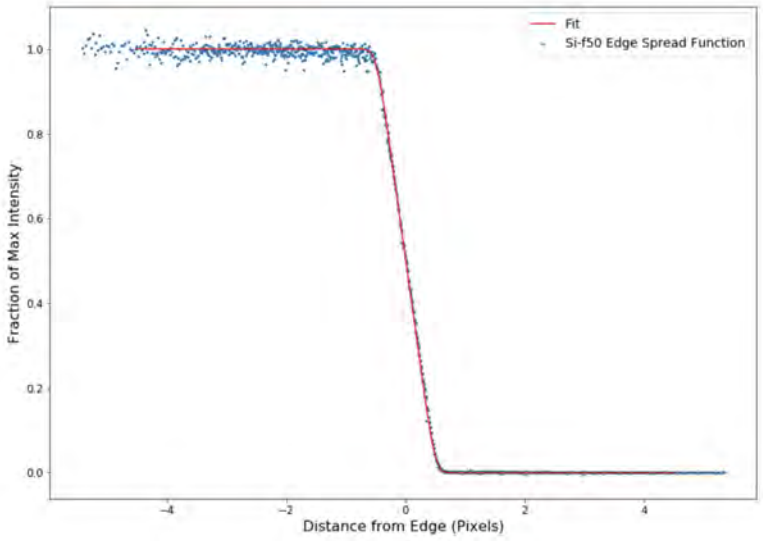

(b)

Figure 4.12: Edge spread functions for Ag 47 keV and Cu 23 keV flood illumination from 4000 averaged frames with a 10 ms collection time each. The Gaussian kernel had a width of 22.5 μm for the silver source and 15.0 μm for the copper source.

at higher energies. Since the location the fluorescence occurs is not known, the fluorescent photons may only reach certain pixels. The alignment of the location of the fluorescence, knife edge, and detector is different from that of the primary source, knife edge, and detector, so the fluorescent photons may be blocked from reaching these pixels by the knife edge, even if the knife edge is not directly in front of them. This is consistent with our observation that the roll-off switches to the other side of the ESR if the orientation of the edge if changed. If roll-off is ignored, the spatial resolution of the Si-f50 is high, as the charge spread in the sensor is small relative to the pixel size.

CHAPTER 5

CHARACTERIZATION OF SENSOR BEHAVIOR FOR DOPED GERMANIUM OF VARYING THICKNESSES

5.1 Properties of Germanium Semiconductors, Production, and Operating Conditions

Doped germanium semiconductors remain an appealing alternative to silicon for use in X-ray detection, particularly due to its increased quantum efficiency for hard X-rays as described in Section 2.1. Moreover, (relatively) high purity germanium wafers are commercially available and relatively inexpensive [36].

Doped germanium has an indirect band gap of 0.7 eV. However, prior studies have shown that the activation energy, $\sim$0.21 eV, is less than the band gap [36]. This can be attributed to a high defect concentration relative to silicon, which enables a predominance of SRH dark current generation [36]. For optimal performance, the sensor should be kept at the lowest possible temperature to minimize excitations out of the band gap defect states. Previous studies have found imaging possible at approximately -80^{o}C or lower, though we had difficulty reconstructing meaningful images at temperatures greater than -140^{o}C [36].

The Gruner lab characterized a set of six hole-collecting germanium sensors with thicknesses of 34 μm, 54 μm, 55 μm, 98 μm, 150 μm, and 200 μm that were bump-bonded to MMPAD ASICs at MIT's Lincoln Laboratories. Recall that the semiconducting materials used to produce photodiode detectors must have a sufficiently high resistivity at the imaging temperature to enable full depletion without an excess of leakage current. Leakage current increases sensor noise and

can heat and damage the sensor if it is sufficiently large. The germanium wafers we studied were produced commercially and can be used for applications outside of radiation detection, such as the fabrication of germanium MOS. These applications do not require the same level of resistivity as a photodetector, and more generally, high resistivity germanium is difficult to find. During testing, we observed excess and nonuniform amounts of leakage current before full depletion, particularly for the thicker sensors, likely due to a low and nonunifrom resistivity. We present a more thorough analysis of the depletion behavior in the following section.

Exposing germanium photodiodes to high temperatures ($\sim$100^{o}C) can lead to an increase in diode leakage current and to the deformation of the detector bump-bonds. Bump bond damage is due to the difference in the thermal conductivity of the germanium sensor and the silicon readout chip [36]. As a result, the traditional method of high-temperature solder bump-bonding the sensor to the ASIC can be problematic. At MIT-LL, the germanium wafers were *indium* bump-bonded to the MMPAD. Indium is remarkably ductile at lower temperatures and can absorb the mechanical stresses induced by the mismatch in thermal properties [37]. Bump-bond size and uniformity are studied extensively in [37], but the electrodeposition of indium bump-bonds is a mature technique that is not expected to inhibit detector operation, particularly for the MMPAD's 150μm-by-150μm pixels.

I was involved with testing the hole-collecting 54 μm, 55 μm, 98 μm, 150 μm, and 200 μm sensors. The group characterized the 34 μm sensor before I joined, so I will not include detailed results regarding its behavior. However, it was capable of imaging at cryogenic temperatures before it cracked, likely due to prolonged exposure to cryogenic temperatures. The 54 μm sensor also imaged until it too cracked after being left at cryogenic temperatures overnight. The

remaining sensors did not fully deplete so imaging was not possible. The 55 μm sensor was photosensitive and exhibited unstable depletion and leakage current behavior, while the remaining three thickest sensors were not particularly close to sufficient depletion for imaging. I include a brief summary of our study on just the 54, 55, and 98 μm sensors, as the 150 and 200 μm sensors exhibited behavior almost identical to that of the 98 μm.

5.2 54μm Sensor Characterization

We tested and characterized the 54 μm sensor before we had programmed the cryostat's temperature controller. We cooled the sensor by completely filling the liquid nitrogen chamber all at once, leading to a temperature decrease from $\sim$20^{o}C to $\sim$ -170^{o}C over several minutes. Again, the sensor cracked within 24 hours of cooling, so not all relevant data was collected. Moreover, the range of analog current values and the analog-to-digital multiplier were not verified before the sensor cracked, so the included data and figures are analyzed from a somewhat qualitative standpoint.

5.2.1 Depletion Behavior

Doped silicon with a 200 μm thickness is known to deplete near 100 V and image best at 150-200 V, so we did not investigate the depletion of the sensor in Chapter 4. A high detector leakage current, coupled with a large applied bias voltage, would transfer heat (at a rate given by P = IV) to its surroundings and boil away the liquid nitrogen at a high rate. We did not know if the germanium

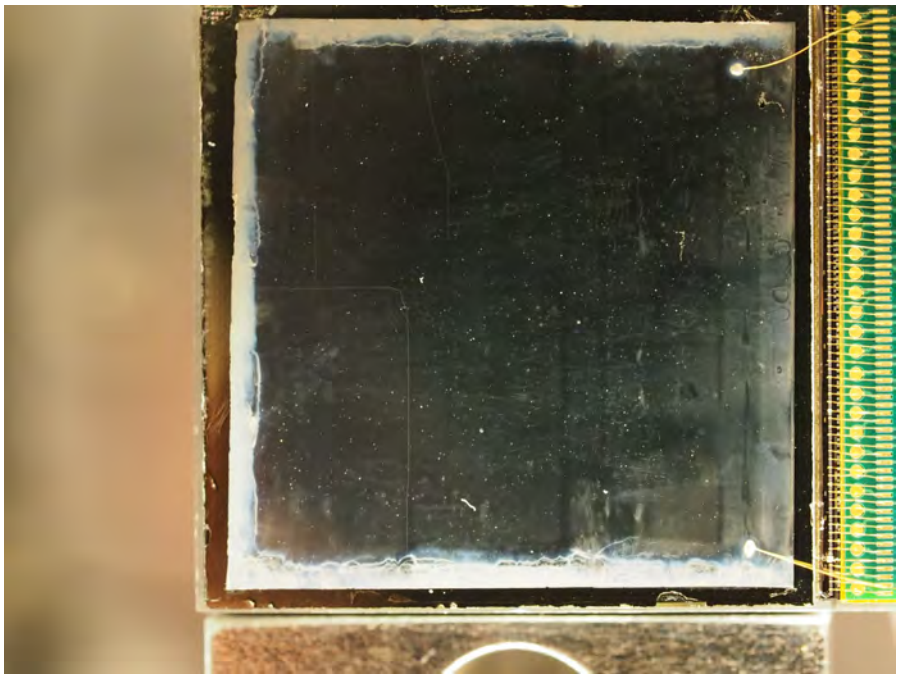

Figure 5.1: Photograph of the 54 μm sensor after cracking. Two cracks (which together make a rectangle with the perimeter of the sensor) are visible near the bottom left of the image.

sensors would deplete before the leakage current would be large enough to heat the environment. We slowly increased the applied voltage bias to observe the bias current and ensure that this state was not reached.

Figure 5.2 shows background images for a range of applied bias voltages. Images were taken at -170^{o}C. The black pixels correspond to an excess of current traveling from the ASIC to the germanium semiconductor. These pixels register an ADU value of 0, as the MMPAD does not register negative intensities if the image is not background-subtracted. Each integrating amplifier in the readout pixels has a nonzero reference voltage that determines the rate of integration. The effective bias voltage applied to a given photodiode is the difference between the voltage supplied by the Keithley power supply and this reference voltage. As a result, at low biases, the semiconductor may still be forward-biased, which leads to an excess

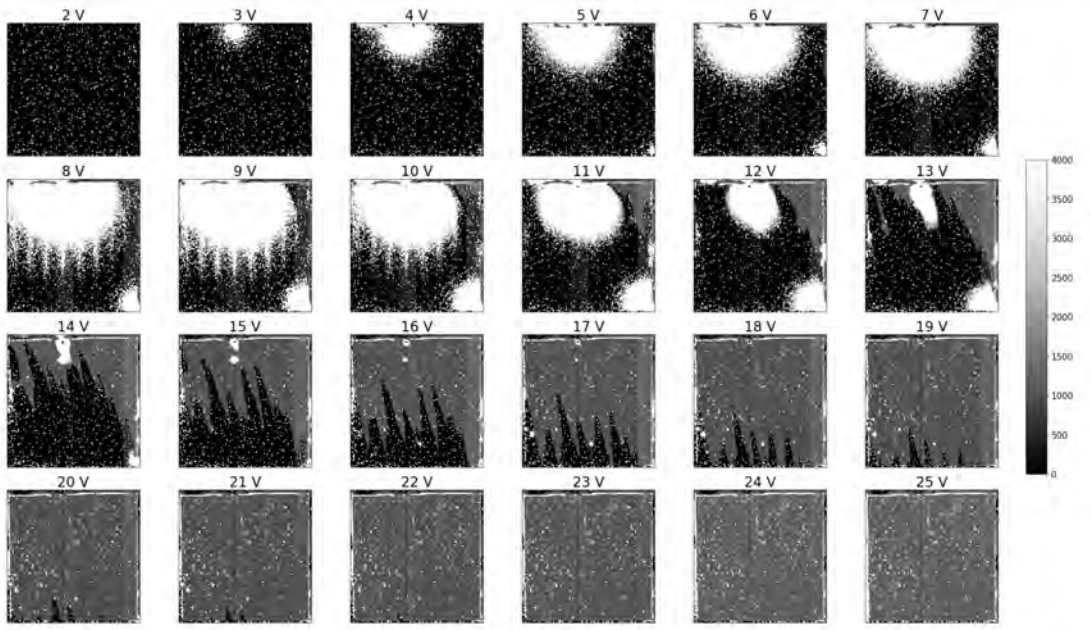

Figure 5.2: Depletion behavior of 54 μm germanium for varying biases at -171^{o}C. Each subplot is an average of 100 frames with a 1 ms collection time each. The black regions consist of pixels with excess hole current flowing from the ASIC into the sensor. The white regions correspond with a high hole current passing from the sensor into the ASIC. The light grey regions have a small hole current passing from the sensor into the ASIC and represent photosensitive regions of depletion.

of current opposite the direction the input bias is supplied.

The bright white regions correspond to areas of complete saturation where the hole current traveling from the semiconductor to the ASIC is extremely high. This behavior usually suggests a reverse breakdown due to a large reverse bias, so the proximity of the saturated regions to the described dark regions at intermediate biases is puzzling. This suggests a strong lack in uniformity in the physical properties of the bulk semiconductor, requiring us to refrain from treating each pixel as an independent photodiode. We attribute this behavior to a type of charge cycling process in the semiconductor bulk, in which the large hole current that travels from the ASIC into the sensor is diverted to neighboring regions in the semiconductor via a lateral electric field perpendicular to the direction of the bias. The electric

field in this neighboring region points in the direction of the bias, and the extremely large hole charge drifts to the pixelated region and is integrated accordingly. The lateral electric fields that enable this type of charge cycling require localized and pronounced variations in the solid-state properties of the semiconductor. A probable explanation is that the wafer has an especially low and nonuniform resistivity, which will introduce high quantities of leakage current that can then cycle through the sensor if there exist defects that can change the electric field in the sensor bulk.

At around a 14 V bias, the saturation regions begins to dissipate and localized regions of a small hole current (the light gray patches) begin to form. These light gray patches correspond to depleted regions in the germanium bulk. We approach full depletion near 21 V, though there still exist isolated pixels with a high leakage current. It is possible that adjusting the amplifier reference voltages would have allowed these "flaky" pixels to deplete normally, but we did not get the opportunity to investigate this before the sensor cracked.

We were also interested in the relationship between the hole current passing through the pixelated region of the detector and the total bias current supplied by the Keithley power supply, as shown in Figure 5.3. The current through the pixels peaks near 8-10 volts, corresponding to the biases which maximized the number of saturated pixels. Note that we registered an ADU intensity of 0 (instead of some large negative value) in the pixels in which there was an excess current flowing from the ASIC into the sensor. This may inflate the computed pixel current for the smaller biases voltages.

Figure 5.3 shows that although the supplied input current increases monotonically with bias voltage, once the sensor is depleted, minimal current passes through the pixelated region of the sensor. This suggests that there exists some path with

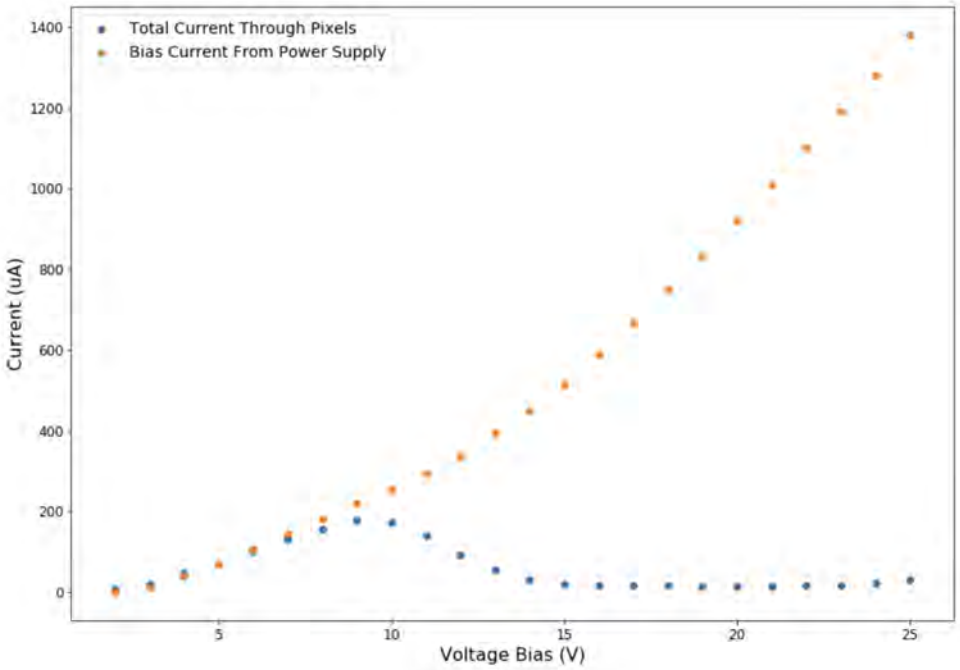

Figure 5.3: Change with bias voltage of the measured current through detector pixels (computed from Figure 5.2) and the input bias current.

minimal resistance outside of the pixels that the bias current can pass through. We speculated that the increased leakage current was passing through the guard rings of the pixels, as previous studies have shown an increase in guard ring current with voltage bias [36]. The guard ring is a set of PAD implants around the edges of the sensor that can collect current but do not process a signal. Therefore, we expect that at higher biases, there exists a high leakage surface current that moves along the edges of the sensor and is collected by guard ring electrodes. For sensor operation, it is most important to minimize the leakage current reaching the readout pixels, though the current "excluded" from the pixels can still lead to sensor heating. Therefore, we would ideally hope to eliminate excess leakage current in the semiconductor, although we would expect little effect on the quality of data collected.

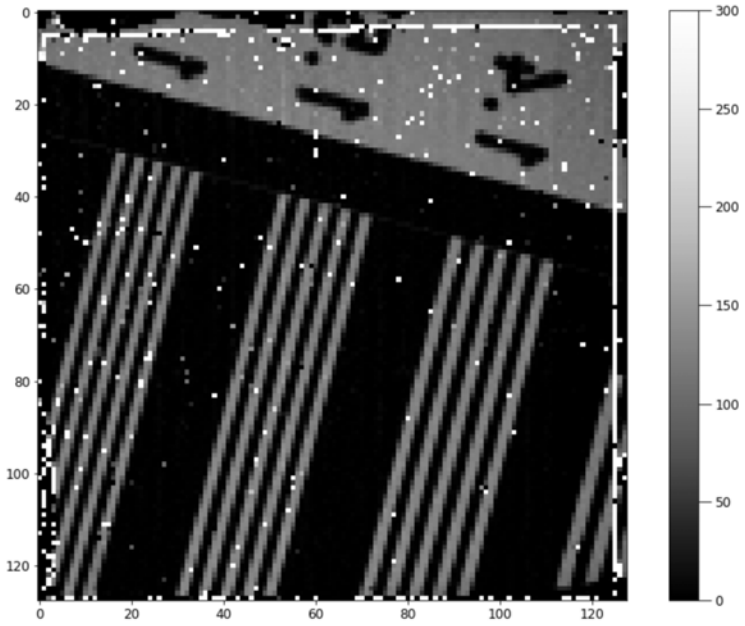

Figure 5.4: Image of a line pair mask from the Ag X-ray tube biased at 35 kV. The sensor was biased at 25 V, and 100 frames with a 1 ms collection time were averaged.

5.2.2 Qualitative Imaging Performance

We imaged the line pair mask at -170^{o}C to show that this sensor was capable of producing coherent images. From Figure 5.4, it is clear that we were able reconstruct images with a resolution on the order of millimeters (the width of the lines in the mask) but that the abundance of bright pixels noticeable reduces the overall quality of the images. We did not get the opportunity to image to lightbulb or otherwise qualitatively assess the performance of this sensor before it cracked.

5.2.3 Spatial Resolution

We used the same procedure for determining the spatial resolution as we did for the Si-f50 sensor, for which we used an image of a tantalum knife edge to determine

the response of pixels partially illuminated by the incident X-rays. Please refer to Section 4.4.3 to see how the edge spread function is computed from an image of a knife edge. Figure 5.5 shows the averaged image of the tungsten knife edge and the resulting edge spread function. When we first plotted the edge spread behavior, we noticed a high degree of nonlinearity in the sensor response. We attributed to the fact that the analog-to-digital multiplier value had not been computed before the detector cracked. We determined a multiplier value via data post-processing and recomputed all ADU intensities with the new multiplier to create a new set of knife edge images. From the modified average image, we computed the resulting edge spread function, for which the nonlinearity improved noticeably. After this, we excluded the flaky bright/dark pixels from the edge spread function by filtering out pixels with a substantially higher or lower intensity than its immediate neighbors. We fitted the edge spread function by eye to a ramp function convoluted with a Gaussian. Again, the width of the Gaussian gives the lateral spread of the photogenerated charge cloud in the bulk of the semiconductor, which is how we define the spatial resolution of a Hybrid Pixel Detector.

The measured spatial resolution of 15 μm indicates strong detector performance. Like the Si-f50 sensor, there exists noticeable roll-off in the edge spread data about a pixel away from the edge. We again can potentially attribute this to an excess fluorescence in somewhere in beam pipe that is aligned differently with the knife edge and detector.

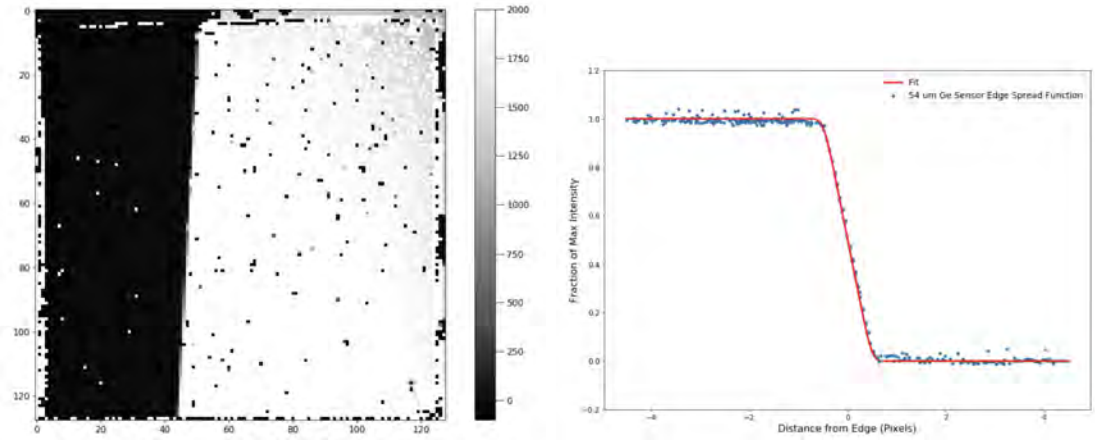

(a) (b)

Figure 5.5: (a) is the average of 4000 1 ms frames of the tantalum knife edge, taken with flood illumination from the Ag tube biased at 35 kV. The sensor was biased at 25 V and images were taken at -170^{o}C. After a post-processing procedure and the exclusion of flaky pixels, the ADU intensities from (a) and an additional image with the pixels fully illuminated were used to create (b), the corresponding ESR fitted with a ramp function that has been convoluted with a Gaussian. The Gaussian width was 15 μm, which represents the spatial resolution of the detector.

5.3 55μm Sensor Characterization

Despite having an almost identical thickness to the 54 μm sensor, the 55 μm sensor did not fully deplete before the total power drawn by the sensor heated its surroundings and the temperature in the cryostat increased quickly. We programmed the temperature controller before testing the sensor, so we were able to cool the detector incrementally and warm it back to room temperature over several hours. The sensor did not crack, though its utility was limited since it did not fully deplete. Figure 5.6 shows the thermal history of the sensor during the cooling process and the resulting input current for a fixed bias, which again is strongly correlated with the dark current.

The 55 μm sensor depleted in localized regions that were sensitive to incident radiation. However, the leakage current through the pixels would increase with

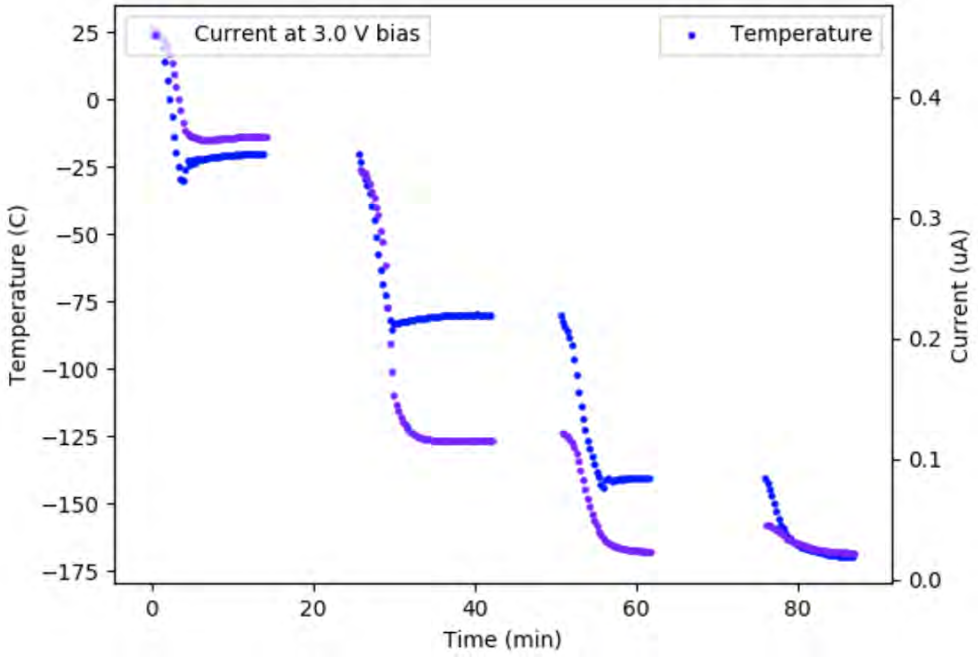

Figure 5.6: Thermal history and input current at a 3 V bias during the cryogenic cooling of the 55 μm sensor.

time, affecting the depletion behavior. These results are summarized in the next section.

5.3.1 Depletion Behavior and Leakage Current Instability

Figure 5.7 shows the depletion behavior of the sensor for various biases at -171^{o}C. Like the 54 μm sensor, at lower biases there is a high concentration of pixels with 0 ADU intensity, corresponding to a high hole current flowing from the ASIC into the bulk of the sensor. At intermediate biases, regions of saturation develop, and the first localized depletion patch appears around 20 V. At higher biases, most of the saturation regions deplete, but even at 32 V, the maximum bias we could apply without drawing too much current, there still existed regions that did not deplete. The images in Figure 5.7 were taken immediately after the

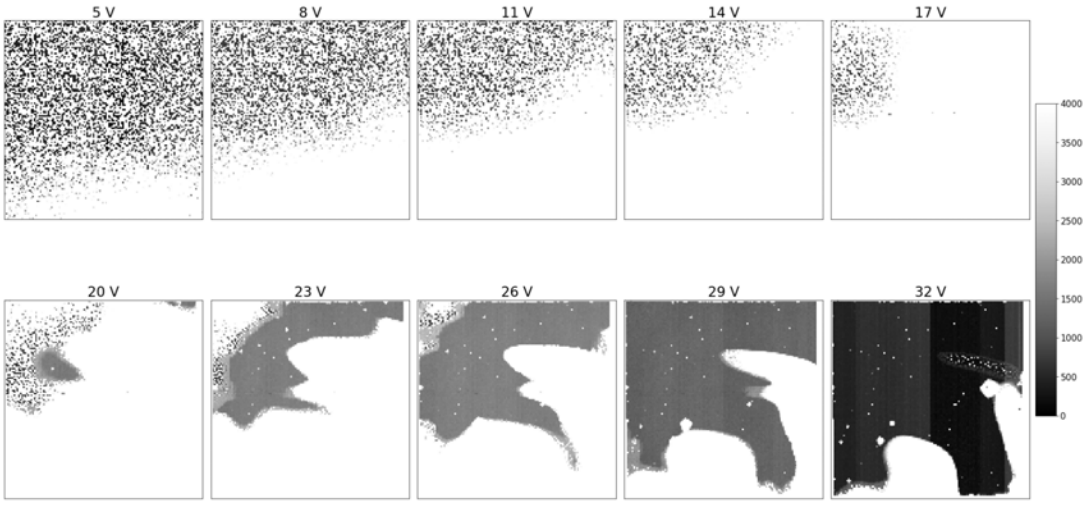

Figure 5.7: Depletion behavior of 55 μm germanium for varying biases at -171^{o}C. Each subplot is an average of 100 frames, each with a 10 ms collection time. The black/white speckled regions consist of pixels with excess hole current flowing from the ASIC into the sensor. The white regions correspond with a high hole current from the sensor into the ASIC. The light gray regions have a small hole current from the sensor into the ASIC and represent photosensitive regions of depletion.

specified bias was set.

Similar to the 54 μm sensor, depletion begins at a localized region before spreading throughout the sensor. The nonuniformity in depletion behavior suggests that the physical properties of the sensor, such as the resistivity or doping profile, vary across the face of the crystal. Again, the low resistivity of the germanium wafer likely contributed to the non-ideal depletion behavior.

Furthermore, the total leakage current through the sensor, given by the input current from the biasing power supply, increased quickly with time (Figure 5.8). This correlated with the shrinking of the fully depleted region. Though we do not know the exact cause of this phenomena, we hypothesized that there exists a high concentration of charge traps, in which charge carriers are captured by a defect in the band gap before being remitted to the conduction band via "detrapping" [7].

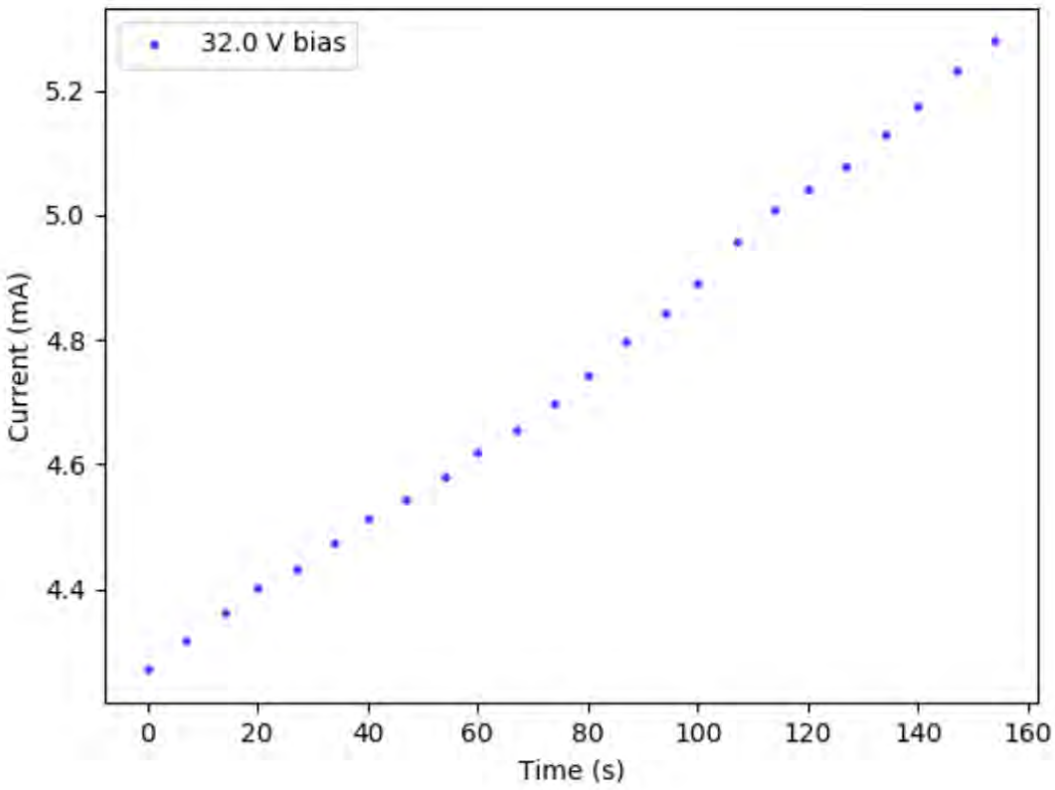

Figure 5.8: Input bias current versus time at a 32 V bias.

Charge trapping is discussed in more detail in Section 1.2.2. Initially, under the reverse bias, all free charge carriers have recombined with dopants or otherwise inhabit these trap states. We speculated that a prolonged exposure to a high bias can lead to detrapping, corresponding to an increase in leakage current as the number of available charge carriers in the bulk germanium increases with the bias exposure time [7].

In other words, the depletion region shrinks with time because holes are released from band-gap defects and are swept to the readout chip. The holes are eventually "pulled-out" of the traps after prolonged exposure to a high bias, but we would expect that decreasing the bias voltage would decrease the strength with which this "pulling" occurs. This would allow the traps state to refill and potentially provide

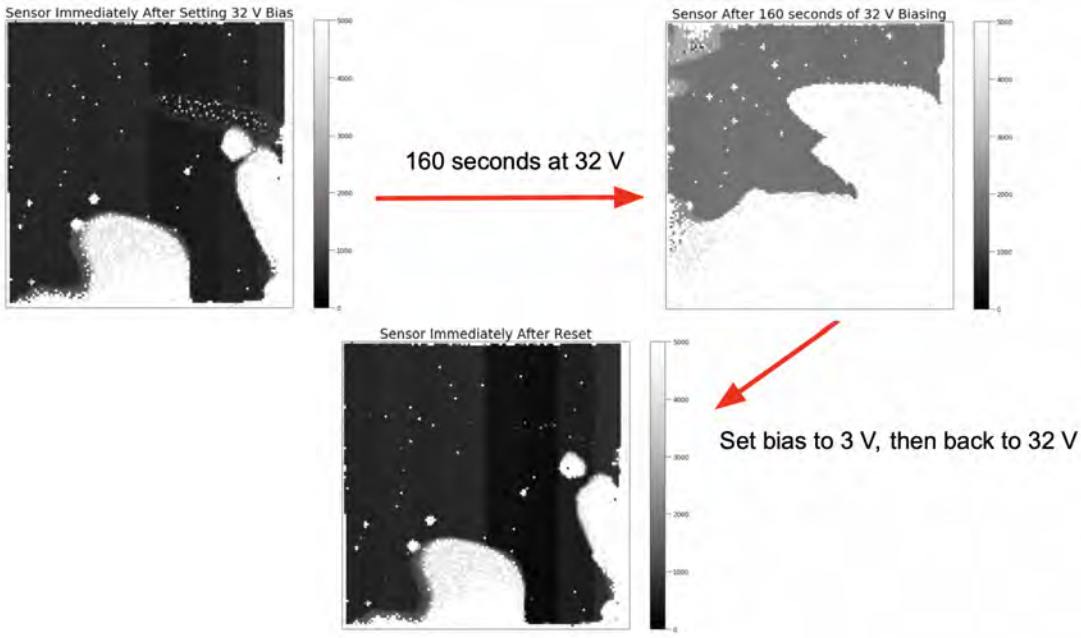

Figure 5.9: Depletion shrinking and resetting procedure for the 55 μm sensor. After a prolonged exposure to a 32 V bias, the localized regions of depletion shrink with an increase in hole current through nearly all of the originally depleted pixels. However, the sensor can be refilled with positive charge carriers by exposing the sensor to a low bias for several seconds. This restores the original depletion behavior.

the means the restore the initial depletion pattern. Once the semiconductor is no longer depleted (without use of this rather inconvenient restoration procedure), imaging is not possible, and the liquid nitrogen begins to boil away as the detector system heats up rapidly. This prevented a extensive characterization of even the depleted pixels at a 32 V bias. Figure 5.9 illustrates the shrinking of the depletion region and demonstrates how depletion can be reset by temporarily decreasing the bias voltage.

Lastly, we verified that the pixels that appeared depleted were indeed sensitive to incident X-ray radiation. Figure 5.10 shows the background at 32 V and a background-subtracted knife edge image. Although the intensities of the background-subtracted image are generally not reliable, as we have shown that

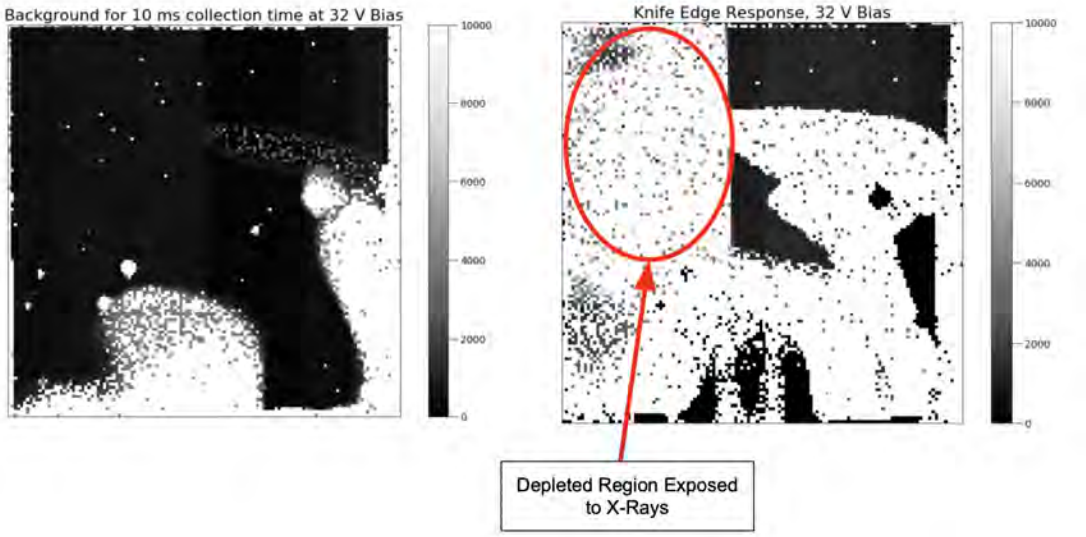

Figure 5.10: Background image for a 32 V bias and background subtracted knife edge image using X-rays from the Ag tube biased at 47 kV. Each images is an average of 10,000 frames with a 10 ms collection time. The increased intensity in the region unobscured by the knife edge demonstrates that the depleted pixels are indeed photosensitive.

the depleted pixel intensities are increasing with time, the large ADU signal in the region exposed to X-rays demonstrates that the depleted pixels are indeed photosensitive shortly after biasing.

The increase in intensities in the region not exposed to X-rays illustrates that the leakage current instability inhibits X-ray imaging. An investigation of the sensor fabrication, beginning from the growth of crystalline germanium, would be the next steps in better understanding this behavior.

5.4 98 μm Sensor Characterization

Here we present the behavior of the 98 μm sensor. We were only able to deplete a small region of the sensor before the excess sensor leakage current affected the

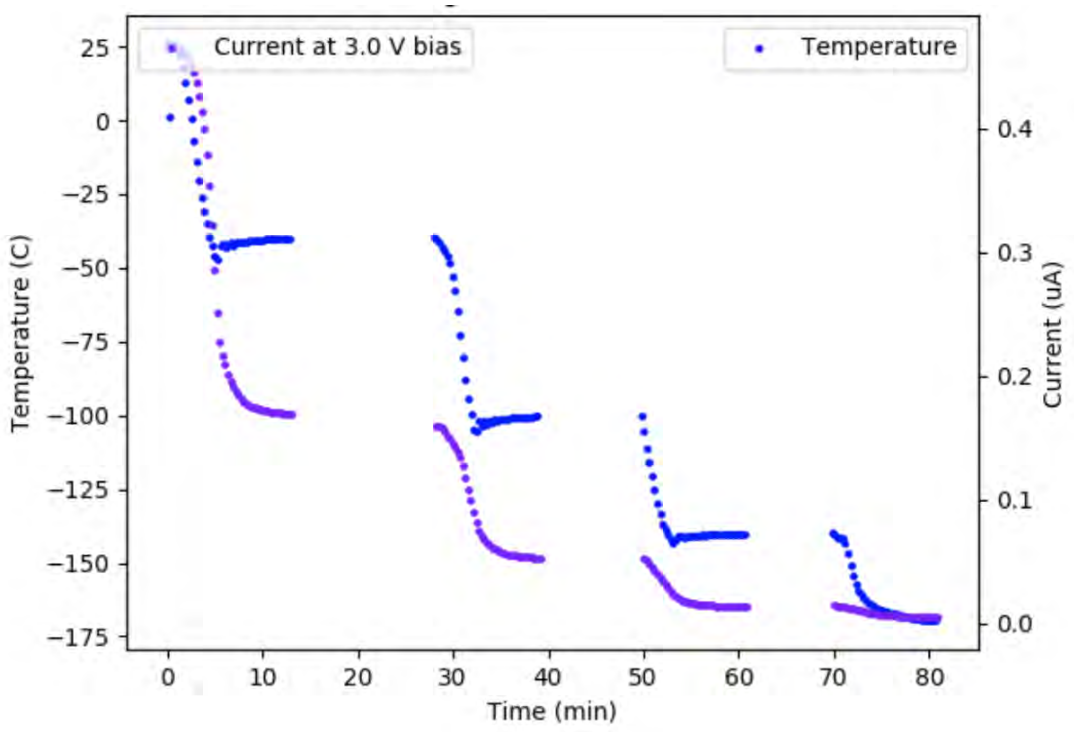

Figure 5.11: Thermal history and input current at a 3 V bias during the cryogenic cooling of the 98 μm sensor.

surrounding temperature of the system. Extremely similar behavior was observed in the thicker germanium sensors provided to us by MIT-LL - we only discuss this sensor to eliminate redundancy. Depletion is more difficult to achieve in thicker sensors since the electric field in the bulk semiconductor is inversely related to the thickness for a fixed bias. Therefore, given the behavior of the 55 μm sensor, we did not expect to be able to taken meaningful images for a 98 μm thick sensor.

Figure 5.11 shows the thermal history and the resulting changes in input current for a fixed bias voltage. Since the sensor was thicker and was cooled and warmed judiciously, it did not crack at any point during the characterization.

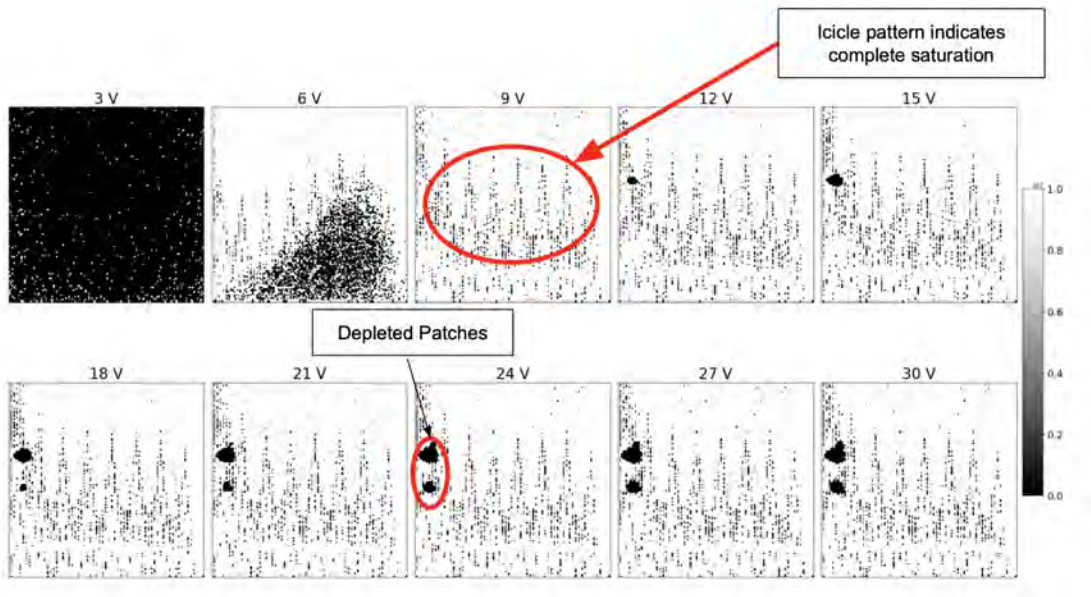

Figure 5.12: Depletion behavior of 98 μm germanium for varying biases at -171^{o}C. The colorbar scale is in units of ADU$\times 10^7$. Each subplot is an average of 100 frames, each with a 10 ms collection time. The black regions consist of pixels with excess hole current flowing from the ASIC into the sensor. The white regions correspond with a high hole current from the sensor into the ASIC. The small black patches have a small hole current from the sensor into the ASIC and represent regions of depletion.

5.4.1 Saturation at Low Bias Voltages

Figure 5.12 shows the depletion behavior of the sensor for various biases at -171^{o}C. The 98 μm sensor saturates at a lower bias than the 54 and 55 μm sensors. This is consistent with previous studies that have measured a higher leakage current in thicker semiconductors. However, since the photodiodes do not deplete before the leakage current is too high, the sensor remains almost completely saturated. Note that several localized and unconnected areas deplete at higher biases, but it remains unfeasible to conduct any X-ray-dependent characterizations.

Moreover, like the 55 μm sensor, the total leakage current at a set bias increased quickly with time as shown in Figure 5.13. Though the rate of change appears to

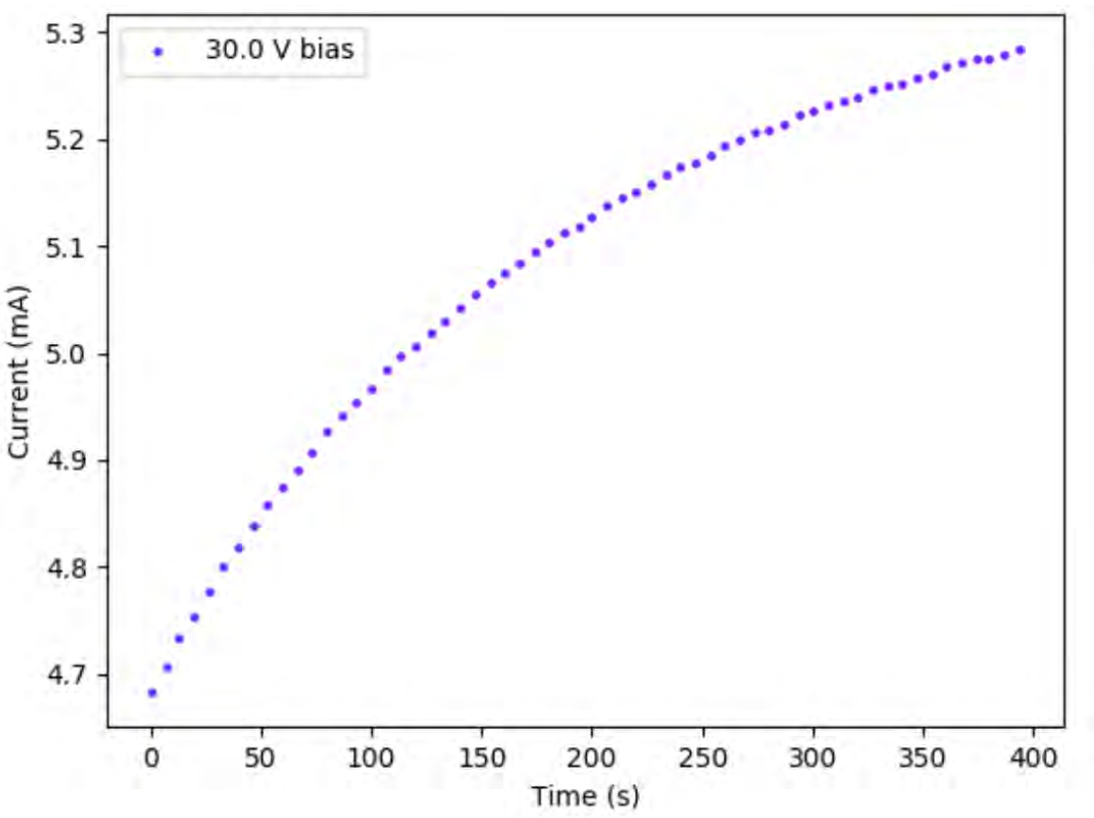

Figure 5.13: Input bias current versus time for the 98 μm sensor at a 30 V bias.

decrease as time passes, this instability potentially suggests a high defect concentration in the germanium, resulting in charge detrapping after prolonged exposures to high biases. Moreover, the decrease in the rate of change may suggest that the traps are beginning to empty-out after a sufficiently long exposure, though it is difficult to verify this with high confidence.

Together, our study of MIT-LL's sensors demonstrate that germanium is a promising high-Z material for use in a hybrid pixel X-ray detector, but the fabrication and production of high-resistivity germanium wafers is not straightforward. Leading researchers, including a group at Brookhaven National Laboratory, are working to fabricate thick, photosensitive germanium sensors with a high resistivity that the Gruner/Thom-Levy lab will hopefully characterize in the months

following my involvement in the project.

CHAPTER 6

SPATIAL RESOLUTION OF AMORPHOUS SELENIUM

6.1 Properties of Amorphous Selenium Semiconductors, Production, and Operating Conditions

The Gruner/Thom-Levy lab collaborated with researchers at Brookhaven National Laboratory, Stony Brook University, and other groups to investigate the performance of directly-deposited amorphous selenium on the MMPAD. Amorphous materials lack a well-defined crystal structure and are thus produced via markedly different procedures than the crystalline semiconductors we have investigated thus far. Amorphous selenium (a-Se) is most commonly used for medical imaging largely because it can be deposited uniformly over the large-scale flat panel imagers required to image objects the size of human body parts [31, 38]. We were interested if similar fabrication procedures could be used for synchrotron X-ray detectors, so the selenium was evaporated directly on the MMPAD for this investigation. Each readout pixel of a bare MMPAD ASIC has an aluminum pad upon which a solder or indium bump bond typically rests. We extended these aluminum pads to cover a far greater portion of each pixel's area and deposited 200 μm of amorphous selenium directly on this aluminum layer [14]. By departing from the typical bump-bonding procedure used for crystalline semiconductors, we had the potential to assess not only the performance of a-Se, but also if PAD readout is congruent with a new category of semiconducting materials.

a-Se is a compelling material due to its low dark current at room temperature, high photoconductivity, and high quantum efficiency for hard X-rays [14, 38]. How-

ever, low charge carrier mobilities and a high concentration of charge traps reduce detector sensitivity and lead to a slow signal response [14]. As a result, the a-Se sensor required a high bias voltage ($\sim$2 kV) and lacked the dynamic response exhibited in many crystalline sensors. Again, the direct-deposition of amorphous detector on CMOS readout is a relatively new practice, for which new techniques are being developed to ameliorate these drawbacks [14].

My involvement with the a-Se project was mostly limited to an investigation the spatial resolution for various X-ray spectra. A more thorough characterization that includes radiographs, charge collection at various biases, and the dynamic response is included in the group's recent publication: [14].

6.2 Measurement of Spatial Resolution

Here we present measurements of the spatial resolution of the 200 μm hole-collecting selenium sensor. The sensor was biased at 2 kV and imaged at room temperature and pressure. It was not necessary to compute the analog-to-digital multiplier because the exposure times/incoming intensities were too low for digital counts to be registered. The detector was placed in a single slot of the MMPAD 2×3 housing, as it was easiest to epoxy a high voltage wire using this setup. Figure 6.1 illustrates the test setup.

We investigated the spatial resolution for two different X-ray emission spectra: a 23 kV biased Cu tube with 25 μm Ni filter and a 47 kV biased Ag tube with a 1 mm Al filter. The 25 μm Ni filter absorbs nearly all of the Cu kβ radiation, resulting in a nearly monochromatic source. The 1 mm Al filter reduces much of the lower energy part of the spectrum without reducing the total photon count too

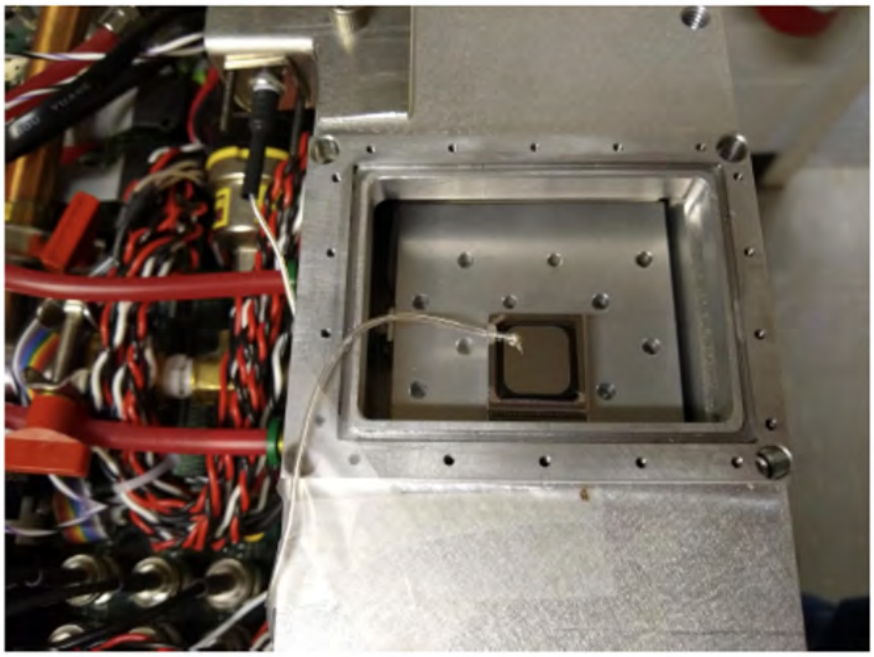

Figure 6.1: MMPAD 2×3 housing with 200 μm a-Se detector [14]

dramatically. For both sources, we computed the emission spectrum by measuring the energy of single photons passing through a small opening ($\sim$1mm^2) via a cadmium telluride drift detector. Drift detectors compute the total ionized charge that "drifts" to a single electrode and are particularly well-equipped for photon counting and high resolution measurements of photon energies [7].

Like our silicon and germanium analyses, we computed an edge spread function from the image of a tantalum knife edge. See Section 4.4.3 for a more detailed explanation regarding the procedure for computing the ESR from averaged knife edge images. Moreover, from the ESR, we determined the modulation transfer function (MTF), which describes the strength of the detector response to a pattern (such as line pairs) with a given spatial frequency [39]. The MTF is straightforward to calculate from the ESR - please see [39] for a more rigorous explanation.

The ESR is fit to a ramp function convoluted with a Gaussian kernel. The

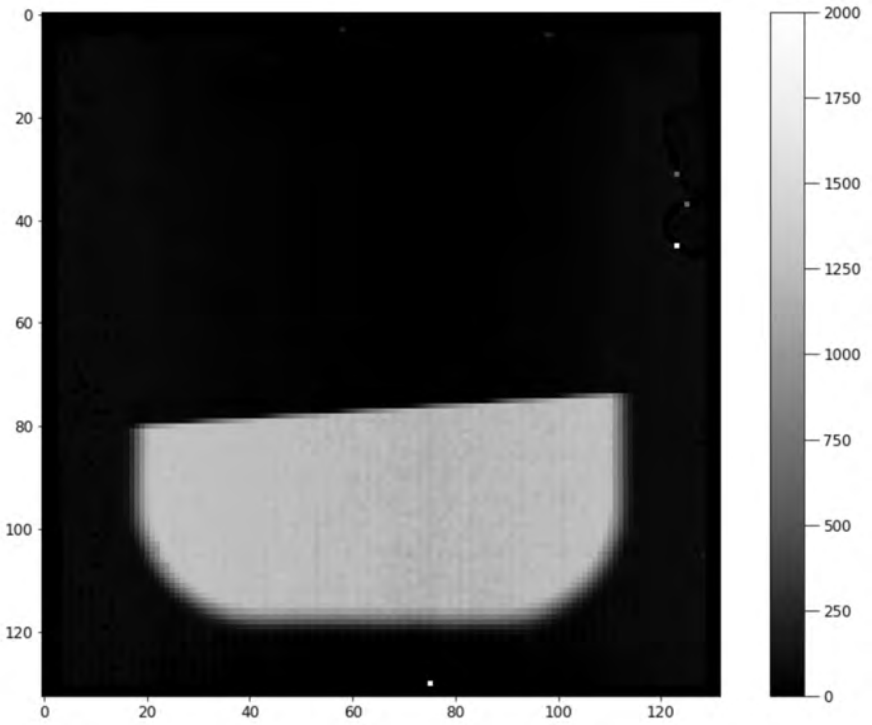

Figure 6.2: Knife edge image from flood illumination X-rays from the Ag tube biased at 47 kV with a 1 mm Al filter in place. The image is an average from frames with a 80 ms collection time.

spread of the charge cloud spread is represented by the width of the Gaussian. Figure 6.3 shows the energy spectra, ESR and MTF data from each source. For the Ag data, we noticed a pronounced non-linearity on the "ramp" portion of the ESR data, which led to low-quality fits. As a result, the ramp/Gaussian best fit was determined via a least squares regression on the subset of data points ($\pm$(0.3-0.7) pixels from the edge) most strongly affected by the Gaussian profile. Once the optimal Gaussian width was determined on this set, the resulting fitting function was imposed on the entire set of ESR data and the associated MTF was computed.

The average X-ray energies were 8.98 keV for the Cu source and 22.1 keV for the Ag source. The sub-pixel resolutions from the ESR fit were 5.12 μm and 10.1 μm respectively, both of which are very small relative to the pixel size. The MTFs also

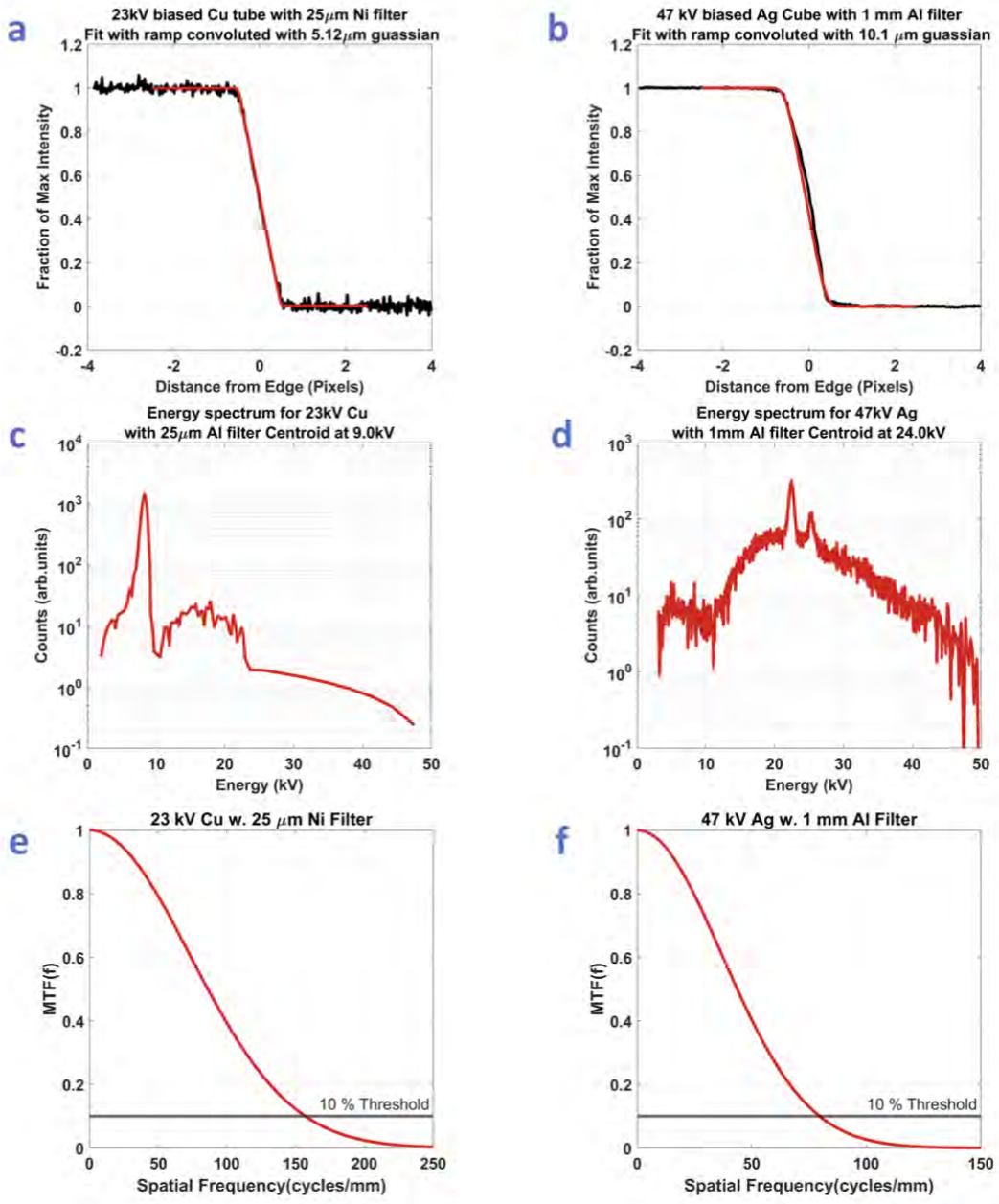

Figure 6.3: The first column presents data from X-rays emitted by the Cu tube biased at 23 kV with a 25 μm Ni filter in place. The second column presents data from X-rays emitted by the Ag tube biased at 47 kV with a 1 mm Al filter. Panels (a) and (b) illustrate the edge spread responses with their associated fits. Panels (c) and (d) show the illumination energies from both sources. Panels (e) and (f) presents the modulation transfer functions that can be computed from the fits in panels (a) and (b) [14].

show that the detector is capable of discerning patterns with a spatial frequency on the order of tenths of an inverse micron. However, there were several interesting features in the edge spread behavior that are not completely understood. For one, the "roll-off" observed in the ESRs for the silicon and germanium sensors from a strongly biased Ag source (see Section 4.4.3 and Section 5.2.3) is largely minimized (if not completely imperceptible) in the Ag ESR for selenium. We speculated that the previously observed roll-off could be attributed to excess fluorescence in the X-ray beam pipe. Though we used the same X-ray setup for the selenium analysis, the detector was placed in a different housing, so it is possible that the majority of the photons from the fluorescence did not reach the detector due to a change in alignment.

Another interesting feature is the non-linearity of the ESR for the high energy source. We verified that this was present for a similarly-biased Molybdenum tube and are confident that this is an attribute of the detector itself as opposed to the X-ray source. It is also surprising that this behavior is not observed for the lower energy spectra from the Cu source. Physically, the data suggests that for pixels only partially illuminated, a higher fractional intensity is registered than what would be expected given the fraction of the area covered by the knife edge. This effect is more pronounced when less of the pixel area is obscured, meaning the most strongly affected pixels neighbor ones that are fully illuminated.

One hypothesis is that the selenium itself is fluorescing by a measurable amount when exposed to higher energy X-rays. Selenium has a kα line of 12.6 keV, so this effect would be minimized for lower energy emissions [40]. In this scenario, a fraction of the photons with sufficient energy would, upon interacting with the bulk amorphous selenium, would create secondary X-rays that could travel laterally

throughout the semiconductor and excite electrons to the conduction band at a nearby location. As a result, illuminated pixels adjacent to the edge may fluoresce such that the "signal" associated with the fluorescent photons could be registered by pixels that are obscured by the knife edge. This would lead to an overestimation of the fractional intensity for these neighboring pixels. Though fluorescence may occur in silicon and other materials, we expect that it is more pronounced in selenium due to its lower attenuation length [41]. Altogether, the a-Se sensor performed very well and exhibited strong spatial resolution. Direct-deposition amorphous sensors are a promising technology for X-ray imaging at a synchrotron.

CHAPTER 7

TRANSIENT BEHAVIOR AND LEAKAGE CURRENT INSTABILITY IN LEAD PEROVSKITE

7.1 Properties of Lead Perovskite Semiconductors, Production, and Operating Conditions

The high-Z semiconductors presented in this thesis thus far (germanium and selenium) have generally performed well, but a high concentration charge traps and other defects have introduced complications regarding high leakage currents, low charge collection efficiencies, and other features that dramatically reduce imaging performance. These aberrations are mostly introduced during fabrication. Therefore, it is difficult to assess the long-term viability of the these materials for synchrotron X-ray imaging without substantial developments upstream. The high-Z collaboration is interested in characterizing atypical semiconductors for synchrotron imaging that have been studied in far less detail than germanium, CdTe, and other oft-mentioned alternatives to silicon. Many of these materials are selected because high quality crystals can be grown with extremely few defects. As a result, the question of sensor performance depends on the behavior of the semiconductor under a high bias, high radiation fluxes and other characteristics of a synchrotron environment as opposed to its inherent solid-state properties after fabrication.

Lead perovskite ($CsPbBr_3$) has emerged as one such promising candidate. A group at Northwestern and Argonne National Laboratory has fabricated a single-crystal lead perovskite semiconductor that exhibits the appropriate IV character-

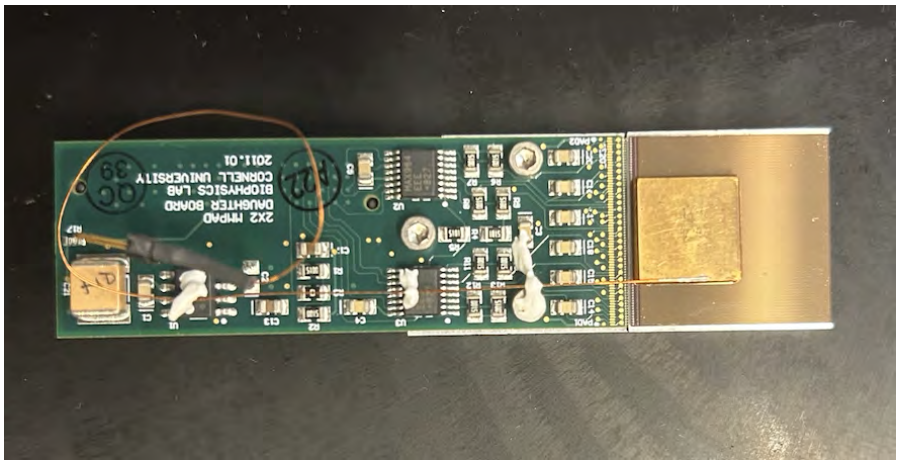

Figure 7.1: Lead perovskite MMPAD detector. The perovskite sensor only occupies a set of pixels near the bottom of readout pixel array.

istics for large range of biases, low dark currents (on the order of a nA), and photosensitivty to a broad dynamic range [15]. Lead perovskite belongs to a broader category of semiconducting materials known as solution-processed metal halide perovskites (MHPs) [42]. In a previous study, the same group demonstrated that MHPs have a remarkably high "defect tolerance", meaning the chemical structure of these crystals leads to strong charge transport characteristics [42]. The crystal purity was verified via a measurement of the time-resolved photoluminescence (TRPL) decay lifetime, which determines how quickly photogenerated charge recombines with defect-induced charge traps.

A millimeters-thick hole-collecting lead perovskite crystal was bump-bonded to a contiguous region of pixels on the MMPAD. The crystal was too small to cover the entire ASIC. The sensor was characterized at room temperature and under a vacuum. Preliminary images were taken under a 300 V bias.

7.2 Characterization of Dark Current and Preliminary Images

The behavior of the perovskite MMPAD exhibited a high degree of instability as the IV behavior and detection conditions changed dramatically with time. As a result, we were only able to collect a very limited set of measurements before the sensor completely broke down, so much of our analysis is limited to qualitative observations.

We first biased the detector at 300 V which brought about a total bias/leakage current of approximately 1.2 μA. The pixel intensities were completely saturated, so imaging was initially impossible. However, the total leakage current appeared to decrease rapidly over time and had halved after an hour of biasing. The decrease in leakage current led to smaller pixel intensities, and although the detector response was visibly different with and without incident X-rays, the high pixel noise completely obscured any meaningful X-ray image. The total current passing through the sensor also increased by several hundredths of a microamp with X-rays on. Background-subtracted dark images were characterized by localized regions with dramatic fluctuations in intensity. The time scale of these fluctuations was on the order of seconds and had an amplitude far greater than the readout noise. We left the sensor under a 300 V bias overnight, hoping that the leakage current and total noise would continue to decrease.

By the next day, the leakage current had dropped to $\sim$0.15 μA. The visible intensity fluctuations had also dropped significantly, and X-ray images with a degree of uniformity and resolution could be taken. Figure 7.2 shows the leakage current before and after approximately 16 hours at high bias. The decrease in

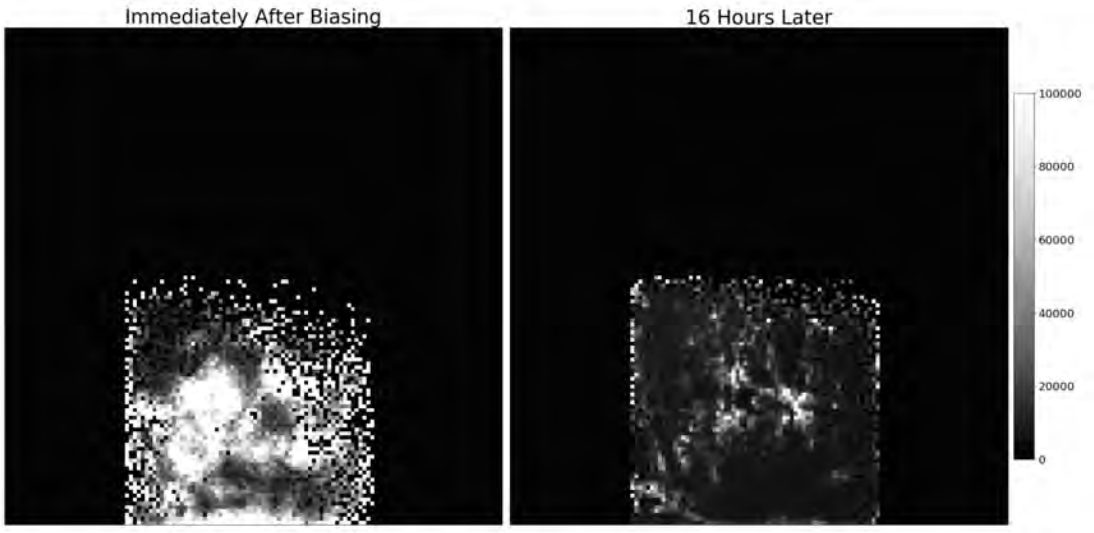

Figure 7.2: Background ADU images immediately after applying a 300 V bias and after approximately 16 hours of biasing. Each image consists of an average of 1000 frames with a 10 ms collection time each.

pixel current is apparent, and it is clear that several bright spots have persevered but may be in different locations than they were initially. It is difficult to precisely define the causes of this behavior, but if the perovskite is assumed to have an extremely low defect concentration, it is likely that the sensor is not bonded to the ASIC is a uniform way, or there exists some material breakdown at the interface of the crystal with the MMPAD. During sensor fabrication, there were concerns that $CsPbBr_3$ was too soft for a standard indium bump-bonding procedure, so new techniques were implemented using silver epoxy bumps. It is also possible that the crystal was damaged at some point due to the environmental conditions (perovskite is sensitive to moisture) and that these effects led to the unanticipated breakdown of the sensor itself.

Figure 7.3 shows an X-ray image of a line pair mask, taken with the Mo tube biased at 47 kV. The image is of a reasonable quality - there is an evident lack of signal uniformity across the face of the sensor with notable localized bright patches at various locations, but the main features of the mask are visible, suggesting that

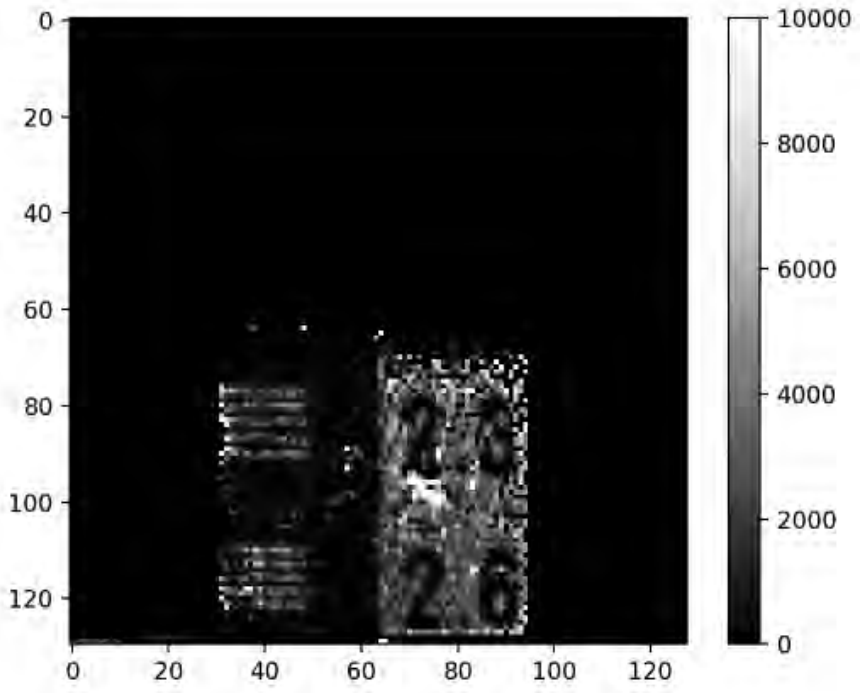

Figure 7.3: Image of a line pair mask taken with a 47 kV biased Mo tube. The image is a background-subtracted average of 1000 frames, each with a 10 ms collection time.

the resolution is at least of the order of the line width.

7.3 Bias Current Instability and IV behavior

After collecting the initial leakage current data and imaging the line pair mask, we left the perovskite under a 300 V bias over the weekend, hoping that the leakage current would continue to decrease. However, when we returned, the current was at the compliance value of 105 μA. This suggested that a prolonged exposure to high bias had led to a reverse breakdown in the photodiode array, though this had not been observed in our earlier measurements or in previous studies [15]. The current remained at compliance while the bias was decreased until 10-20 V would

be reached.

However, another interesting effect that we observed was that for biases less than 100 V, the bias current would occasionally jump back down to a reasonable value ($\sim$0.1 μA) and remain there for a short period of time before instantaneously returning back to compliance. Downward jumps would be facilitated by decreasing the bias voltage, while upward jumps were facilitated increasing the bias voltage. However, these behaviors were also observed with no perturbation at all.

Over the next several weeks, we monitored the leakage current of the perovskite sensor for a 100 V bias. The magnitude of the measured current was usually several microamps and decreased very slowly. However, the supplied current would occasionally jump to compliance (105 μA) for a short period of time, before returning to its typical value of several microamps. The current was never low enough for imaging to be possible at 100 V and would jump to compliance if a 200 or 300 V bias was attempted.

We measured the IV behavior of the sensor in its "low current" state. Starting from -10 V (forward biased), I collected data in +5 V increments until I reached a 50 V bias. Since the bias current changed with time, usually trending upward if I had been increasing the voltage, for each bias I took 6 measurements separated by 10 second increments. The value plotted in Figure 7.4b corresponds to the last reading measured after a full minute of biasing. After reaching 50 V, I increased the voltage in +10 V steps. The sudden jump at 110 V and 120 V is consistent with described instability, in which after the initial jump, the current would either soon increase to the compliance value of 105 μA or return to the appropriate value ($\sim$10 uA). Here, it decreased back roughly the expected value, so data taking could continue uninterrupted. The current jumped to compliance at a 210 V bias and

would not return to the low current state, so data is not available for higher biases.

In this biasing range, the total current does not plateau at some bias, as would be expected if the sensor exhibits diode characteristics. Figure 7.4 compares the IV behavior measured by the Argonne/Northwestern group who fabricated the sensor with our measurements with the sensor bonded to the MMPAD. These results, coupled with the strong instability in overall sensor behavior, suggests that the sensor was in damaged in some way. Again, this is likely due to the environmental conditions the sensor had been exposed to or to a breakdown at the interface of the crystal and the ASIC. A characterization of imaging performance is not possible until we better understand the sensor behavior under an applied bias.

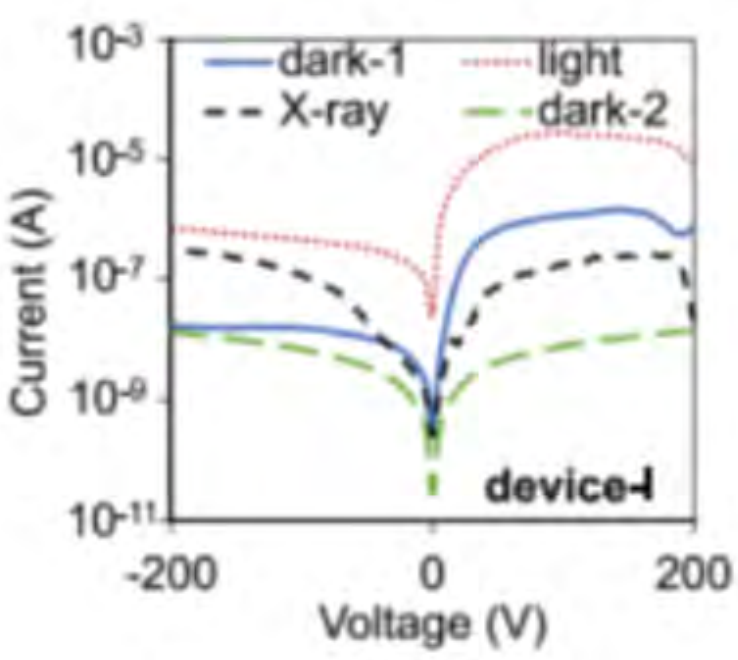

(a)

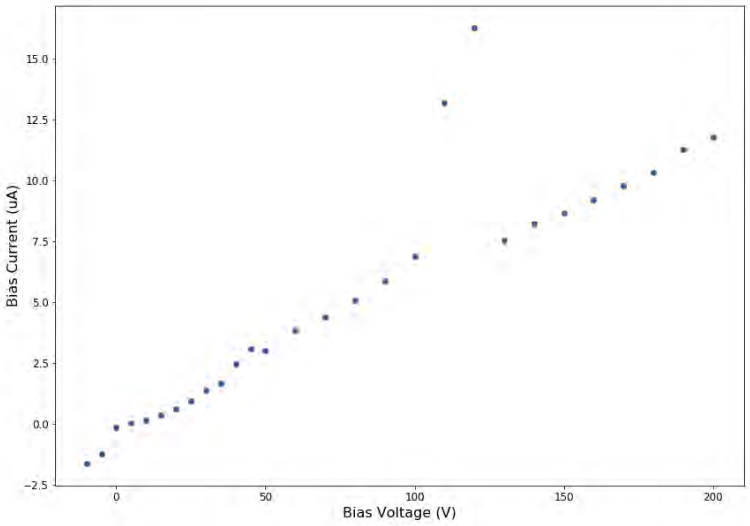

(b)

Figure 7.4: (a) is the IV behavior measured by the group at Northwestern/Argonne [15]. The curve labelled "light" most closely corresponds to the conditions in which we collected data. For their plot, negative voltages represent a reverse bias. (b) is the IV behavior measured by the Cornell group after the sensor was bump-bonded to the MMPAD. Positive voltages correspond to a reverse bias. After bonding, the sensor exhibits a far greater leakage current that increased linearly with reverse bias. This diverges from the expected behavior of a diode detector.

CHAPTER 8

CHARACTERIZATION OF SENSOR BEHAVIOR AND CHARGE TRAPPING IN CADMIUM ZINC TELLURIDE - SELENIUM (CZTS)

8.1 Properties of CZTS Semiconductors, Production, and Operating Conditions

Single-crystal cadmium telluride (CdTe) sensors are a viable high-Z sensor material with a high quantum efficiency and a low dark current at room temperature. However, the growth of CdTe crystals often introduces a high concentration of defects that lead to charge trapping in the bulk semiconductor [43]. This results in dose-dependent polarization, an effect that reduces the sensor's response to incident radiation after a prolonged exposure to X-rays [44].

Previous studies have shown that CdTe can be doped with zinc (CZT) to increase sensor hardness, reduce defects in the crystal bulk, widen the band gap, and increase the total sensor resistivity [43, 45]. The material can also depolarize without the application of a forward bias to detrap charge, a necessary step for CdTe. CZT sensors have been characterized at light sources, but still exhibit inefficient charge transport properties, particularly for holes [46]. However, when also doped with selenium to make CZTS, the crystal growth yield (percent of crystal volume that is detector grade) has been measured to be nearly 90%, far greater than the best reported yield of CZT, 33% [46]. Moreover, the inclusion of selenium reduces the total concentration of tellurium precipitates, the location of the majority of charge traps [46]. As the high-Z community looks to fabricate

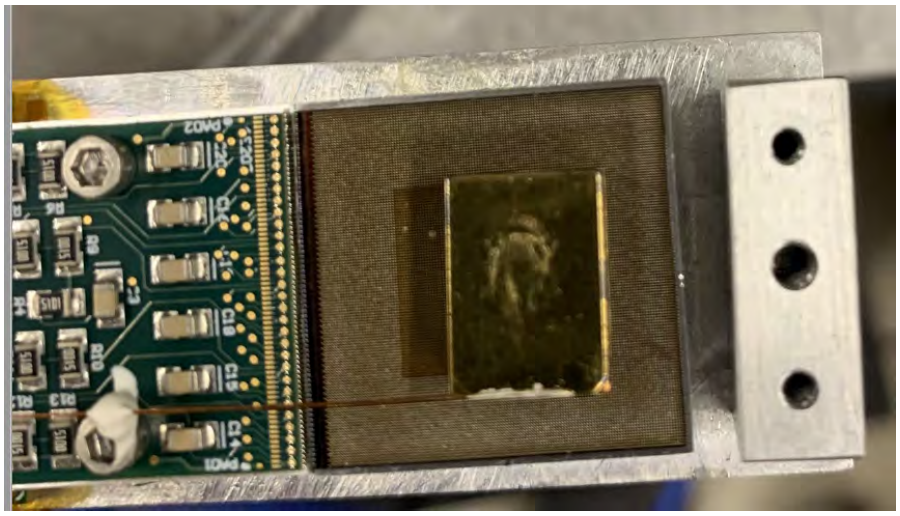

Figure 8.1: CZTS MMPAD detector

sensor materials for which single crystals of the highest quality can be grown, CZTS appears to be an extremely compelling option for which characterizations with hard X-rays are a high priority [45].

A several centimeters thick, hole-collecting CZTS crystal was grown and bump-bonded to an MMPAD ASIC at Brookhaven National Laboratory. Like the perovskite, the sensor only covered a fraction of the readout pixels and was characterized under vacuum and at 20^{o}C. The detector was also taken to Cornell's X-ray synchrotron, CHESS, for measurements in a higher-energy, higher-flux environment. Only the results from the in-lab characterization are included in this thesis, as the data collected at CHESS has not been analyzed in its entirety at the time of writing.

8.2 ASIC Noise and Sensor Dark Current

Since the depletion and leakage current behavior of this particular sensor was not known before characterization, much of our analysis was focused on deter-

mining the ideal voltage with which to bias the sensor. Like silicon, we first characterized the readout noise and dark current, but did so at a variety of biases.

Figure 8.2 presents the root-mean-square (RMS) images of a set of backgrounds taken at various bias voltages. Note that this approach for computing the background is different from what was described for silicon in Section 4.2. With silicon, we assumed high uniformity in the response of individual pixels and computed a single value to quantify the readout noise. This value was ascertained from a histogram of the intensity of each pixel for each frame. For CZTS, we do not assume that each pixel will have comparable noise. Therefore, to determine the frame-by-frame noise on a pixel-by-pixel basis, we computed the RMS of a given pixel's intensities from the set of collected background images. The lower pixels in the image are clearly less noisy than the rest of the sensor, particularly for the lower/intermediate biases tested. The visible change in noise, seemingly at a particular pixel row, suggests either a conscious change in the bump-bonding, doping, or other physical property of the crystal itself or an unintended modification of the electronic properties of this portion of the readout array.

Figure 8.3 is a dark current map of the sensor for a 50 V and a 100 V bias. The dark current appears relatively uniform across the face of the sensor (rarely larger than 2 pA per pixel) and the total dark current across the face of the sensor increases from 315 pA to 618 pA from a 50 to 100 V bias. For a 100 V bias, localized bands across the face of the sensor register largest dark currents and a handful of brighter, "flaky" pixels begin to appear. Assuming a sufficient detector sensitivity and gain like that of silicon ($\sim$44 ADU per photon), the readout noise and dark current are reasonably low and should not impede X-ray imaging; however, subsequent measurements indicated otherwise.

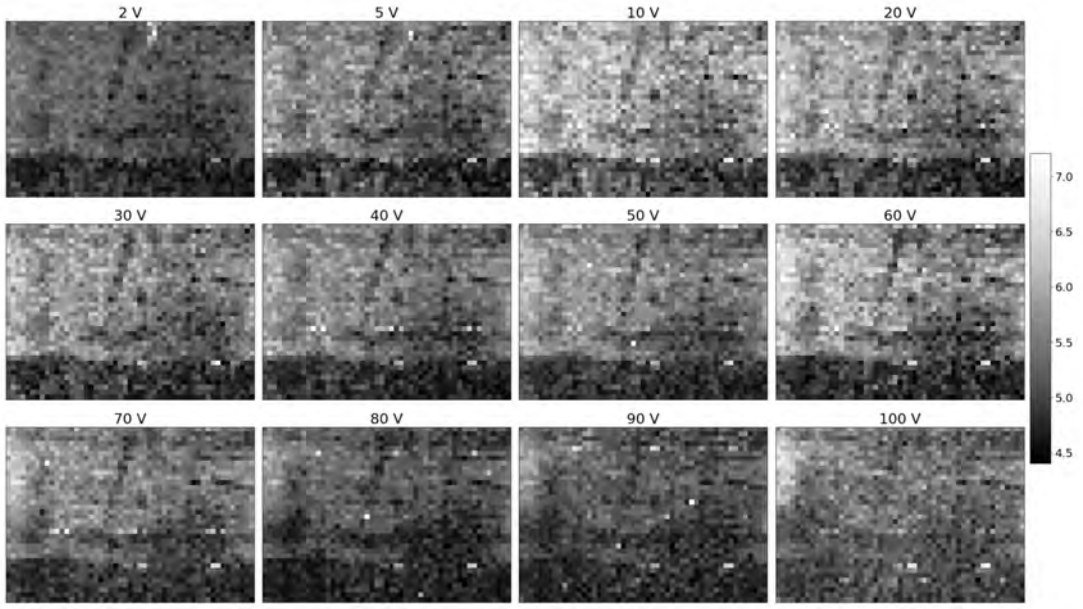

Figure 8.2: RMS ADU images of the CZTS sensor from a set of backgrounds. Each RMS image was computed from 1000 frames, each with a 10 ms collection time.

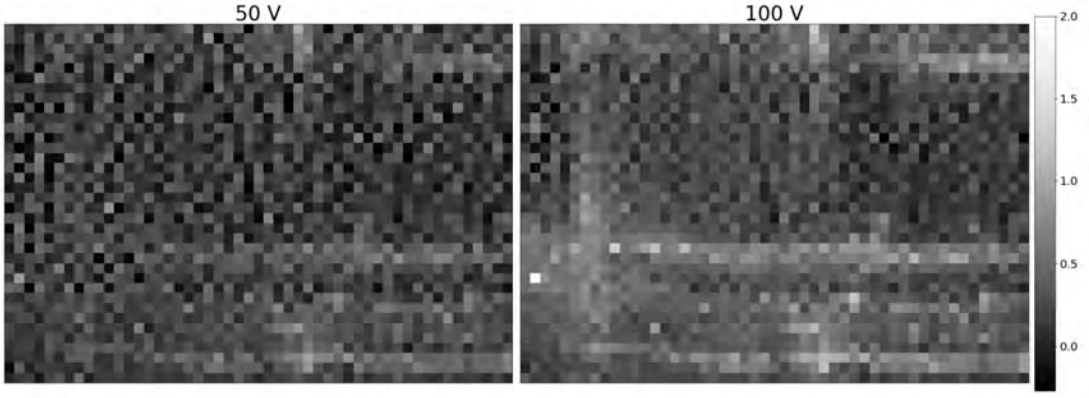

Figure 8.3: Map of sensor dark current (in pA) for a 50 and 100 V biases.

8.3 Flood Illumination Response with Varying Voltage Bias

Next, we investigated the response of CZTS to flood illumination. In particular, we were interested in how the charge collection efficiency varies with applied bias voltage. We quantified this by measuring the change in average pixel intensity. A

higher bias usually correlates with a better charge collection efficiency, as the charge carriers experience a stronger attraction to the readout electrodes. However, after a sufficiently high bias, the improvement in charge collection efficiency begins to plateau, as nearly all photogenerated charge reaches the ASIC. The bias at which this plateau begins is usually best for imaging, as the charge collection efficiency is essentially optimized and the polarization effects associated with higher biases may be avoided.

We characterized the response of the sensor to flood illumination from the Ag tube biased at 47 kV. We maximized the incoming photon flux by using no filters. Figure 8.4 shows the resulting ADU images for several biases. The overall imaging performance is very poor. The small measured intensities suggest that either only a small fraction of the incident photons are absorbed by the material or that very few of the generated charge carriers in the sensor actually reach the readout chip (i.e. the charge collection efficiency is extremely low). Moreover, the high frame-by-frame pixel noise, illustrated in Figure 8.2, clearly affects the image quality. The bottom, less-noisy half of the sensor appears more uniform and photosensitive. For the higher biases in Figure 8.4, a small patch with a strong intensity (circled in red) begins to form, potentially indicating that sensitivity may improve for larger biases.

One possible explanation for the low sensitivity is the presence of a "dead" layer at the top (furthest away from the ASIC) portion of the sensor. A dead layer is a region with large transverse electric fields, often produced by charge traps. The presence of a dead region near the top of the sensor is usually an unavoidable feature of fabrication, but for most sensors, this layer is thin and the X-rays are sufficiently energetic such that the majority of X-rays are absorbed at a location

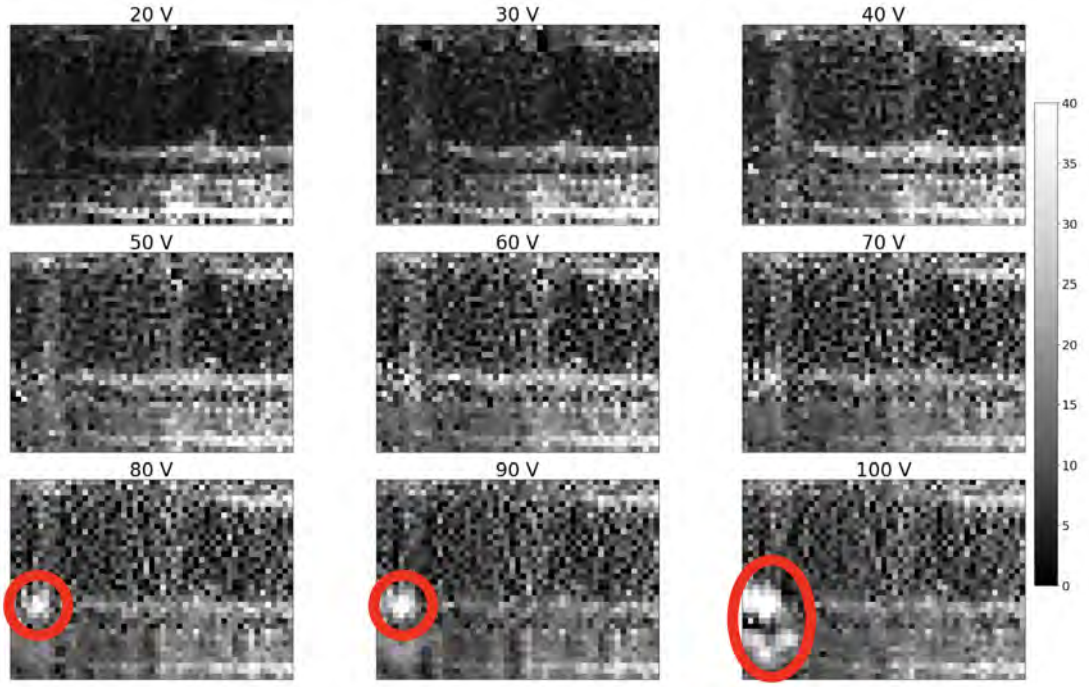

Figure 8.4: Sensor response, in ADU, from flood illumination from a 47 kV biased Ag tube. Each image is an average of 1000 frames, each with a 10 ms collection time. The red circled regions are spots of high intensity and strong response.

past the dead region. For the CZTS sample, we hypothesize that most photons are absorbed in the dead layer and the majority of the generated charge in this region travels laterally in the dead region or is absorbed by charge traps. The geometry of the dead layer likely varies across the face of the sensor, leading to the lack of uniformity in the flood illumination response. From Figure 8.4, it appears that for a given frame, the amount of charge that eventually reaches the ASIC corresponds to a signal of $\sim$20 ADU, which is a fraction of an X-ray. On the rare occasion a photon is absorbed past the dead layer, the part of the sensor I denote the active region, the photogenerated charge reaches the ASIC and is processed normally.

As a result, much information is lost when only averaged images are considered. For a given pixel, the "true" response, corresponding to when a photon is absorbed in the active region, is only observable for certain frames. We are specifically

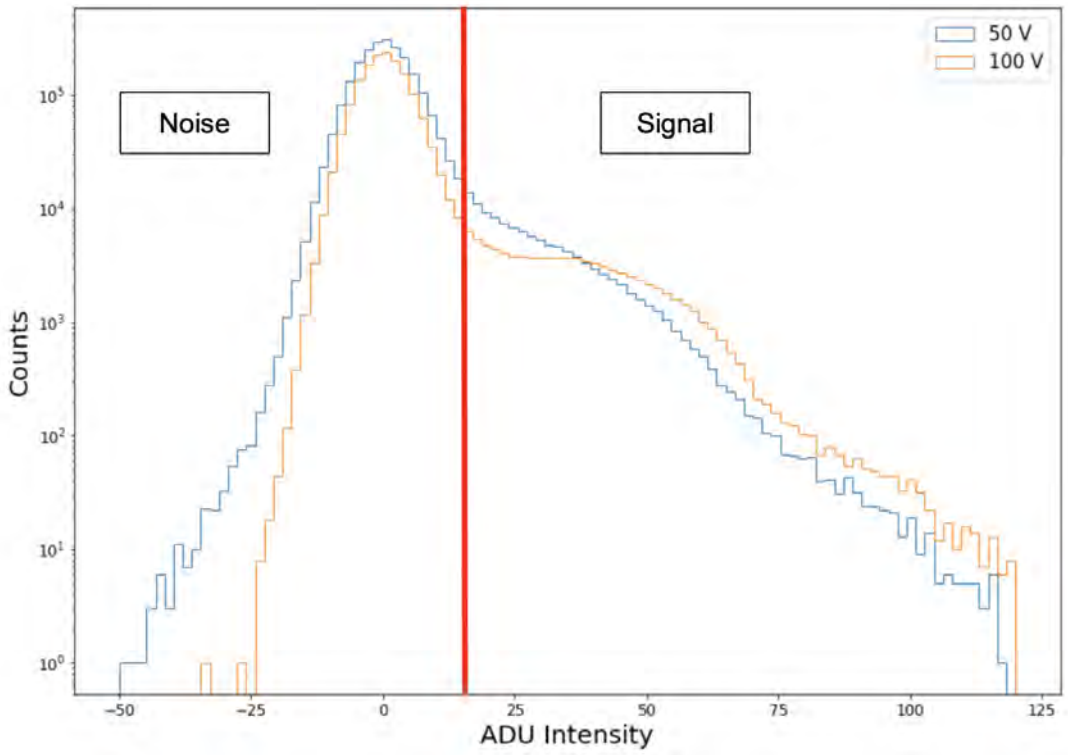

Figure 8.5: Histogram of all registered ADU values with the mode intensity of a given pixel subtracted. The data associated with the specified bias voltage is compiled from 1000 frames with a 10 ms collection time. The sensor noise from the dead layer "blur" is represented by the component of the distributions left of the red line. The signal from photons absorbed in the active region is represented by the part of the distribution right of the red line.

interested in the signal intensities associated with these events. For a given bias and for each pixel individually, we determine the *mode* intensity from the set of frames. Then, for the same set of frames, we subtracted the mode intensity associated with that pixel from each registered value. The resulting data is histogrammed in Figure 8.5 for a 50 V and a 100 V bias. The distribution of mode pixel intensities for the two biases were similar.

We introduce the idea of "mode background subtraction" to eliminate the blur associated with the small fraction of generated charge that leaks out of the dead layer. As expected, this fraction of charge strongly varies from frame-to-frame,

leading to a relatively wide distribution centered at 0 that can attributed almost entirely to noise. The sensor response to photons absorbed in the active region is given by the right half of the histogram, where the symmetry of the distribution about 0 is broken. Clearly, tabulated intensities associated with noise/blur (i.e. a lack of absorbed photons in the active region) are more frequent than true photon measurements by up to several orders of magnitude. As expected, the majority of signal photons have an intensity of $\sim$40 ADU, corresponding with the expected value for silicon. Moreover, significantly more signal events are registered with a 100 V bias than a 50 V bias, which suggests better charge collection efficiency for higher biases in the active region. The 100 V biased sensor also exhibits a smaller spread in the noise portion of the distribution, potentially indicating more uniformity in the behavior of the dead layer across the face of the sensor.

8.4 Dynamic Response

In the previous section, we speculated that the total response of the CZTS sensor to flood illumination was inhibited by a wide dead layer defined by a high concentration of charge traps. The filling of deep charge traps in CdTe and the resulting alterations of the electric field in the sensor bulk have been shown the reduce the charge collection efficiency [47]. Again, this feature is known as polarization and is one of the main limitations of the CdTe detectors [44, 43]. Polarization increases for longer exposures, as the deep traps grow increasingly full with prolonged exposures to radiation. Thus, the sensor response is time-dependent.

We mentioned before that selenium is added to CZT to reduce the concentration of charge traps and to lessen polarization effects [46]. However, the presented

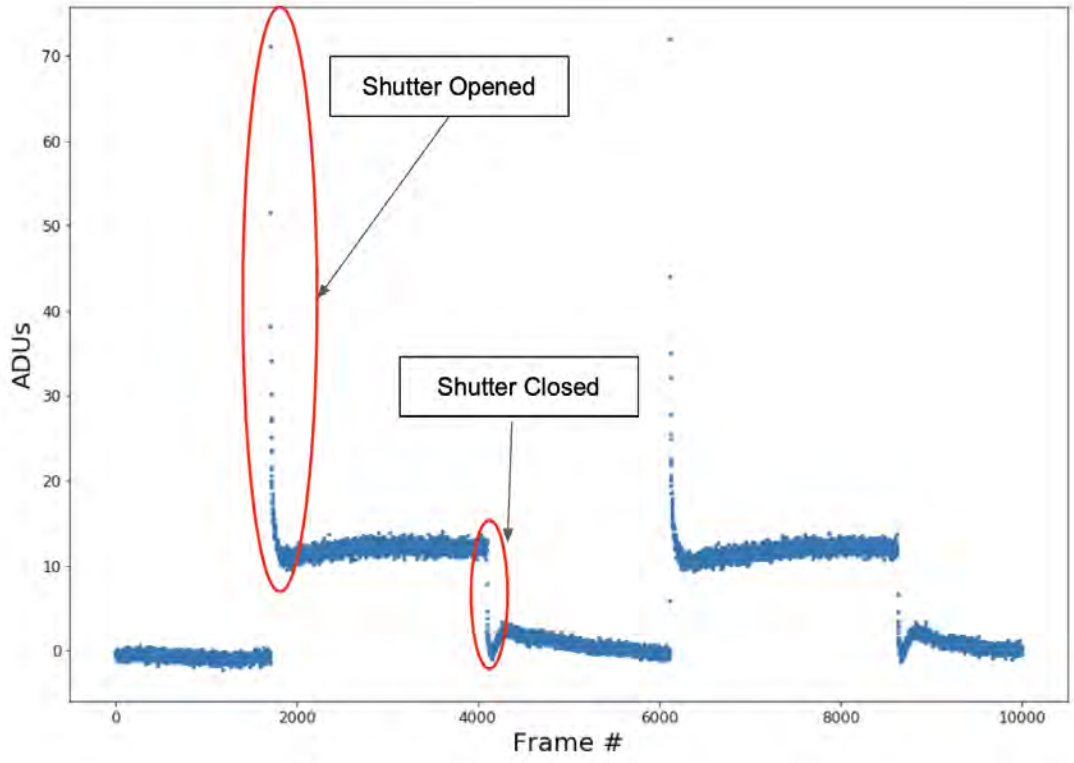

Figure 8.6: Dynamic response of CZTS from the 47 kV biased Ag tube with no filter. The collection time was 10 ms. The average, background-subtracted pixel intensity for each frame is plotted. A sudden increase in average pixel intensity corresponds with the opening of the shutter, while a sudden decrease corresponds with its closing.

discussion on the sensor dead layer suggests that the behavior of our CZTS sample is very much affected by the presence of charge traps and that it would be worthwhile to specifically investigate the change in sensor response with time. In particular, we characterized the dynamic response of the sensor, or how the measured intensity changes when the shutter is turned on and off. We used X-rays from the Ag tube biased at 47 kV, biased the sensor at 50 V, and plotted the average pixel intensity for each frame from our set of background-subtracted images. The shutter was opened and closed twice throughout data collection.

The shutter was not open long enough to draw any conclusions regarding long-

term sensor polarization akin to what is observed in CdTe. However, the initial spikes and drops in intensity when the shutter is opened and closed possibly indicate a similar phenomena. The average pixel intensity ($\sim$70 ADU) when the shutter is first opened corresponds to the expected sensor response with little to no distortion of the electric field in the sensor bulk. The sharp decrease in registered intensities could be attributed to the rapid filling of charge traps. Once the charge traps are filled, the electric field in the semiconductor no longer points uniformly towards the readout chip, reducing the charge collection efficiency dramatically and leading to the steady-state blur observed in the averaged flood images. The data also suggests that after the initial trap filling (assuming that this is indeed the cause of this behavior), the registered intensities slowly increase before the steady state is reached. At this steady state, we assume that trapping and detrapping occur at roughly the same rate.

The dramatic decrease to 0 ADU immediately after the shutter is closed is expected, as there is no new current generated by photons that can be integrated by the ASIC. However, the subsequent small increase immediately after this drop in intensity is surprising. This could be due to the detrapping of the charge that had been generated earlier from X-rays. Moreover, with a lack of newly-photogenerated charge to refill the traps, the rate of detrapping is expected to decrease with time. This potentially explains the loss in intensity after the initial spike.

Further analysis is required to verify that these effects can be prescribed to a wide dead layer with an especially high concentration of charge traps. We hope that an analysis of the sensor response to higher energy X-rays would somewhat reduce the blurring effect, as a larger portion of the incident photons would be absorbed in the active region. Moreover, we expect charge traps to fill more quickly with

harder X-rays at a higher flux, resulting in a faster decrease in sensor response upon opening the shutter. A preliminary analysis of the CHESS results suggests that any improvement is only marginal, as the ratio of signal to blurring-induced noise is still smaller than expected.

CHAPTER 9

CONCLUSIONS AND FUTURE WORK

9.1 Summary

X-ray radiation is an essential tool for a variety of scientific applications, including medical radiography, high energy diffraction experiments, and other techniques through which materials can be characterized at the atomic scale. Many such experiments occur at a synchrotron light source, where high energy X-rays can be produced with the highest fluxes. However, the quality of data collected at a synchrotron is often limited by poor detector performance, particularly for X-rays with energies greater than 20 keV. One compelling detector technology is the Hybrid Pixel Detector, which consists of a semiconducting sensor layer bump-bonded to a readout chip. We characterized various high-Z sensors bonded to Cornell's MMPAD readout architecture. High-Z materials exhibit better photon absorption at high energies than silicon, and the MMPAD is particularly well-equipped for continuous readout in a high-flux environment.

We characterized four different high-Z sensor materials: germanium, amorphous selenium, lead perovskite, and CZTS. The high-Z community is interested in germanium and amorphous selenium because their behavior as semiconductors is well-understood and fabrication methods are mature. Both detectors were fundamentally photosensitive and able to produce coherent images. However, the depletion behavior in germanium was somewhat unpredictable, likely due to a low wafer resistivity. The spatial resolution of a-Se worsened at higher energies and the charge collection efficiency was not ideal.

Lead perovskite and CZTS represent a new emphasis on the growth of high-quality single crystals for photon detection, even if the necessary constituents are less readily available. The perovskite exhibited extremely unstable depletion and leakage current behavior, which made imaging not feasible. The IV behavior of CZTS was stable, but the sensor lacked sufficient sensitivity to incident X-rays, likely due to a high concentration of charge traps in a thick dead layer at the top of the sensor.

9.2 Next Steps

The results presented in this thesis demonstrate that while an ideal sensor for high energy X-ray imaging at a synchrotron still has not been found, many sensor materials exhibit novel and exciting behaviors that could be the subject of future investigations. A photosensitive, millimeters-thick germanium wafer has been fabricated at Brookhaven National Laboratory and would circumvent many of the limitations on thick germanium outlined in this thesis. The direct deposition of high-Z materials, like a-Se, was shown to be compatible with the MMPAD, introducing a new category of semiconductors for characterization. The group also collected data with the CZTS sensor at CHESS, which will enable a more precise characterization of the charge collection efficiency at high energies. Much work is required to create a novel X-ray detector, but acquiring an understanding of candidate sensor materials is an important and exciting first step.

BIBLIOGRAPHY

[1] J. T. Weiss, K. S. Shanks, H. T. Philipp, J. Becker, D. Chamberlain, P. Purohit, M. W. Tate, and S. M. Gruner, "High dynamic range x-ray detector pixel architectures utilizing charge removal," *IEEE Transactions on Nuclear Science*, vol. 64, no. 4, pp. 1101–1107, 2017.

[2] D. R. Schuette, *A mixed analog and digital pixel array detector for synchrotron x-ray imaging*. PhD thesis, Cornell University, 2008.

[3] A. Maier, S. Steidl, V. Christlein, and J. Hornegger, *Medical imaging systems: An introductory guide*. Springer, 2018.

[4] W. A. Tayon, K. E. Nygren, R. E. Crooks, and D. C. Pagan, "In-situ study of planar slip in a commercial aluminum-lithium alloy using high energy x-ray diffraction microscopy," *Acta Materialia*, vol. 173, pp. 231–241, 2019.

[5] Cornell University, "Cornell high energy synchrotron source (chess)," Oct 2018.

[6] D. Pennicard, B. Pirard, O. Tolbanov, and K. Iniewski, "Semiconductor materials for x-ray detectors," *MRS Bulletin*, vol. 42, no. 6, pp. 445–450, 2017.

[7] G. Lutz *et al.*, *Semiconductor radiation detectors*. Springer, 2007.

[8] MKS Instruments, "Diode physics."

[9] Aspencore, "Pn junction diode and diode characteristics," Aug 2022.

[10] Last Minute Engineers, "Pn junction diode."

[11] J. Becker, *Signal development in silicon sensors used for radiation detection*. PhD thesis, Hamburg University, 2010.

[12] E. Haug and W. Nakel, *The elementary process of bremsstrahlung*, vol. 73. World Scientific, 2004.

[13] C. Suryanarayana, M. G. Norton, C. Suryanarayana, and M. G. Norton, *X-rays and Diffraction*. Springer, 1998.

[14] Z. Han, A. Mukherjee, A. Albert, A. Rumaiz, I. Harding, M. Tate, S. Gruner, J. Thom-Levy, A. Kuczewski, D. Siddons, *et al.*, "High spatial resolution direct conversion amorphous selenium x-ray detectors with monolithically integrated cmos readout," *Journal of Instrumentation*, vol. 18, no. 04, p. P04021, 2023.

[15] L. Pan, I. Pandey, A. Miceli, V. Klepov, D. Y. Chung, and M. Kanatzidis, "Perovskite cspbbr3 single-crystal detector operating at 1010 photons/s/mm2 for ultra-high flux x-ray detection," 2022.

[16] R. Holmes, "Gamma ray and neutron sources," 1982.

[17] T. Zhang, C. Wilson, and M. Schamschula, "X-ray flares from sagittarius a* and black hole universe," *Progress in Physics*, vol. 12, no. 1, pp. 61–67, 2016.

[18] A. J. Calzavara and C. D. Matzner, "Supernova properties from shock breakout x-rays," *Monthly Notices of the Royal Astronomical Society*, vol. 351, no. 2, pp. 694–706, 2004.

[19] M. A. Meyers and K. K. Chawla, *Mechanical behavior of materials*. Cambridge university press, 2008.

[20] P. Willmott, *An introduction to synchrotron radiation: techniques and applications*. John Wiley & Sons, 2019.

[21] W. S. Boyle and G. E. Smith, "Charge coupled semiconductor devices," *Bell System Technical Journal*, vol. 49, no. 4, pp. 587–593, 1970.

[22] P. Magnan, "Detection of visible photons in ccd and cmos: A comparative view," *Nuclear Instruments and Methods in Physics Research Section A: Accelerators, Spectrometers, Detectors and Associated Equipment*, vol. 504, no. 1, pp. 199–212, 2003. Proceedings of the 3rd International Conference on New Developments in Photodetection.

[23] S. M. Gruner, J. R. Milch, and G. T. Reynolds, "Survey of two-dimensional electro-optical x-ray detectors," *Nuclear Instruments and Methods in Physics Research*, vol. 195, no. 1-2, pp. 287–297, 1982.

[24] P. Rossi, "L. and fischer, t. rohe, and n. wermes," *Pixel Detectors: From Fundamentals to Applications*, 2006.

[25] Nuclear Regulatory Committee, "Semiconductor detectors," Jan 2010.

[26] N. Sato, *Electrochemistry at metal and semiconductor electrodes*. Elsevier, 1998.

[27] W. Shockley, *Electrons and holes in semiconductors: with applications to transistor electronics*. van Nostrand, 1959.

[28] H. Spieler, *Semiconductor detector systems*, vol. 12. Oxford university press, 2005.

[29] W. Shockley and W. Read Jr, "Statistics of the recombinations of holes and electrons," *Physical review*, vol. 87, no. 5, p. 835, 1952.

[30] T. P. Pearsall, *Photonics essentials*. McGraw-Hill Education, 2003.

[31] S. Kasap, J. B. Frey, G. Belev, O. Tousignant, H. Mani, J. Greenspan, L. Laperriere, O. Bubon, A. Reznik, G. DeCrescenzo, *et al.*, "Amorphous and polycrystalline photoconductors for direct conversion flat panel x-ray image sensors," *Sensors*, vol. 11, pp. 5112–5157, 2011.

[32] G. Giacomini, W. Chen, A. Kuczewski, A. K. Rumaiz, and D. P. Siddons, "Operational conditions of silicon pixel arrays for x-ray spectroscopy," *IEEE Transactions on Nuclear Science*, vol. 66, no. 10, pp. 2245–2251, 2019.

[33] N. Khiyani and V. Singh, "X-ray image production equipment operation," in *StatPearls [Internet]*, StatPearls Publishing, 2021.

[34] H. A. Kramers, "Xciii. on the theory of x-ray absorption and of the continuous x-ray spectrum," *The London, Edinburgh, and Dublin Philosophical Magazine and Journal of Science*, vol. 46, no. 275, pp. 836–871, 1923.

[35] M. Krammer, "Silicon detectors in high energy physics experiments," *Scholarpedia*, vol. 10, no. 10, p. 32486, 2015.

[36] D. Pennicard, B. Struth, H. Hirsemann, M. Sarajlic, S. Smoljanin, M. Zuvic, M. Lampert, T. Fritzsch, M. Rothermund, and H. Graafsma, "A germanium hybrid pixel detector with 55μm pixel size and 65,000 channels," *Journal of Instrumentation*, vol. 9, no. 12, p. P12003, 2014.

[37] Y. Tian, C. Liu, D. Hutt, and B. Stevens, "Electrodeposition of indium for bump bonding," in *2008 58th Electronic Components and Technology Conference*, pp. 2096–2100, 2008.

[38] H. Huang and S. Abbaszadeh, "Recent developments of amorphous selenium-based x-ray detectors: a review," *IEEE Sensors Journal*, vol. 20, no. 4, pp. 1694–1704, 2019.

[39] K. Kohm, "Modulation transfer function measurement method and results for the orbview-3 high resolution imaging satellite," in *Proceedings of ISPRS*, vol. 35, pp. 12–23, 2004.

[40] G. Belev and S. O. Kasap, "Amorphous selenium as an x-ray photoconductor," *Journal of non-crystalline solids*, vol. 345, pp. 484–488, 2004.

[41] Lawrence Berkeley National Laboratory, "X-ray attenuation length."

[42] Y. He, I. Hadar, and M. G. Kanatzidis, "Detecting ionizing radiation using halide perovskite semiconductors processed through solution and alternative methods," *Nature Photonics*, vol. 16, no. 1, pp. 14–26, 2022.

[43] J. Franc, P. Moravec, V. Dědič, U. Roy, H. Elhadidy, P. Minárik, and V. Šíma, "Microhardness study of cd1-x znxte1-ysey crystals for x-ray and gamma ray detectors," *Materials Today Communications*, vol. 24, p. 101014, 2020.

[44] H. T. Philipp, M. W. Tate, K. S. Shanks, P. Purohit, and S. M. Gruner, "High dynamic range cdte mixed-mode pixel array detector (mm-pad) for kilohertz imaging of hard x-rays," *Journal of Instrumentation*, vol. 15, no. 06, p. P06025, 2020.

[45] O. Baussens, C. Ponchut, M. Ruat, M. Bettelli, S. Zanettini, and A. Zappettini, "Characterization of high-flux cdznte with optimized electrodes for 4th generation synchrotrons," *Journal of Instrumentation*, vol. 17, no. 11, p. C11008, 2022.

[46] J. W. Kleppinger, S. K. Chaudhuri, U. N. Roy, R. B. James, and K. C. Mandal, "Growth of cd0.9zn0.1te1–ysey single crystals for room-temperature gamma ray detection," *IEEE Transactions on Nuclear Science*, vol. 68, no. 9, pp. 2429–2434, 2021.

[47] Y. Petukhov and W. Krop, "The research of polarization in cdte pin detectors of nuclear radiation," in *2008 IEEE Nuclear Science Symposium Conference Record*, pp. 263–268, IEEE, 2008.